STRUCTURE PROPERTY AND DEFORMATION ANALYSIS OF POLYPROPYLENE MONTMORILLONITE NANOCOMPOSITES

Alejandro Hernandez-Luna, B.S., M.S.

Dissertation Prepared for the Degree of

DOCTOR OF PHILOSOPHY

UNIVERSITY OF NORTH TEXAS

May 2003

APPROVED:

Nandika A. D'Souza, Major Professor
Marta Drewniak, Committee Member
Bruce Gnade, Committee Member and
Chairman of the Department of Materials Science
Zhibing Hu, Committee Member
David Hunn, Committee Member
Richard F. Reidy III, Committee Member
C. Neal Tate, Dean of the Robert B.
Toulouse School of Graduate Studies

Hernandez-Luna, Alejandro. Structure property and deformation analysis of polypropylene montmorillonite nanocomposites. Doctor of Philosophy (Materials Science), May 2003. 132 pages, 15 tables, 53 figures, 142 references

Nanocomposites with expandable smectites such as montmorillonite layered silicates (MLS) in polymer matrices have attracted extensive application interest. Numerous MLS concentrations have been used with no particular justification. Here, we investigate the effects of MLS dispersion within the matrix and on mechanical performance. The latter is resolved through a three-prong investigation on rate dependent tensile results, time dependent creep results and the influence of a sharp notch in polypropylene (PP) nanocomposites. A fixed concentration of maleated polypropylene (mPP) was utilized as a compatibilizer between the MLS and non-polar PP. Analysis of transmission electron micrographs and X-ray diffraction patterns on the surface and below the surface of our samples revealed a unique skin-core effect induced by the presence of clay. Differential scanning calorimetric and polarized optical microscopic examination of spherulites sizes showed changes in nucleation and growth resulting from both the maleated PP compatibilizer and the MLS. These structural changes resulted in a tough nanocomposite, a concept not reported before in the PP literature. Nonlinear creep analysis of the materials showed two concentrations 3 and 5 % wt of PP, which reduced the compliance in the base PP. The use of thermal wave imaging allowed the identification of ductile failure among materials, but more important, aided the mapping of the elastic and plastic contributions. These are essential concepts in fracture analysis.

ACKNOWLEDGMENTS

It has been more than 4 years since I joined the department of Materials Science at the University of North Texas. Finally I am close to fulfilling the goal I have had since that day. The road was not easy, and I am sure I could have not made it without the help and support of certain people that helped me along my way.

First of all I would like to thank to Dr. Nandika A. D'Souza for her continue advice and support, but mainly for her patience. I appreciate the way she forced me to do things in order to understand the physical meaning of each concept, and for giving me the opportunity to participate in a very exciting project that opened my mind to a variety of concepts in the materials science world. I also owe her for the opportunity of gaining experience outside of the university, in the real world. Thank you very much Dr. Nandika for all your support in the good, but mainly in the bad moments.

I appreciate the support and advice of each of my committee members Bruce, Rick, both of them my professors for the knowledge they shared with me; Dr. Hu who cooperated freely to evaluate my work but special thanks to Dr. David Hunn and Dr. Marta Drewniak for their time and the materials support. This work could not be finished without your help. I hope you find some reward in it.

I cannot forget to thank to Dr. Rollie Schaffer, who was my first contact at UNT, when I first tried to come to the USA. Also, I appreciate the support that CONACYT, the Mexican council of science and technology, for supporting me the first years of my studies.

From my time here, I will always remember the support, advice and jokes of my friends Rosie, Dr. Manuel, Dr. PP (Praka), Gaurang, Soumitra, Dr. Jesus, Peter, Ajit (who helped me with much of my analysis), Dr. Dora, another Peter, Alberta, Dr. Oscar and to all the folks that in some way contributed to this goal. It was a great time having you all around.

Also, I want to thank to my family; my parents Juan Antonio and Martha, as well as to Laura, Antonio, Melissa, and Martha Laura, for the unconditional support and motivation to reach my goal. I do not know what would have been of me without your continuous cheers.

Finally, I want to thank to the person who has brought light to my days and that in her very special way has supported me to the end in order to reach my goals. Thanks "Aga", for all that you have done for me, and for believing in me. I will do my best for keeping you believing.

TABLE OF CONTENTS

LIST OF TABLES

LIST OF FIGURES

CHAPTER 1

OVERVIEW

A composite material is generally described as a combination of two or more phases at the macroscopic level, which will result in an improved system with superior characteristics than that of its individual components by themselves. However, such a generalized concept should be more clearly defined to include the scale of the reinforcements, since systems can be reinforced chemically at both microscopic and nanoscopic levels.

Nanocomposites are a relatively new category of composites that have gained recognition in recent years, due to their unique reinforcement properties. They are based on the use of a low concentration of expandable smectite clays, such as montmorillonite layered silicates (MLS), in the matrix [1-34]. Multifunctional benefits such as mechanical performance, oxygen permeability resistance and flame retardant characteristics are obtained simultaneously. Once expensive, nanocomposites are becoming more cost effective when low cost materials, such as polypropylene (PP), are used as a matrix.

PP has been used due to its low cost and good performance. With the addition of MLS, a cost effective structural material can be obtained. PP nanocomposites have found a special place in the automotive industry, where its flexibility and low density have been used as substitute for metallic parts. A tough nanocomposite will promote diversification of PP in the automotive and other industries.

The addition of MLS in a polymeric matrix results in different clay distributions that do not always provide an improvement in performance. When MLS is added to a

polymer, it remains an immiscible system. However, pioneering work by Toyota showed that surfactant-treated MLS is capable of hydrophobic interactions leading to partially-or completely-dispersed composites [2, 4]. The different clay distributions are the immiscible, intercalated, partially exfoliated and exfoliated dispersions. They are further explained in the next chapter. In general, exfoliated structures have resulted in better performance, and are often sought as the desired structure in the final nanocomposite.

A wide range of MLS concentrations have been tried in the quest for the ideal system that combines low concentration with good mechanical performance. The paradox that nanocomposites face mirrors the one that long fiber-reinforced composite technology faced earlier: how to obtain both strength and toughness in the same system. The bulk of nanocomposite literature [1-33] indicates that increased strength, or elastic modulus, considerably decreases strain to failure and ductility. In PP, this is further complicated by the non-polar nature of PP, requiring the use of bridge molecules between the PP and the MLS. Prior studies have focused on using high concentrations (above 5 % by wt of PP) [32-33] of polar compatibilizer, for example maleated polypropylene (mPP) [32-34]; the reasoning being that the polar compatibilizer would solubilize the MLS surfactant. This should increase the degree of reinforcement between polymer chains and layered silicate structures. The reality is that the low molecular weight compatibilizer reduces the stiffness and toughness of the material.

In this work a new approach has been proposed to reach a more stable system; reduction to 2 wt % of compatibilizer and vary the MLS concentration between 1% and 5%. Prior research has indicated that at concentrations greater than 5 wt %, the high volume fraction of MLS causes an increase in edge platelet interactions [34]. This

architecture would nullify the benefit of nanocomposites. To evaluate the degree of exfoliation in the matrix, transmission electron microscopy (TEM) and X-ray diffraction (XRD) analysis were conducted. What started as a routine evaluation of MLS dispersion by XRD, revealed significant changes in the matrix due to the semicrystalline nature of PP. In a more detailed analysis, the dispersion in the XRD peaks of PP was correlated to the occurrence of a skin-core effect.

A central issue affecting technological applications of polymers as structural elements is their time dependent effects. Therefore, mechanical analysis followed two paths. The quasi-static response of nanocomposites was examined by determining the elastic limit, yield strength, ultimate tensile strength, and elongation to failure and fracture toughness. Fracture toughness, has always been considered a negative property for most nanocomposites. Preliminary results from tensile tests showed retention of the original basic properties (Young's modulus, ultimate tensile strength, etc). One sample, containing 5 % wt of MLS, showed both high strength and high ductility, mirroring the base compatibilized PP.

Long-term time dependence was examined through creep-recovery measurements. The analysis showed that the addition of MLS limited the increase in compliance of PP induced by the compatibilizer. Furthermore, the compliance loss was significantly recovered at higher concentrations of MLS.

A purely quantitative evaluation of these tests, while providing the information required for understanding the properties of the investigated materials, did not completely explain the reason for the time dependent behavior. The study of the immediate structural effects induced in materials by the application of external stresses is hard to

follow. One of the best approaches is to stop a test in progress and analyze the sample for structural changes, but instantaneous changes cannot be followed by this technique. A novel non-contact technique, thermal wave imaging (TWI), has been used to follow the structural changes in the specimens while they are being tested. As opposed to photoelastic image analysis, TWI is able to image non-transparent specimens. TWI equipment is based on measurement of the emissivity of materials and changes these values to temperature, providing profiles that allow the detection of structural changes in the material. A brief analysis using this technique has been done to show how two specimens that have similar failure mechanisms undergo different structural transformations while failing.

The objective of this dissertation is therefore to understand the deformation, rate effects and crack presence in PP nanocomposites. Since nanocomposite performance is tied to the dispersion of MLS layers in the matrix, XRD was conducted in conjunction with TEM. Resolution of different inferences implied by these two techniques led to the analysis of samples with and without the surface layer. This analysis led to the determination of a unique skin-core effect. Mechanical tensile testing was used to determine macro-mechanical properties. In order to understand the influence of cracks in nanocomposites on deformation, fracture toughness techniques were applied. Creep tests revealed non-linearity induced by the compatibilizer, but the non-linearity is counteracted to a certain extent by the MLS. Deformation analysis was done using real time thermal wave imaging. The results indicate that nanocomposite performance does not scale with concentration of the MLS. Particularly in PP, crystalline effects strongly affect performance induced by MLS presence and mPP.

References

1. Pinnavaia TJ. Science 1983; 220 (4595): 365-371.
2. Kornmann X. ESCM newsletter 4.
3. Alexandre M, Dubois P. Mater Sci Eng R 2000; 28:1-63
4. Pinnavaia TJ, Beall GW. Polymer clay nanocomposites. New York. John Wiley and Sons 2000 (Chapters 7- 8).
5. Vaia RS, Jandt KD, Kramer EJ, Giannelis EP. Chem Mater 1996; 8: 2628-2635.
6. Tjong SC, Meng YZ, Hay AS. Chem Mater 2002; 14: 44-51.
7. Okada A, Kawasumi M, Usuki A, Kojima Y, Marauchi T, Kamigaito O. Mater Res Soc Proc 1990; 171 :45-50.
8. Lagaly G. Applied Clay Sci 1999; 15:1-9
9. Wang Z, Pinnavaia TJ. Chem Mater 1998; 10: 1820-1826.
10. Fong H, Vaia RA, Sanders JH, Lincoln D, Vreugdenhil AJ, Liu W, Bultman J, Chen C. Chem Mater 2001; 13: 4123-4129.
11. Manias E, Touny A, Wu L, Strawhecker K, Lu B, Chung TC. Chem Mater 2001; 13: 3516-3523.
12. Shi H, Lan T, Pinnavia TJ. Chem Mater 1996; 8: 1584-1587
13. Tabtiang A, Venables RA. Polymer 2002; 43 (17): 4791-4801.
14. Ichazo MN, Albano C, Gonzalez J, Perera R, Candal MV. Compos Struct 2001; 54: 207-214.

15. Gonzalez-Montiel A, Keskkula H, Paul DR. Jour Polymer Sci 1995; 33: 1751-1767.
16. Vaia RA, Teukolsky RK, Giannelis EP. Chem Mater 1994; 6(7): 1017-1022
17. LeBaron PC, Wang Z, Pinavaia T. Applied Clay Sci 1999; 15: 11-29.
18. Liu Y. J, Schindler JL, DeGroot DC, Kannewurf, CR, Hirpo W, Kanatzidis MG. Chem Mater 1996; 8; 525-534.
19. Dennis HR, Hunter DL, Chang D, Kim S, White JL, Cho JW, Paul DR. Polymer 2001; 42: 9513-9522.
20. Kurokawa Y, Yasuda H, Kashiwagi M, Oyo A. Jour Mater Sci Letters 1997; 16: 1670-1672.
21. Kornmann X, Berglund LA, Sterte Jour Polymer Engin Sci 1998; 38(8): 1351-1358.
22. Dagani R. Chem Engin News 1998, Sept 21st: 70-77.
23. Gilman JW, Kashiwagi T, Lichtenhan JD. SAMPE Jour 1997; 33(8): 40-46.
24. Asselman T, Garnier G. Colloid Surf A 2000; 170: 79-90.
25. Hambir S, Bulakh N, Kodgire P, Kalgaonkar R, Jog JP. Jour Polymer Sci Part B. Polymer Phys 2001; 39: 446-450.
26. Fu X, Qutubuddin S. Polymer 2001; 42: 807-813.
27. Foresta T, Piccarolo S, Goldbeck-Wood G. Polymer 2001; 42: 1167-1176.
28. Maiti P, Nam PH, Okamoto M, Hasegawa N, Usuki A. Macromolecules 2002; 35: 2042-2049
29. Nam PH, Maiti P, Okamoto M, Kotaka T, Hasegawa N, Usuki A. Polymer 2001; 42: 9633-9640.

30. Tidjani A, Wilkie CA. Polymer Degrad Stab 2001; 74: 33-37.

31. Saujanya C, Radhakrishnan S. Polymer 2001; 42: 6723-6731.

32. Wang H, Elkovitch M, Lee LJ, Koelling KW. SPE ANTEC conf 2001; Dallas, TX

33. Wang H, Zeng C, Svoboda P, Lee JL. SPE ANTEC 2000. Orlando, FL.

34. Butzloff P D'Souza NA, Golden TD, Garrett D. Polymer Engin Sci 2001; 41: 1794

CHAPTER 2

COMPOSITE MATERIALS AND THEIR CHARACTERIZATION

2.1. Composites

"A composite is basically a system composed of two or more different individual phases with distinctive characteristics"

All composites have two basic components, the matrix or host, and the reinforcement or filler. The matrix is the element giving shape to the composite, and performs as a load transfer medium to the filler. The filler is designed to optimize selected mechanical properties of the composite. Sandwich composites are an exception to this classification, since they could be constituted as individual layers independent from one another. In this case, a bonding phase is also a constituent that could affect the final performance of the entire system.

Composites can be easily divided in several subcategories. According to the materials used they can be metal, ceramic, or polymer matrix composites. Based on the reinforcement scale, they could be long fiber, short fiber or nanocomposites. Subcategories can be defined according to the metal, ceramic or polymer used. For instance, in polymers the matrix can be a thermoset or thermoplastic. Some basic definitions and divisions are briefly explained below.

According to the size of the reinforcement, composites can be divided into:

-Macroscopic composites: when the phases can be easily distinguished from one another without the use of a magnifying instrument, as in glass fiber composites.

-Microscopic composites: Composites that generally have a matrix with the reinforcement phase embedded in the matrix. Both phases are separate, but for a clear observation, microscopic techniques are used. Cermets belong to this class of composite.

- Nanocomposites: Systems where at least one of the dimensions of the reinforcement phase is nanometric.

Different reinforcements can be used to create composite systems and also as a way to classify them. Reinforcement phases can be different materials as glass, carbon or graphite in fiber form [1-5]. Fiber composites are defined as composites where the fibers could be long or short, unidirectional, planar or three dimensional. In flake or platelet composites, the reinforcement architecture is such that one of the dimensions, generally the thickness, is much smaller than the other two. In particulate composites, the reinforcement is microscopic, all dimensions are similar. Laminar composites are generally formed with no matrix and are composed for several panels, with identical dimensions in a sandwich-like structure. Each panel could be a composite itself.

There are also different kinds of bonding in the composites. According to the joining, or bonding, of each of the phases, two main characterizations can be found. Physically-bonded composites are those where there is no chemical bonding among phases, and the load in the composite is transferred by the action of physical forces. In chemically bonded composites, there is a chemical interaction among the different components. Each composite phase can be a composite itself. By combining one or more of the divisions mentioned before, new groups or divisions can be found or created, but all of them have an essential purpose: optimize the performance of the resulting system.

2.2. Nanocomposites

The addition of particles to polymers has been a common practice for several years now [6-9]. This is done for several reasons that include changing the color, decreasing the viscosity to aid the manufacturability of parts, and increasing the structural properties, etc. Nanocomposites are, in principle, a result of these practices. A nanocomposite generally defines a two-phase system in which at least one of the dimensions of one of the phases is of the order of a nanometer (10^{-9} m) [1-6]. Since researchers at Toyota [16] realized the possibility of synthesizing a nanostructure from a polymer and organophilic layered silicate, different attempts have been made to add diverse nanomaterials to polymers in order to modify several of their properties [10-21].

Different forms of fillers can be used in a polymeric matrix:

- Particles: calcium carbonate, in natural or synthetic form
- Fibers: glass fibers, carbon fibers, and other processed minerals
- Plate-shape particles: kaolin, mica talcum, and aluminum hydroxide.

Some of these materials have to be surface-modified by means of coupling agents in order to make the inorganic material compatible with the polymer. [17]

Among them, MLS have the ability to form organic-inorganic nanocomposites because they are expandable, and capable of swelling in a variety of host matrices. MLS are chemically resistant and possess a high aspect ratio and high strength, which is very desirable for a reinforcement agent. Used commonly as additives, they have the ability to intercalate among the polymeric chains of the matrix. Silicates such as montmorillonite, hetotite, magadite, vemiculite and mosco-clay are examples of nanometric structures used as reinforcements. [14-21]

However, some polymers cannot interact with the silicate particles resulting in immiscible blends. These blends can be compatibilized by the addition of reactive additives that will lead to the formation of interface active species. Maleic anhydride grafted polyolefins are the most common compatibilizer used. [22-24, 38]

Nanocomposites have shown additional advantages over conventional macroscopic composites. Most of the emphasis has focused on the improvement of the mechanical properties of the different systems. These properties include an increase in the mechanical performance where tensile strength has increased and the elastic modulus has almost doubled [16]. A decrease in the permeability of the nanocomposite has been a primary advantage of the technology [11, 12, 16, 26]. The decreased permeability is due to an increased path length for the medium due to the MLS platelets in the path. The addition of MLS improved resistance to organic solvents, as toluene and chloroform, as well as increased the heat distortion temperature, reduced the thermal expansion coefficients, and improved the flame retardance and wear resistance [11-13, 28, 29]. Due to the light refraction nature of the fillers used, these composites are generally optically opaque, but due to the degree of molecular interaction it is possible to obtain nanocomposites with a good degree of transparency.

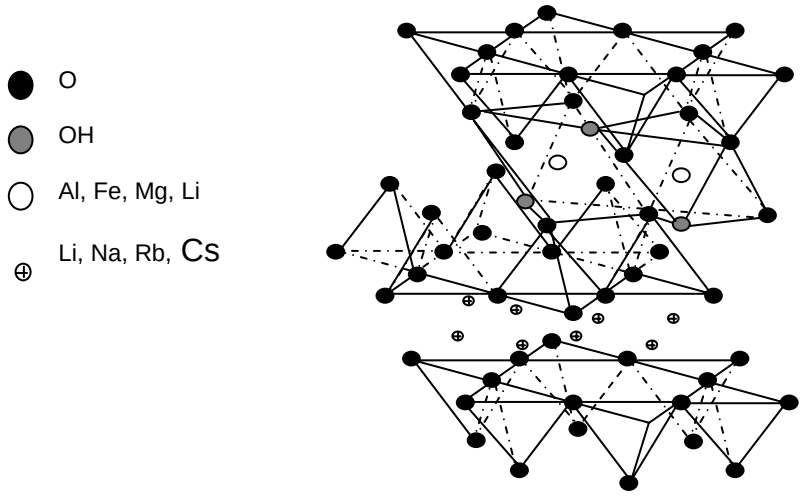

Figure 2.1. Structure of 2:1 phyllosilicates. Used with permission of the American Chemical Society. [11]

2.2.1. Montmorillonite

The common silicates used as reinforcement in the nanocomposites are from the family of phyllosilicates. The crystal lattice consists of two-dimensional layers where a central octahedral sheet of alumina or magnesia is fused to two external silica tetrahedron by the tip, so that the oxygen ions of the octahedral sheet also belong to the tetrahedral sheets [12]. One of the most common layered silicates used is montmorillonite [$M_x(Al_{4-x}Mg_x)Si_8O_{20}(OH)_4$, where M is a monovalent cation and x is the degree of isomorphous substitution]. Its structure is shown in figure 2.1. This type of MLS is characterized by a moderate negative surface charge. The charge of the layer is not locally constant as it varies from layer to layer and must be considered as an average value over the whole crystal. Proportionally, even if a small part of the charge balancing cations are located on the external crystallite surface, the majority of these exchangeable cations are located inside the galleries. Once the hydrated cations are ion-exchanged with organic cations (such as alkyl ammonia molecules), it usually results in a higher interlayer spacing. For

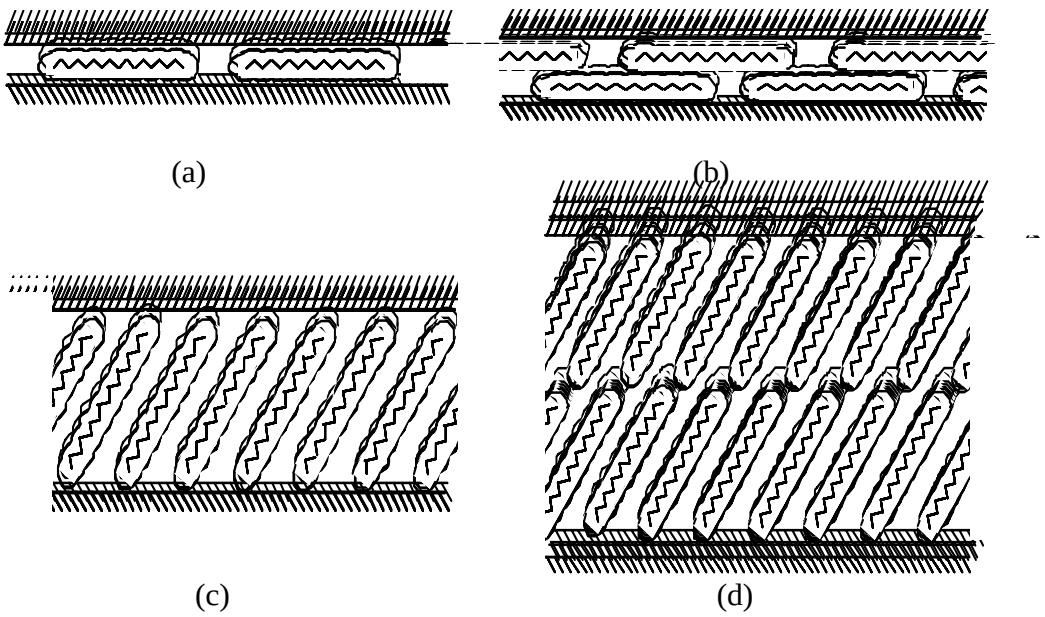

Figure 2.2. Alkyl chain aggregation in layered silicates: (a) lateral monolayer; (b) lateral bilayer; (c) paraffin-type bilayer.; d) paraffin-type bilayer. Used with permission ACS editors from [14]

the description of the structure in the interlayer of the organoclay, it is necessary to understand that as the negative charge originates in the silicate layer, the cationic head group of the alkylammonium molecule preferentially resides at the layer surface, leaving the organic tail radiating away from the surface. In a given temperature range, two parameters define the equilibrium layer spacing: the cation exchange capacity of the layered silicate, driving the packing of the chains, and the chain length of the organic tails. X-ray diffraction data has shown evidence that suggests that the chains lie parallel to the silicate layer forming mono or bilayers. Depending on the packing density and the chain length, the chains may radiate away from the surface, forming mono or even bimolecular tilted paraffinic arrangements, as shown in figure 2.2.

Vaia et al., [25] by means of FTIR studies proposed a more accurate structure. They found that the intercalated chains exist in states with varying degrees of order. As

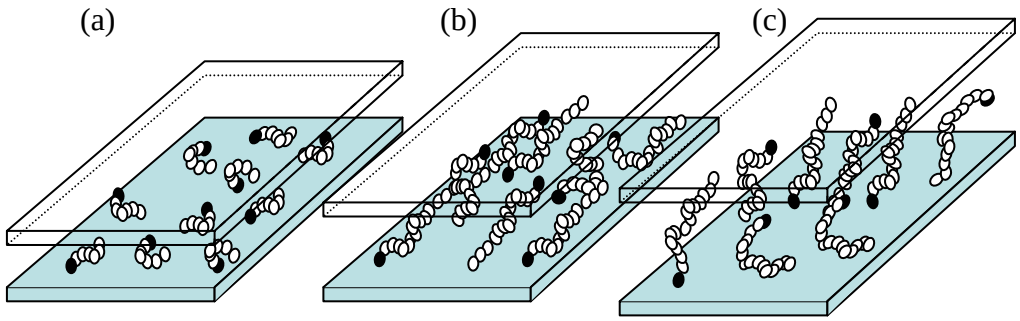

Figure 2.3. Alkyl chain aggregation models (a) short alkyl chains. Isolated molecules, lateral monolayer. (b)intermediate chain lengths: in plane disorder and interdigitation to form quasi-bilayers and (c) longer chain length: increased interlayer order, liquid crystalline-type environment.
Used with permission ACS editors from [14]

the length, or density, of the chain decreases, the intercalated chains acquire a more disordered liquid-like structure. If the surface area per molecule is within a certain range, the chains are not completely disordered, but retain a certain degree of order similar to a liquid in its crystalline state. In figure 2.3, the three different chain configurations are shown.

2. 2. 2. Nanocomposite structures

Nanofillers can self assemble in different ways in the matrix, depending upon the nature of the MLS and the way the nanocomposite is prepared. Three structures have been defined, phase separated (immiscible), intercalated and exfoliated [10-29] and are shown in figure 2.4.

In a phase separated structure the layered silicate and the polymer form a heterogeneous structure, where the polymer surrounds several layers of the MLS

structure. It is possible that the polymer chain and a particle of MLS alternate in the structure keeping a certain degree of order. This is known as an intercalated structure, and the distance between each silicate layer is fixed and in the nanometer range. In an exfoliated nanocomposite there is no order in the MLS within the polymer. The distance between MLS particles is larger, and they are oriented in different directions if there are regions having similar orientation within the exfoliated nanocomposites it is known as an ordered exfoliated structure. Some authors [28] refer to this later nanocomposite as a disordered intercalated composite.

To determine which structure of nanocomposite is obtained, the interlayer spacing needs to be determined. This can be done with TEM, with the interlayer spacing calculated from the image. X-ray diffraction is another technique that can provide information to a certain degree. Being crystalline, the MLS has a specific diffraction pattern. In the case of MLS nanocomposites, there is a low scattering angle region where

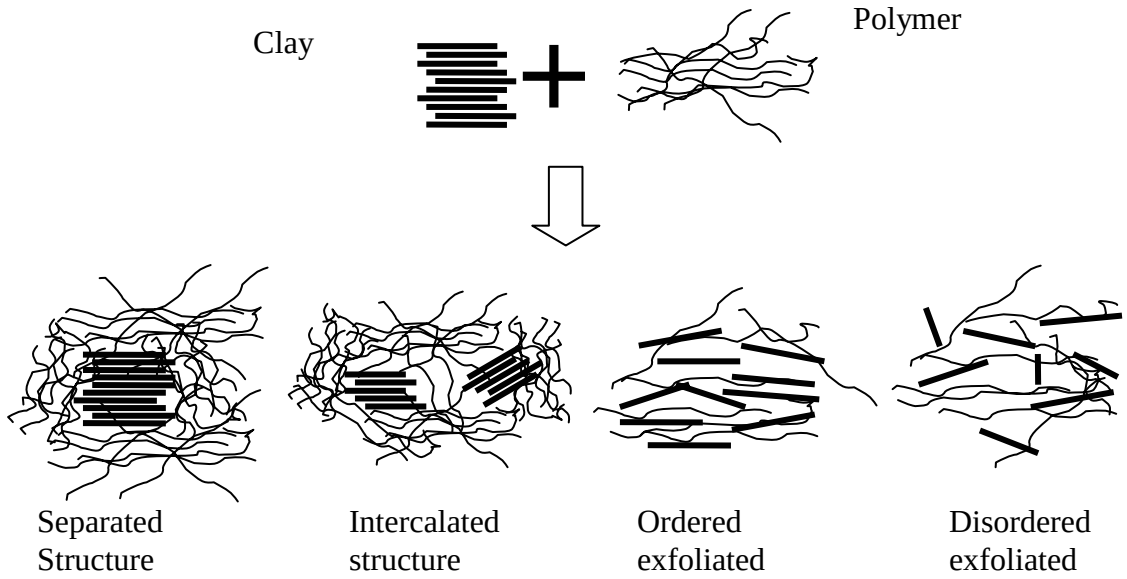

Figure 2.4. Nanocomposite structures [11-13]

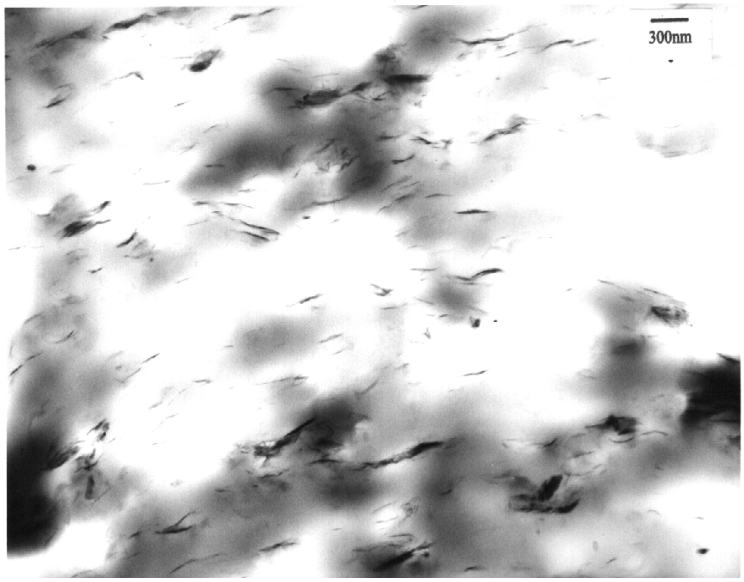

Figure 2.5. TEM image of a PP nanocomposite.

the MLS has very characteristic peaks, below 2θ angles of 10° corresponding to the interlayer spacing [12-14, 21-40]. As the MLS is dispersed or disordered in the matrix, the intensity of these peaks decreases until at some point they completely disappear.

A combined polymer and MLS system retaining the peaks at low 2θ values is indicative of an immiscible nanocomposite. An intercalated ordered structure is characterized by a decrease in the intensity of the peaks and an increase in the interlayer spacing. A disordered exfoliated structure will have no peaks in this region. Since all experiments need verification, XRD and TEM are utilized to characterize the dispersion of the MLS.

2.2.3. Mechanical properties

The first report of improved mechanical properties was made by the Toyota researchers in 1980 [16] when they found an increase of almost 100 % in the modulus of polyamide 6 clay nanocomposites, with a reinforcement of 4% of MLS. Multiple polymer –MLS systems have resulted using different MLS, and the degree of reinforcement (MLS

percentage) obtained either increases, decreases or stays the same in the elastic modulus, ultimate tensile strength, and yield strength of the systems investigated [11-33, 41-44]. The differences have been attributed to the degree of exfoliation of the layered silicate in the polymeric matrix, and to the surface area of the inorganic phase [10-45] and, more recently to the mobility of the nanofiller particle [45]. Also, in the case of increased stiffness of epoxy systems, the increase in effective particle volume fraction in the nanocomposite plays an important role. In a microcomposite the interlamellar spacing of the layered silicate remains constant, while in the nanocomposite, the interlamellar spacing increases, so the effective particle volume fraction becomes much larger than the initial particle volume fraction.

As mentioned before, the formation of a nanocomposite is dependent on the dispersion of the silicate layers, but that does not guarantee, an improved material. Attaining one property, such as optical transparency, could come at the expense of another property such as mechanical performance. Only the final application can determine if an improvement has been reached for multifunctional goals.

2.2.4. Polymer nanocomposites

Different polymers have been modified with MLS in order to obtain a better performance in specific applications. Some of these systems are listed below.

A variety of clays have shown a very high degree of reinforcement in epoxy systems [37, 38]. Alliphatic amine, aromatic amine, anhydride and catalytic curing agents have been used to form epoxy matrices with broad glass transition temperatures. However, a more effective application of this nanolayer has been found in the mechanical

properties when the polymer is in the rubbery state. The dimensional stability, thermal stability and solvent resistance on the glassy matrix can be improved when the MLS nanolayers are present.

In the case of the polyimide systems, the use of nanocomposites resulted in an increase in the barrier properties and thermal stability [12, 26]. Depending on the kind of clay used, the degree of intercalation or exfoliation in the systems will vary. Regardless of the degree of dispersion of the silicate layers, mass-transport studies of polyimide-clay nanocomposites revealed a reduction in the permeability of small gases such as oxygen, helium, carbon dioxide and the organic vapor ethyl acetate [17] with the presence of low concentrations of clay in the system. Changes in the coefficient of thermal expansion have also been found in these systems, using low concentrations of MLS.

Several other systems should be mentioned, for instance polyurethane-clay, polystyrene-clay, polyethylene terephthalate-clay, liquid crystal-clay, and PP-clay systems [11, 12, 13, 26]. All of them have a different degree and kind of reinforcement; while the permeability barriers are increased in polyethylene terephthalate, the mechanical performance can be increased in the other systems. Basically, as the clay is added in different polymers, different features can be obtained.

A more thorough review will be done for the PP nanocomposites, since this is the subject of study in this work. I am primarily concerned with the failure mechanisms of these systems.

2.3. Polypropylene

PP is a semicrystalline polymer with a sub-ambient glass transition temperature. When using polymers, an important factor to consider is the processing method, but even

more important is the final structure obtained, since the resulting physical properties of the material will be highly dependent on it. The crystallization of a semicrystalline polymer involves two stages [48], primary and secondary crystallization. In primary crystallization, crystal formation is a function of two submechanisms, primary and secondary nucleation. Primary crystallization is assumed to be complete when no additional molecular stems can transport onto a growth face. Secondary crystallization refers to any process that leads to a further increase of crystallinity.

Structural changes in PP can be followed using X-ray diffraction [40]. Pure PP, with no filler shows five peaks in the 2θ range between 10° and 30° which correspond to a monoclinic α phase. The addition of filler can modify the relative intensity of these peaks, as in the case of nanocomposites, where the intensity of peak II is highly impacted, as the filler size decreases the intensity of peak II increases [59, 60]. The monoclinic α phase is the most studied phase, but other phases include hexagonal β and triclinic γ phases [49]. This will be illustrated in the next chapter.

2.4 Polypropylene nanocomposites

PP nanocomposites have been prepared by in-situ polymerization or melt processing. In order to obtain a nanocomposite with improved mechanical properties, a stacked layer structure of MLS separated into monolayers, in a polymer matrix is more easily achieved. With this dispersion, an increment in the aspect ratio is obtained and reinforcement effects enhanced. Bonding between the MLS and the matrix requires control of the interfacial affinity between the MLS particle surface and the matrix of the polymer. The influence of the MLS on termination rates of PP polymerization has made

the first option difficult. In the case of melt processing, the non-polar nature of the propylene repeat unit renders intercalation of the chains between the silicate layers difficult (i.e. in site polymerization). Blending PP with maleated PP (mPP) or styrene acrylonitrile (SAN) are two of the most often followed routes [50]. Poor mechanical properties in SAN modified systems has led to increased interest in mPP.

mPP has proven effective in PP + glass fiber composites, as I have previously investigated [42]. The maleic anhydride segment is compatible with the alkyl ammonium salt, while the PP is compatible with the PP host. Exfoliation of the smectite MLS is enabled through migration of the mPP between the MLS sheets. To compound these systems, two methods are followed. In one method, the mPP is blended with the smectic MLS to form an exfoliated system, which is then mixed into PP. In the second method, a three component system is compounded together.

The first method is followed more commonly, based on the premise that exfoliation of the MLS is highly likely in mPP + MLS mixtures. I however, chose to follow the latter to mitigate a possible phase segregation of the MLS + mPP in the master batch.

No direct intercalation of PP in simply organically modified layered silicates has been observed. Being non polar, to interact with the modified layers, either maleic anhydride or hydroxyl groups should be used in order to reach the melt intercalation [55, 56]. It is known that the main characteristic of nanocomposites is that an improvement of the general properties can be reached with small addition of MLS [10-40]. Also, as the MLS content increases, exfoliation becomes more difficult due to the amount of particles in the system. Thus, low MLS concentrations are key. In addition, there have been

studies where it has been shown that a high level of MLS content (up to 50 %) does not lead to an improvement of the properties, decreasing the original mechanical performance of the material [58].

Different techniques can be used to obtain a PP nanocomposite [13] such as mechanical shear, solvents, and monomer intercalation. An important reason for studying nanoparticle filled nanocomposites is that the fracture mechanisms in these systems may be quite different from conventional composites. It has been speculated that the rigid particles will resist the propagation of cracks, causing them to bend between the particles. However, when these rigid particle sizes are in the nanoscale region, this concept is questionable, requiring resolution.

Some of the previous research in PP nanocomposites can be summarized using the work of Wang et al. observed in table 2.1 where low concentration of MLS (5 %) but high concentrations of compatibilizer are used [41, 42]. Different types of MLS and compatibilizer were used. Also included are results for PP and the compatibilizer by themselves.

This work suggests that the compositions with the highest degree of improvement are composites 5 and 6, with high ultimate tensile strength. However, if attention is paid to nanocomposite number 7; it can be observed that even when the tensile strength and the elastic modulus are not as high as the other two, it has the highest impact strength. These results indicate high compatibilizer concentration will not result in a higher impact resistance, which could be extended to another property, fracture toughness. Thus, our experimental plan utilizes low mPP concentration.

Table 2.1 Mechanical Properties of PP nanocomposites. Data from Wang et al. [42]

MATERIAL	Tensile Strength (MPA)	Elastic Modulus (MPA)	Impact strength (Izod) (J/m)
1. PP	34.2 ± 0.2	1680 ± 10	19 ± 2
2. PB 3150	31.7 ± 0.2	1580 ± 60	
3. PP/20A(95/5)	35.7 ± 0.2	2060 ± 70	22 ± 2
4. PP/E43/20A (80/15/5)	36.6 ± 0.2	2400 ± 100	16 ± 2
5. PP/PB3200/20A (80/15/5)	38.2 ± 0.3	2500 ± 70	21 ± 2
6. PP/PB3150/20A (80/15/5)	39.0 ± 0.6	2440 ± 20	23 ± 2
7. PP/PB3150/20A (90/5/5)	36.3 ± 0.1	2220 ± 80	24.7 ± 1
8. PP/PB3150/I30 (80/15/5)	33.8 ± 0.2	1900 ± 100	14 ± 2
9. PP/PB3150/nylon 6/I3((80/15/5)	30.0 ± 0.2	2000 ± 30	13 ± 2

References

1. Smith WF. Principles of materials and engineering, 2nd ed. New York. McGraw Hill, 1990 (chapters 6, 7 and 13).
2. Heracovich CT. Mechanics of fibrous composites. New York. John Wiley and Sons, 1998 (chapter1).
3. Schwartz MM. Composites materials handbook. New York. McGraw Hill, 1984 (chapters 1 and 2).

4. Shakelford JM. Introduction to materials science for engineers, 4th ed. London. Prentice Hall 1996 (chapter 10).
5. Hull D, Clyne TW. An introduction to composite materials, 2nd ed. Cambridge. United Press 1996 (chapter 1).
6. Seymour RB, Carraher CE. Structure property relationships in polymers. New York. Plenum Press 1984 (chapter 3, 5, and 12).
7. Bikales NM. Mechanical properties of polymers. New York. John Wiley and Sons 1971 (chapter 1 and 3).
8. Rosen SL. Fundamental principles of polymeric materials. New York. Barns and Noble1971 (chapter 17 and 18).
9. Billmeyer FW. Textbook of polymer science, 2nd ed. New York. John Wiley and Sons 1970 (chapter 4, 6 and 7).
10. Pinnavaia TJ. Science 1983; 220 (4595): 365-371.
11. Kornmann X. ESCM newsletter 4.
12. Alexandre M, Dubois P. Mater Sci Eng R 2000; 28:1-63
13. Pinnavaia TJ, Beall GW. Polymer clay nanocomposites, John Wiley and Sons 2000 (Chapters 7- 8).
14. Vaia RS, Jandt KD, Kramer EJ, Giannelis EP. Chem Mater 1996; 8: 2628-2635.
15. Tjong SC, Meng YZ, Hay AS. Chem Mater 2002; 14: 44-51.
16. Okada A, Kawasumi M, Usuki A, Kojima Y, Marauchi T, Kamigaito O. Mater Res Soc Proc 1990; 171 :45-50.
17. Lagaly G. Applied Clay Sci 1999; 15:1-9
18. Wang Z, Pinnavaia TJ. Chem Mater 1998; 10: 1820-1826.

19. Fong H, Vaia RA, Sanders JH, Lincoln D, Vreugdenhil AJ, Liu W, Bultman J, Chen C. Chem Mater 2001; 13: 4123-4129.
20. Manias E, Touny A, Wu L, Strawhecker K, Lu B, Chung TC. Chem Mater 2001; 13: 3516-3523.
21. Shi H, Lan T, Pinnavia TJ. Chem Mater 1996; 8: 1584-1587
22. Tabtiang A, Venables RA. Polymer 2002; 43 (17): 4791-4801.
23. Ichazo MN, Albano C, Gonzalez J, Perera R, Candal MV. Compos Struct 2001; 54: 207-214.
24. Gonzalez-Montiel A, Keskkula H, Paul DR. Jour Polymer Sci 1995; 33: 1751-1767.
25. Vaia RA, Teukolsky RK, Giannelis EP. Chem Mater 1994; 6(7): 1017-1022
26. LeBaron PC, Wang Z, Pinavaia T. Applied Clay Sci 1999; 15: 11-29.
27. Liu Y. J, Schindler JL, DeGroot DC, Kannewurf, CR, Hirpo W, Kanatzidis MG. Chem Mater 1996; 8; 525-534.
28. Dennis HR, Hunter DL, Chang D, Kim S, White JL, Cho JW, Paul DR. Polymer 2001; 42: 9513-9522.
29. Kurokawa Y, Yasuda H, Kashiwagi M, Oyo A. Jour Mater Sci Letters 1997; 16: 1670-1672.
30. Kornmann X, Berglund LA, Sterte Jour Polymer Engin Sci 1998; 38(8): 1351-1358.
31. Dagani R. Chem Engin News 1998, Sept 21st: 70-77.
32. Gilman JW, Kashiwagi T, Lichtenhan JD. SAMPE Jour 1997; 33(8): 40-46.
33. Asselman T, Garnier G. Colloid Surf A 2000; 170: 79-90.

34. Hambir S, Bulakh N, Kodgire P, Kalgaonkar R, Jog JP. Jour Polymer Sci Part B. Polymer Phys 2001; 39: 446-450.

35. Fu X, Qutubuddin S. Polymer 2001; 42: 807-813.

36. Foresta T, Piccarolo S, Goldbeck-Wood G. Polymer 2001; 42: 1167-1176.

37. Maiti P, Nam PH, Okamoto M, Hasegawa N, Usuki A. Macromolecules 2002; 35: 2042-2049

38. Nam PH, Maiti P, Okamoto M, Kotaka T, Hasegawa N, Usuki A. Polymer 2001; 42: 9633-9640.

39. Tidjani A, Wilkie CA. Polymer Degrad Stab 2001; 74: 33-37.

40. Saujanya C, Radhakrishnan S. Polymer 2001; 42: 6723-6731.

41. Wang H, Elkovitch M, Lee LJ, Koelling KW. SPE ANTEC conf 2001; Dallas, TX

42. Wang H, Zeng C, Svoboda P, Lee JL. SPE ANTEC 2000. Orlando, FL.

43. Shia D, Hui CY. Polymer Composites 1998; 19(5): 608-617.

44. Duran JDG, Ramos-Tejada MM, Arroyo FJ, Gonzalez-Caballero F. Jour Colloid Interface Sci 2000; 229: 107-117.

45. Gersappe D. Phys Review letters 2002; 89(5): 1-4.

46. Lan T, Pinnavaia TJ. Chem Mater 1994; 6: 2216-2229.

47. Messersmith PB, Giannelis EP. Chem Mater 1994; 6: 1719-1725.

48. Supaphol, P. Spruiell, J. E. Polymer. 42. 2001. 699

49. Assouline E, Pohl S, Fulchiron R, Gerard JF, Lustiger A, Wagner HD, Marom G. Polymer 2000; 41: 7843-7854.

50. Messersmith PB, Giannelis EP. Chem Mater 1993; 5: 1064-1066.

51. Kojima Y, Fukumori K, Usuki A, Okada A, Kurauchi T. Jour Mater Sci Letters 1993; 12: 889

52. Tjong SC, Xu Y, Meng YZ. Jour Appl Polymer Sci 1999; 72: 1647-1653.

53. Tjong SC, Meng Y. Polymer Intern 1997; 42: 209-217.

54. Manning SC, Moore RB. Polymer Eng Sci 1999; 39(10): 1921-1929.

55. Li S, Jarvela PK, Jarvela PA. Polymer Engin Sci 1997; 37(1): 18-23.

56. Ginzburg VV, Balazs AC. Macromolecules 1999; 32: 5681-5688.

57. Vaia RA, Jandt KD, Kramer EJ, Giannelis EP. Macromolecules 1995; 28: 8080-8085.

58. Wong S, Ling C. SPE ANTEC 2002. San Francisco CA.

59. Hernandez-Luna A, D'Souza NA. SPE ANTEC 2002. San Francisco CA. 2002

60. Hernandez-Luna A, D'Souza NA. SAMPE 2002. Long Beach CA. 2002

CHAPTER 3

DISPERSION AND CRYSTALLIZATION EFFECTS IN POLYPROPYLENE MONTMORILLONITE NANOCOMPOSITES

3.1 Introduction

The objective of this chapter is to investigate the degree and type of dispersion obtained when MLS is incorporated into PP with mPP as the compatibilizer, and to understand the influence of MLS as a crystallization nucleation agent.

As highlighted in the previous chapter, two main structures can be obtained when MLS is dispersed in a polymer, exfoliated and intercalated. The intercalated structure preserves a short distance order and orientation among particles, while the exfoliated structure is characterized by a complete dispersion of the MLS in the polymeric matrix, and no orientation relationship among layers.

An intercalated structure results in an interlayer spacing corresponding to the lateral dimension of the polymer chain. Thus, the degree of reinforcement is localized. In order to obtain a reinforced polymer, an exfoliated structure is preferred [1-9]. Since the MLS is dispersed in the matrix, the interaction with the PP matrix and its reinforcement will be greater. In the classic theory of composites a logical reasoning would be that a higher degree of reinforcement leads to a more reinforced structure. However, the addition of higher MLS content will make exfoliation of the particles more difficult and agglomerated structures will result.

It has been already pointed out that the MLS particles are in the nanometric scale laterally, so in order to determine if a structure is either intercalated or exfoliated, precise methods are required to determine the distribution MLS particles. Most common

characterization techniques include one direct and an indirect method. The direct method is an image of the MLS itself, which can be obtained using transmission electron microscopy (TEM). Interlayer spacing can be obtained by XRD, where a backscattered signal provides information about the crystalline structure and orientation of ordered structures. TEM provides information about individual layers while XRD measures the arrangement of the entire MLS addition.

When nanometric particles are added to materials in low concentrations, no important changes in structure and performance are expected from purely physical interactions in each of the components since one is the host and the other the reinforcement. However, when a chemical interaction is induced in the system, structural differences can be expected. In PP nanocomposites, the use of a compatibilizer to bond the MLS and semicrystalline PP leads to structural changes affecting crystallinity and dispersion in the specimens. Crystallinity is determined using XRD, polarized light microscopy, and differential scanning calorimetry (DSC). The mixed structure of combined lattices should lead to distinctive properties in the material. I will address these concepts below.

3.2. Methods of nanocomposite characterization

3.2.1. XRD

XRD is mainly used in crystalline materials for structural identification. The theory is applicable to any material that shows a consistent, ordered structure. In non-crystalline, or semicrystalline materials this technique is used to probe structure, morphology, and degree of crystallinity. When the MLS particles are close to each other,

and with a preferred orientation (intercalated), the X-ray spectrum will show the presence of this structure together with the matrix. On the other hand if I can obtain a complete distribution of the particles, the absence of the repeated interlayer basal structure will imply an exfoliated dispersion.

3.2.2. Transmission electron microscopy (TEM)

TEM is the most common technique used in the analysis of nanocomposites because it directly shows the dispersion of the nanoparticles in the matrix. Most advanced composites are semicrystalline or amorphous materials, so the diffraction mode will provide no relevant information. In the image mode, the particles can be localized and imaged; this is a clear indication of the presence and distribution of the particles. From a TEM image, it is possible to observe the distribution of the MLS particles and calculate the distance between platelets.

3.2.3. Light microscopy

PP is a semicrystalline material; therefore, the spherulites show birefringence patterns in polarized light microscopy. Polarized light microscopy is a subclassification of reflecting light microscopy, and is based on the ability of the materials to rotate the plane of polarized light. Low magnification prevents its use to directly identify nanocomposite structures, but it has proven useful to follow the nucleation changes induced by the addition of a second particle into semicrystalline matrices.

3.2.4 Thermal analysis

Thermal analysis is used mainly in polymers, but can be extended to metals and some ceramics. These methods are commonly used to follow enthalpy changes due to annealing, quenching, crystallizing and other temperature dependent thermal processes. Thermal analysis can help in the identification of materials from analysis of the transition temperatures, and in the discovery of additional components that may be embedded in the base material.

The most common thermal technique is the differential scanning calorimetry (DSC). An average temperature circuit measures and controls the temperature of the sample and reference holders, following a predetermined programmed cycle. At the same time, the temperatures of the sample and reference are compared by a temperature differential circuit, and provide a feedback signal in order to keep the temperatures of both sample and reference equal when a thermal transition occurs. This power input is a direct measurement of the change in heat flow during the transition. In thermogravimetric analysis the weight loss as a function of temperature is measured. Both techniques are useful in determining glass transition, melting and decomposition temperatures.

3.3 Experimental

3.3.1. Sample preparation

PP + mPP + MLS nanocomposites were co-compounded using a Leitzcritz co-rotating twin-screw extruder. The series of samples investigated are shown in Table 3.1. The PP was a nucleated PP FINA 3925, while the mPP was Polybond 3150. The clay

was a montmorillonite layered silicate (MLS), Cloisite® 15A, obtained from Southern Clay. Compositions used are shown in table 3.1

Table 3.1. Composition of the specimens used.

Material	**PP**	**PP + mPP**	**mPP + MLS**	**NC 1**	**NC 2**	**NC 3**	**NC 5**
HPP	100	98		97	96	95	93
Polybond 3150		2	99	2	2	2	2
Cloisite®			1	1	2	3	5

PP = polypropylene. mPP = maleated PP. NC 1, 2, 3, 5 = nanocomposite 1, 2 ,3, 5 %

3.3.2. X-ray diffraction

X-ray diffraction was done on a Siemens D-100 instrument, using a step size of 0.05 with a Cu anode for 2θ ranging from 2 to 50 degrees.

3.3.3. Transmission electron microscopy

The TEM study was conducted on a JEOL JEM-100CX II electron microscope. A MT6000 Sorvall microtome was used to cut thin sections (less than 100nm thick) of the sample.

3.3.4. Differential scanning calorimetry

5 to 10 mgs of sample were heated from 30 °C to 200 °C at 10 °C/min. The sample was held at 200 °C for 30 minutes and then quenched to 30 °C at 50 °C /min. A second heat cycle was carried out from 30 °C to 200°C at 10 °C/min, held for 10 minutes at 200 °C and then cooled down to 30 °C at 10 °C/min. The purpose of the first run is to normalize the samples to remove any sample preinduced effects. The end heat and

cooling reflect the material properties. Experiments were carried out individually in a Perkin Elmer DSC7^{TM}.

3.5. Optical microscopy

Optical microscopy was conducted on a Zeiss polarizing optical microscope. The lens magnification was 40X. The same cycle as the DSC was followed. Photographs were taken using a CONTAX camera.

3.4. Results

3.4.1. X-Ray diffraction at surface

The XRD scans of the sample surfaces are shown in Figure 3.1. First considering the interaction between the interlayer spacing of the MLS and the PP + mPP blend, one can see that there was retention of the peaks at low 2θ angles (<5) in the samples of NC 1, NC 2, NC 3, and NC 5. There was also a slight shift to lower MLS interlayer d spacing or higher 2θ. I attribute this to the experimental error in obtaining the MLS spectra from a different batch of material. Comparing the full width at half maximum for this peak at 16 ° (Table 3.2) for the various samples, it can be seen that the width of the peak gradually increases with increasing MLS concentration. This indicates decreased structural regularity of the MLS interlayers in PP as the MLS concentration increased. Note the section corresponding to the XRD specimen in figure 3.2.

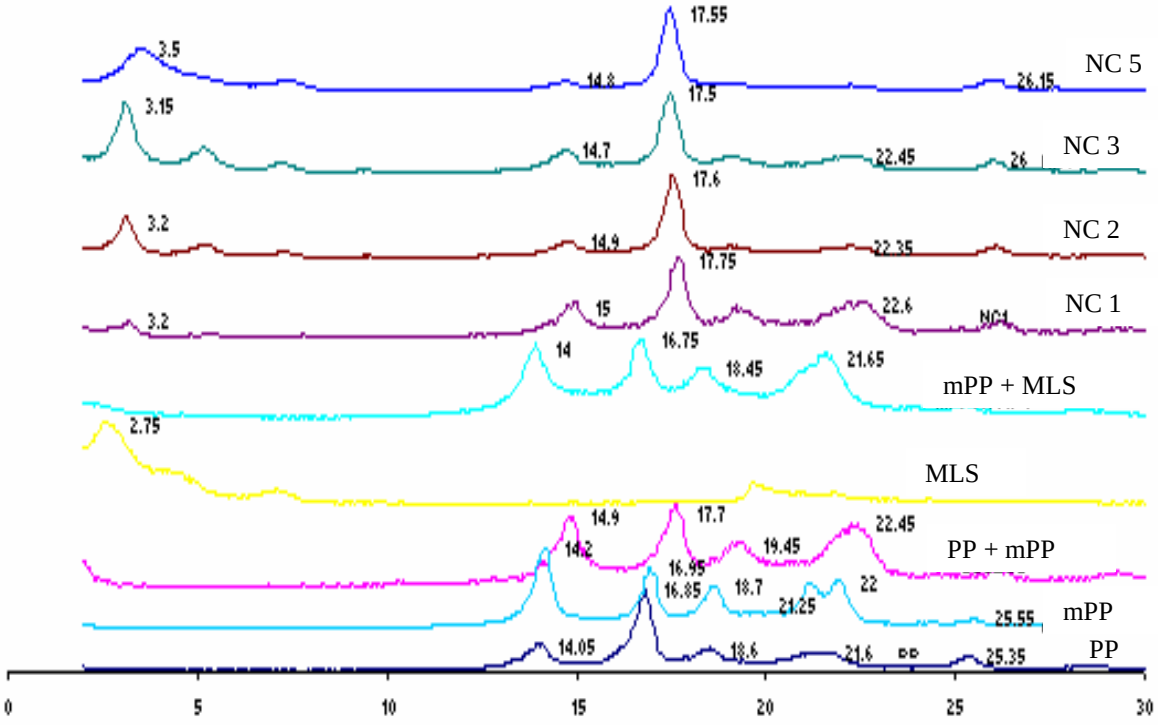

Figure 3.1. Surface X-ray spectra of the specimens

The absence of exfoliation at the surface is highlighted by the presence of the reflections of the 001 peak at 2 θ = 4.5° and 7.1 ^{o} in all the MLS containing samples. I also examine the influence of MLS and mPP on the crystal structure of PP. This is complicated since the monoclinic α phase of PP is most predominant in nucleated PP, but has an epitixial relationship to the γ phase of PP such that each can grow on the lamella of the other [19]. A demarcation between the α and γ phase is made by comparing peak intensities at 2θ =14^{o} to 2θ =17^{o}. The 14^{o} peak is seen to be sum of the α peak at 14.08 ^{o} and the γ peak at 13.84 ^{o} while the peak of 17° is the sum of the α peak at 16.95 and the γ

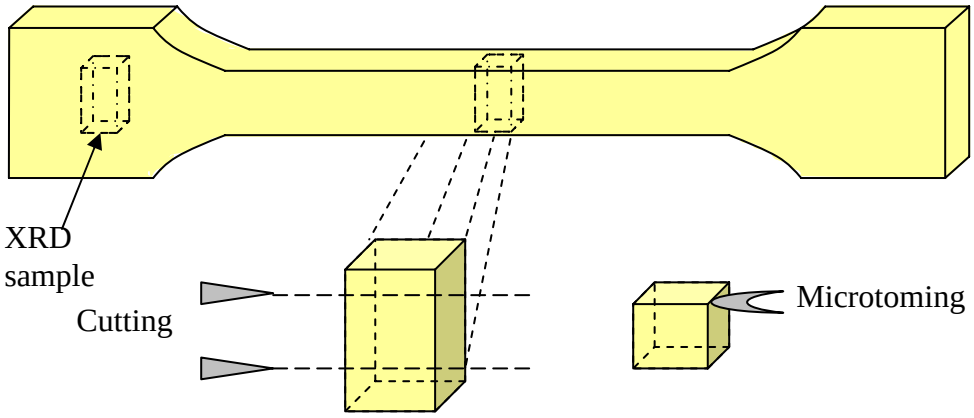

Figure 3.2. Location of microtoming for the TEM analysis

peak at 16.72°. When the latter peak is higher it implies a dominance of the γ phase [34, 35].

Table 3.2. Retention of small diffraction angle on the samples tested

Material	**FWHM**
PP	No peak
mPP	No peak
PP + mPP	0.349
MPP + MLS	No Peak
NC 1	0.632
NC 2	0.430
NC 3	0.470
NC 5	0.776

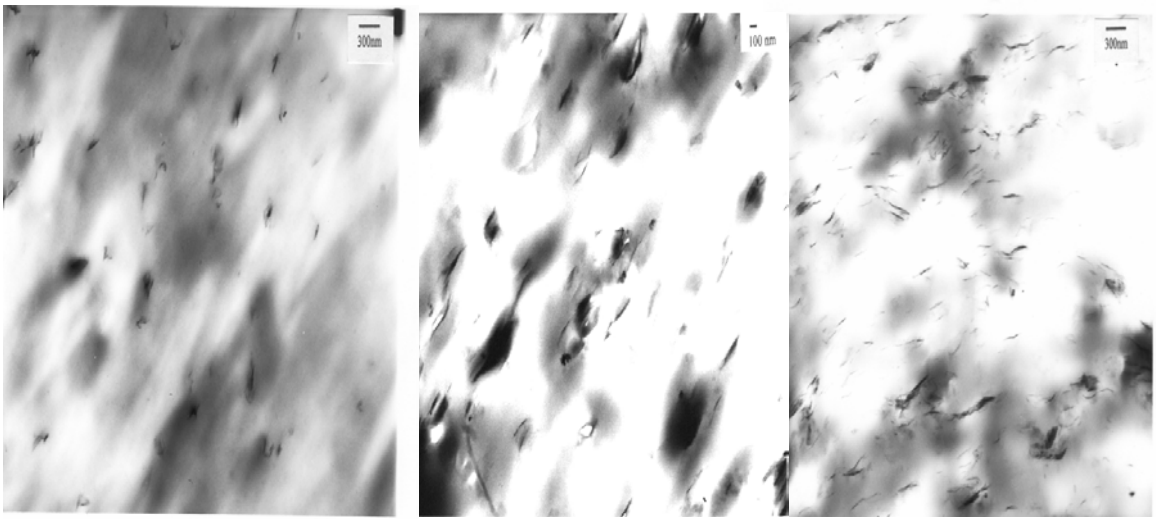

(a) (b) (c)

Figure 3.3. TEM for (a) NC 1, (b) NC 3, and (c) NC 5 nanocomposites.

Examining the peaks of the PP sample a γ phase dominance is seen in the higher intensity of the 17^{o} peak relative to the 14^{o} peak. mPP however shows a α phase dominance. When PP and 2%mPP are blended together, the α phase dominance of the mPP was retained. The same situation occurs when 1% MLS was added to the mPP sample. Thus the dominance of mPP crystallization was evident in the mPP + PP and mPP + MLS combinations. Adding MLS to the PP + mPP blend however returns the system to a γ phase dominance for all the nanocomposites.

3.4.2. TEM analysis

Once the preliminary results suggested a characteristic intercalated structure, it was necessary to determine the degree of exfoliation and the distances between each particle. Figure 3.2 shows the location where the samples for microtoming were taken.

TEM images of nanocomposites with MLS concentration of 1, 3, and 5% are shown in figure 3.3. The images shown that it is possible to observe the dispersion showing complete exfoliation, since the MLS particles do not show any order, and are completely dispersed in the matrix. Figure 3.4 shows the separation between platelets, indicating enough separation to be considered a highly exfoliated structure.

The TEM analysis of the specimens seemed to be inconsistent with the X-ray diffraction results. One significant difference was that the X-ray analysis was done

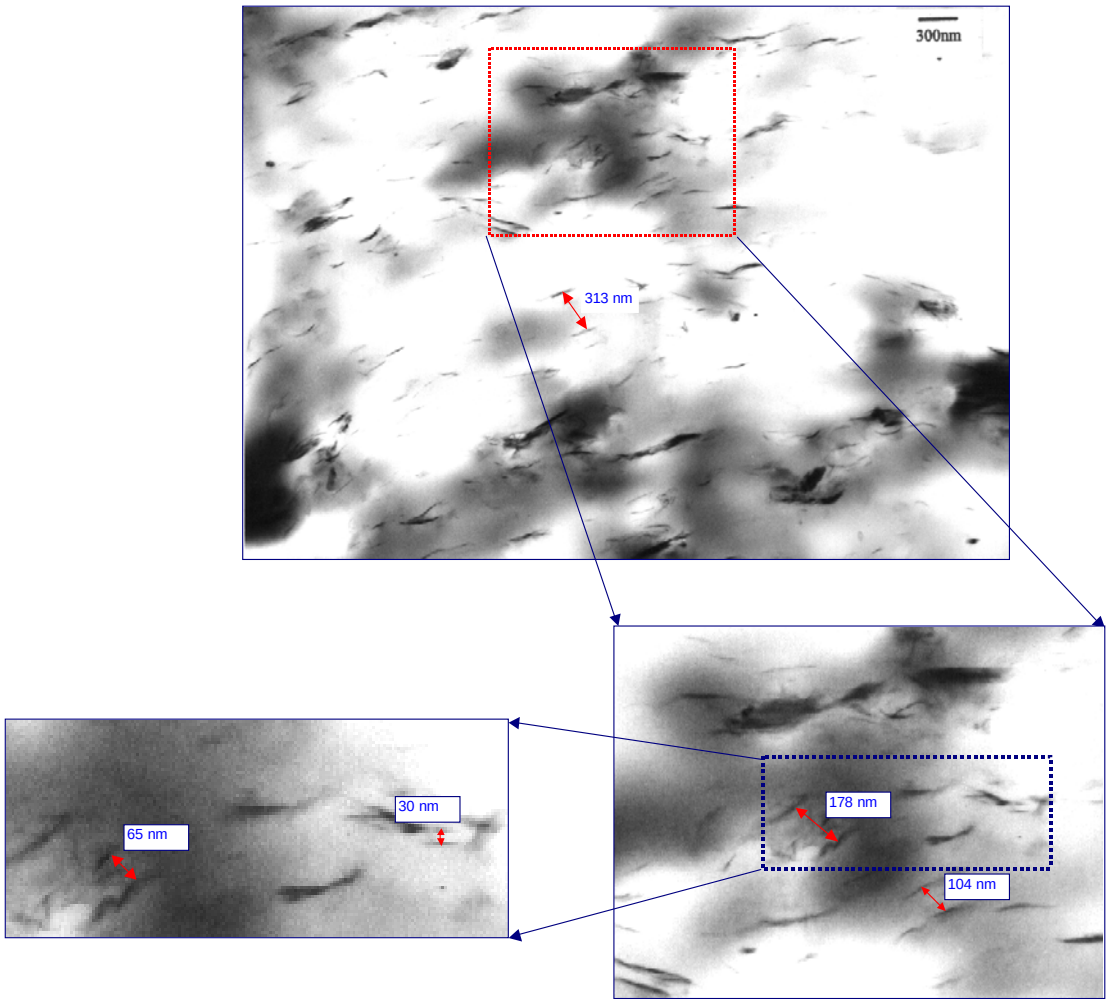

Figure 3.4 Spacing among platelets in NC 5 specimen

across the cross section of the surface, while the TEM samples were taken from the bulk of the specimens. Further analysis was therefore conducted after removing the surface layers of the sample.

3.4.3. Bulk X-ray analysis

In order to analyze the bulk of our specimens, I polished the surface of the sample and performed a new XRD analysis (Figure 3.5). The X-ray spectra indicated that all nanocomposites had no peak corresponding to the 001 interlayer basal spacing of the MLS, indicating an exfoliated structure.

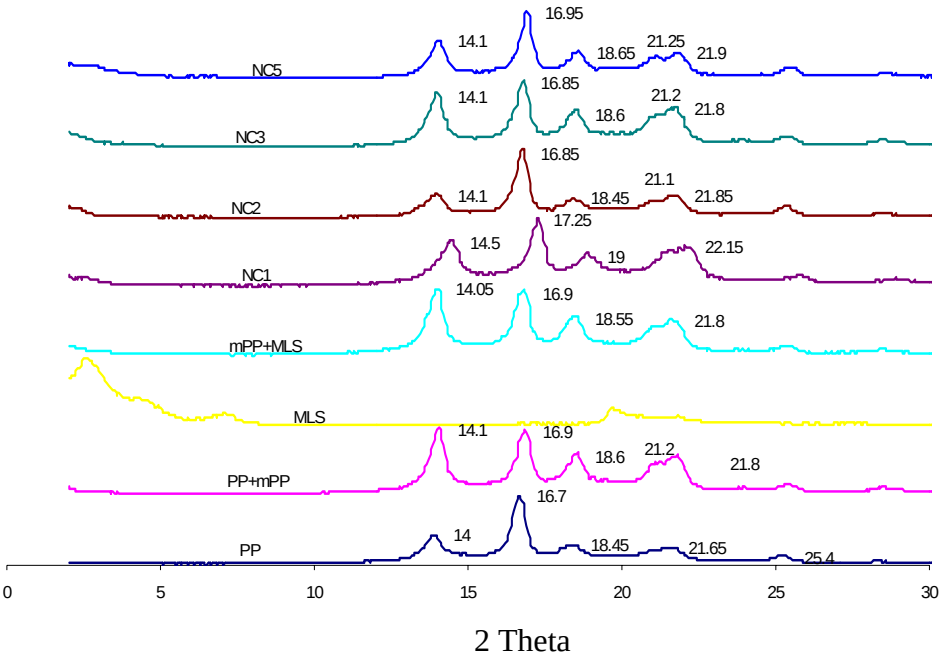

Figure 3.5. Bulk X-ray diffraction pattern of systems investigated

Table 3.3. Intensity ratio for the surface and inner portions of the specimens for peaks at 2θvalues of 16° to 14 °

$I_{16°}/I_{14°}$		
	Surface	**Inner**
PP	3.80	2.26
mPP	0.67	0.67
PP + mPP	1.08	0.95
mPP + MLS	0.96	0.99
NC 1	2.28	1.47
NC 2	4.79	2.72
NC 3	3.31	1.21
NC 5	7.64	1.72

XRD indicated that the mPP bulk spectrum also retains the α dominance exhibited by the surface. The combined mPP + PP bulk spectrum shows a γ phase dominance of the PP phase and also a shift to higher 2θ. This indicates a phase transformation in PP induced by mPP in going from the surface to the core of the sample. The transformation is accompanied by a drop in crystal size, also observable by comparing the average FWHM for the five peaks between 2θ values between 14° and 25° degrees.

The nanocomposite samples show that for all samples an increased α phase growth onto the γ phase characterized by a decreasing intensity ratio of the 17^o to 14^o peak indicating differences in crystalline structure at the core and the surface. There is no discernable change in phase with increasing MLS concentration.

I note the retention of the crystalline phase as being a γ phase in contrast to research in nylon indicating that the presence of MLS results in transformation of the original α phase of nylon to a γ phase [19]. Thus the presence of MLS does not appear to introduce a compression effect inducing a phase change on the trapped PP materials. I attribute this to the high level of exfoliation depicted in the TEM pictures leading to low levels of intercalated structures in the bulk. This skin-core effect could be originated in the conditions in which the samples were processed. Figure 3.6 shows the direction of flow in the mold.

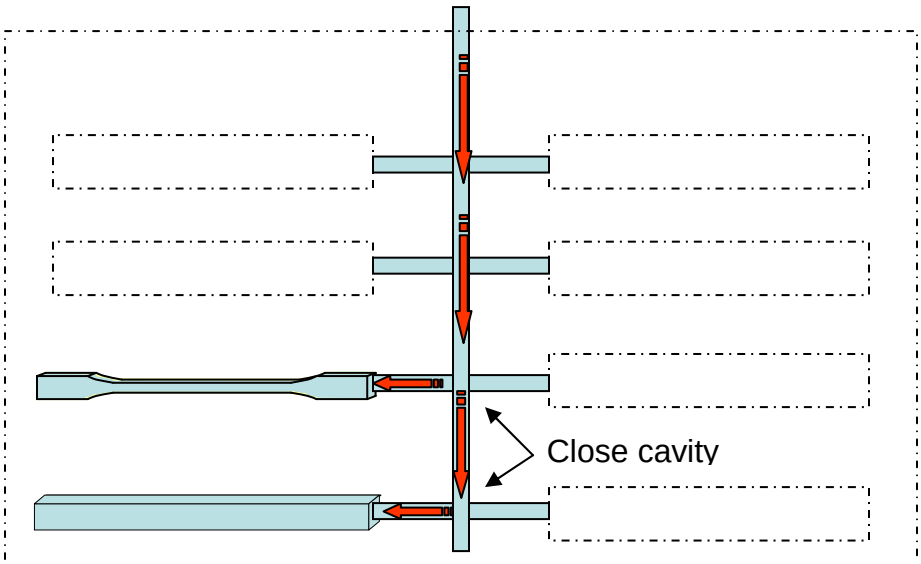

Figure 3.6. Injection flow inside mold

It is further probed the skin-core effect by conducting DSC analysis, showing noticeable differences among surface and core sections of the specimens.

The results for the skin and core are shown in Figure 3.8 and tabulated in Table 3.4.

Table 3.4. Calorimetric results on the surface and interior of the specimens tested

Inner						
	H 1st heat	**H 2nd heat**	**H cooling**	**T Peak Heat1**	**T Peak Heatl2**	**T Peak cooling**
PP	78.068	83.743	-99.621	160.366	158.033	116.3
mPP	60.271	59.871	-79.528	165.556	164.903	113.307
mPP+MLS	78.646	99.837	-94.215	162.366	156.7	114.3
mPP+PP	72.157	75.596	-100.012	162.7	159.7	115.966
NC1	39.575	36.983	-59.836	164.033	160.7	115.633
NC2	52.954	64.944	-87.139	163.366	160.366	113.633
NC3	61.303	57.364	-90.518	163.366	158.033	115.3
NC5	89.327	78.067	-104.888	162.033	159.033	112.966
Surface						
	H 1st heat	**H 2nd heat**	**H cooling**	**T Peak Heat1**	**T Peak Heatl2**	**T Peak cooling**
PP	71.603	74.106	-92.071	163.7	159.366	114.966
mPP	60.271	59.871	-79.528	165.556	164.903	113.307
mPP+MLS	63	57.074	-84.665	162.366	158.033	114.633
mPP+PP	71.425	65.65	-88.26	165.033	159.7	114.3
NC1	71.91	78.502	-96.182	164.033	159.366	116.3
NC2	58.122	53.671	-74.16	164.033	159.7	115.3
NC3	69.621	63.51	-94.546	165.033	160.033	114.966
NC5	58.325	61.906	-91.801	165.366	161.366	114.966

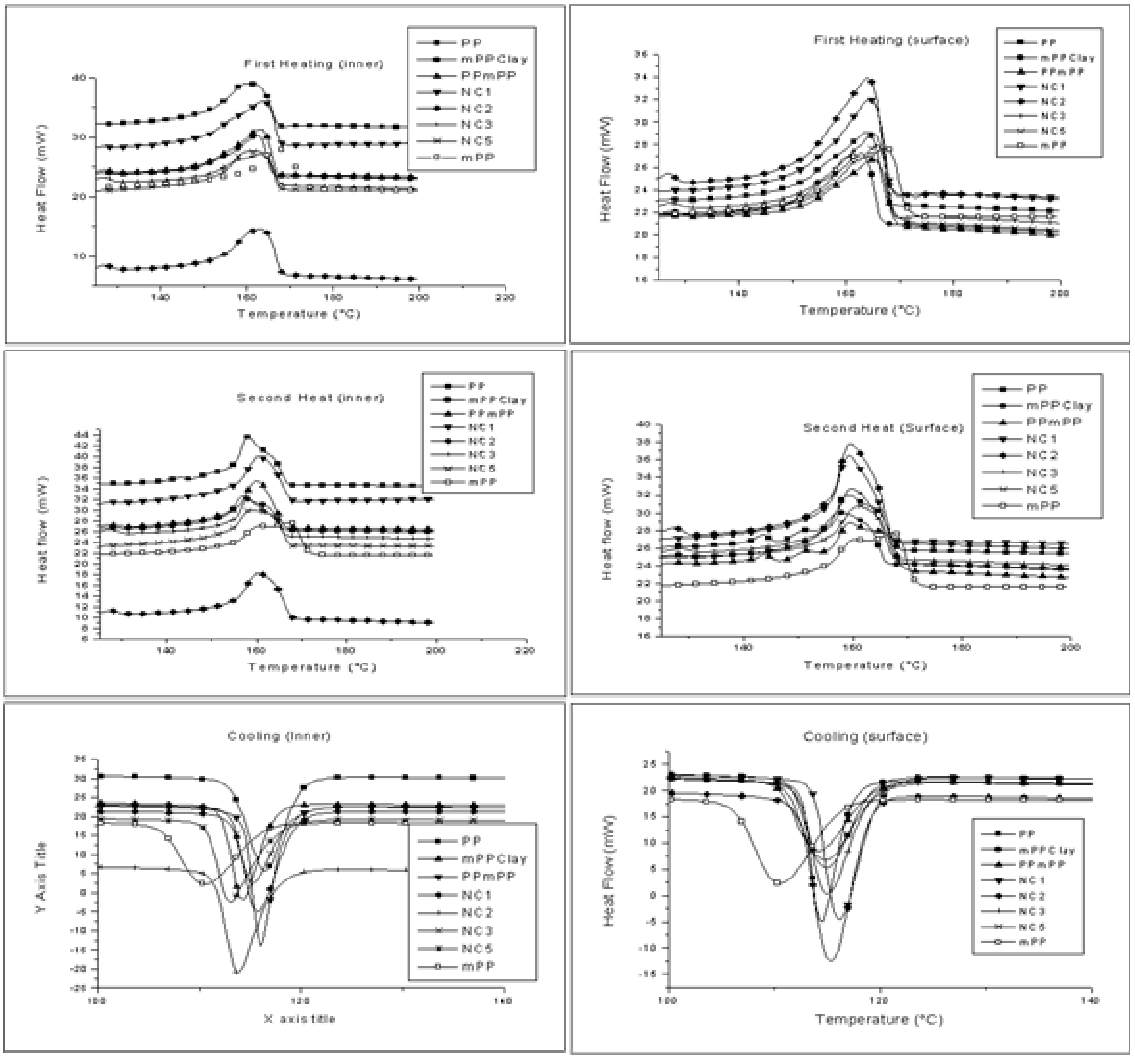

Figure 3.7. DSC plots of surface and bulk samples

As can be seen, for PP, there is no discernable difference between the surface and bulk enthalpy of melting. However all nanocomposites show a sharp drop in the enthalpy of melting in the bulk compared to the surface. Further, as the DSC scans indicate, a slight increase in melting temperature takes place, but it is accompanied by decreased area under the curve with increasing MLS content. This is indicative of decreased overall crystallization, but an increased rate of crystallization as MLS is introduced into the PP + mPP blend. Prior research on PP + mPP shows that the interaction between the systems

can be represented as an attraction between the PP homopolymer and the PP moiety of the copolymer, and repulsion between PP and the maleic anhydride. Depending on the level of maleation, two morphologies can result: a co-crystallized system represented by a single melting peak at low temperature, or a phase separated crystallite characterized by two melting peaks, especially as the scanning rate is decreased. As can be seen from examination of the first and second heating scans, the introduction of mPP into the PP results in a phase separated PP.

The melting temperature along all the samples increases over that of PP, and there is a slight increase in fusion temperatures indicative of changes in crystalline dimensions to smaller crystallites (also supported by increased 2θ values in x-ray peaks) but a higher degree of crystallinity. However, the introduction of MLS results in a single melting peak whose enthalpy varies with concentration. The insertion of 1% MLS by weight into the mPP+PP serves to decrease the melting point and increase the crystallization fusion point, indicative of typical nucleation and growth kinetics due to introduction of additional heterogeneities, in the form of MLS platelets. The nanocomposites containing 2, 3 and 5% MLS by weight are characterized by similar melting peaks and enthalpies of melting but fusion peaks show that the NC 2 and NC 3 nanocomposites have decreased fusion temperatures indicative of distinct nucleation and growth kinetics. In NC 5 the fusion temperature is the same as NC 1, with a substantial decrease in peak area. Examining the trends, I hypothesize that there are two competing mechanisms: the crystallization kinetics increased the nucleation effects of more MLS sites, but then it also limits their growth due to the competing size of the crystallites to that of the MLS.

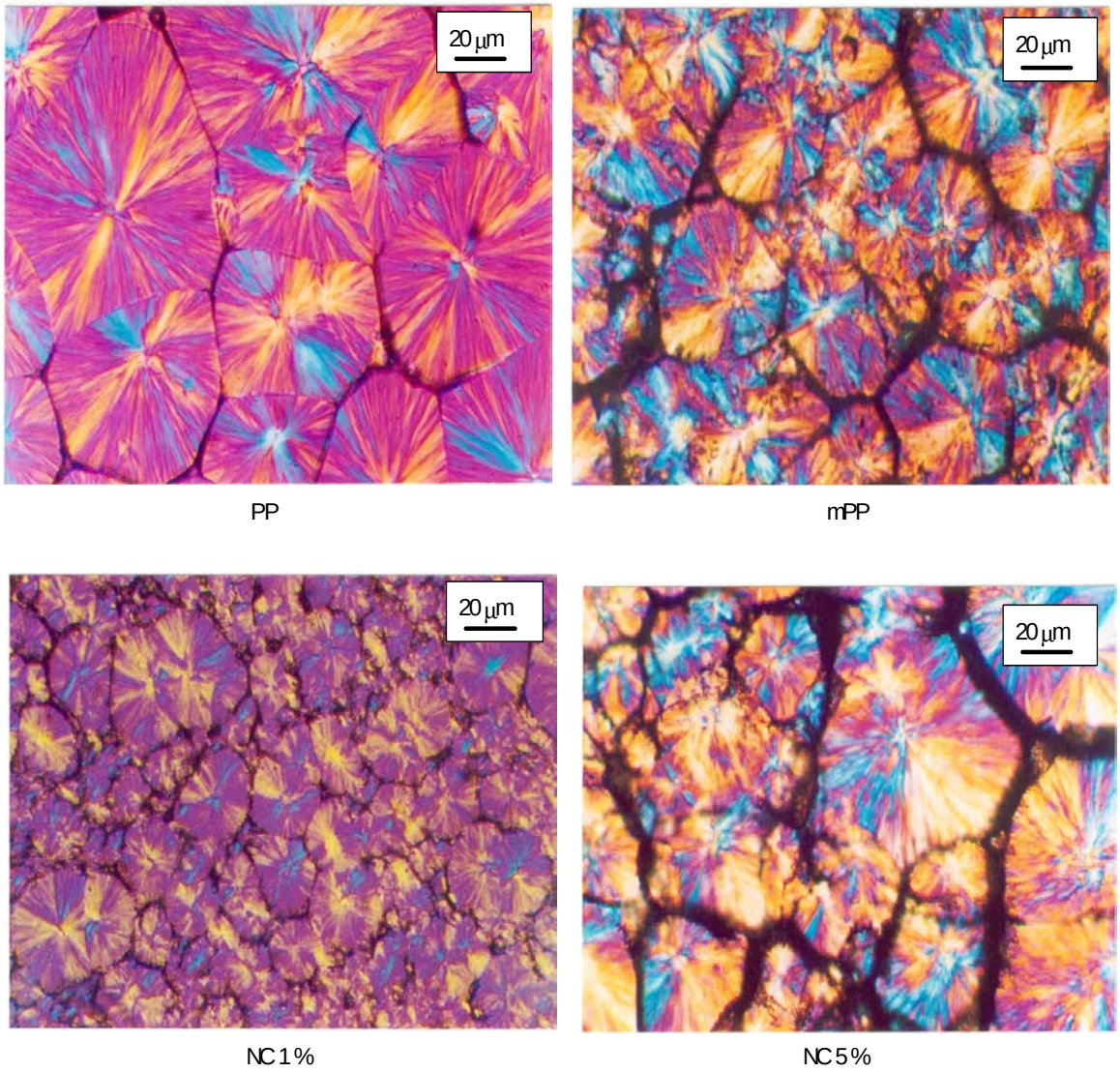

Figure 3.8. Optical micrographs of PP and the nanocomposites showing the influence of mPP and MLS on spherulites sizes

Examining the optical micrographs in Figure 3.8 I can see that the introduction of mPP into PP results in smaller crystallites. For NC 1, the crystallite sizes decrease, supporting our earlier DSC inference of increased nucleation. In the case of NC 3, a larger crystallite is formed, supporting the decreased fusion temperatures from the DSC.

However for NC 5 a bimodal distribution in spherulitic size is formed with some crystallites having a dimension close to that of the PP + mPP and others larger as in the case of polypropylene. The fact that the polypropylene used is self-nucleated polypropylene helped to this bimodal distribution and growing. Difficult to capture in images, the self-nucleated polypropylene interacts with the MLS affecting the crystallization mechanisms. The presence of the MLS increases the nucleation sites present in the matrix leading to a higher number of spherulites. The presence of mPP and clay also influences the final size and aspect ratio of the spherulites.

3.5. Summary of results on the dispersion and crystallization effects of PP nanocomposites

The X-ray results have shown the dual effect that the addition of MLS produces in the PP. First, the MLS tends to emigrate to the surface of the specimens, pulled by the maleic anhydride. This could be thought as an effect contrary to what is desired. However, the viscosity of the systems does not allow the complete emigration of the fillers. As consequence of this emigration effect and being the MLS and mPP bond to each other, the MLS is better exfoliated in the matrix, pulled by the mPP in its way to the surface. The X-ray spectra for the bulk shows complete exfoliation since all the low reflection peaks disappear. Another effect observed, is the change in the crystallization of PP phases.

The MLS at the surface influences the transition from a monoclinic α phase to a triclinic γ phase. However, the bulk of the matrix retains the monoclinic phase. Being a

triclinic structure, a crystalline state with lower symmetry, will represent a more complicated path for deformation to occur. This will lead to a more reinforced structure.

The TEM images show the distribution of the MLS in the matrix and the interlayer spacing. From the data, it is possible to observe the manner in which the distance between platelets and their relative orientation are characteristic of an exfoliated structure. Changes in NC 3 to NC 5 imply that NC 3 specimen is a partially exfoliated structure, however, the X-ray analysis shows that they actually are exfoliated. This could be related to the MLS content in each specimen. In TEM images of NC 1, the image shows a lower density of reinforcement. Also the compatibilizer content is kept constant in all the samples, then the interaction between MLS and mPP will be easier and more proper in the NC 5 content than n the NC 1 since there is more clay that can be dispersed and even when similar content of clay would immigrate to the surface pulled by the mPP, the core would show a higher exfoliation yielding in a better reinforcement.

The microstructure of the PP is observed in the optical micrographs. Here, the changes the matrix experiences are critical. The original PP shows a characteristic spherulite size. The addition of mPP decreases slightly the spherulite size, but induces a thick grain boundary, which could lead to lower ductility in the specimens. However, low MLS content limits the growth of the spherulites, but promotes nucleation. This could be of some benefit, since the matrix will increase its stiffness, but as soon as a crack is formed it will find almost no inhibition to propagation. Increasing the content of MLS produces a combined effect. The mixture of big and small spherulites, will represent a better reinforcement, since the combined action of strength and small size will distribute the applied stresses, and since it is not a directional effect, it could happen in

both axes. The difference in nucleation can be explained as follows. The addition of mPP will cause a decrease in the spherulite size. The addition of MLS promotes the nucleation and growth of these spherulites, but since the MLS content is lower than the mPP content, the mPP dominates the nucleation and growth, leading to the structure I see.

The resulting structure and the fact that a bimodal nucleation is involved in the nanocomposite, could help to explain the changes in the semi-crystalline structure of polypropylene. As explained an alpha and gamma phases are characteristics of different arrangement of polypropylene. If self-nucleated PP starts as a gamma phase, then the presence of MLS and mPP in its structure is leading to a change to an alpha phase, originating the distribution of MLS in the PP matrix. The retention of the gamma phase is observed in the X-ray spectra mentioned above, and it is also demonstrated for the mechanical behavior of the individual specimens, as will be illustrated ahead.

In conclusion, I can say that the performance of the PP nanocomposite is critically affected by the MLS concentration and mPP effects on the crystal formation. A unique skin-core variation of dispersion was obtained implying that flow direction is a variable in nanocomposite processing.

References

1. Wang Z, Pinavaia TJ. Chem Mater 1998; 10: 1820-1826.
2. Wang MS and Pinnavaia TJ, Chem. Mater. 6. 1994. 468-474.
3. Lan T, Kaviratna PD and Pinnavaia TJ, Jour Phys Chem Solids 1996; 57(6):

1005-1010.

4. Kaviratna PD, Pinnavaia TJ, Schroeder PA. Jour Phys Chem Solids 1996; 57(12): 1897-1906
5. Messersmith PB, Giannelis EP. Jour Polymer Sci 1995; 33: 1047.
6. Lan T, Pinnavaia TJ. Chem Mater 1994; 6: 2216-2219.
7. Wang Z, Pinnavaia TJ. Chem Mater 1998; 10: 3769-3771.
8. Lan T, Kaviratna PD, Pinnavaia TJ. Chem Mater 1994; 6: 573-575.
9. Lan T, Kaviratna PD and Pinnavaia TJ, Chem. Mater. 7. 1995. 2144
10. Giannelis EP, Jour Minerals 1992; 44: 28.
11. Messersmith PB, Giannelis EP. Chem. Mater 1994; 6: 1719-1725.
12. Dagani R. Chem Engin news 1999; Sept 21st: 70-77.
13. Miller B. Plastics Formulating & Compounding 1997; May/June: 30.
14. Sherman LM. Plastics Technology 1999; June: 52
15. Shen Z. Nanocomposites of Polymers and Layered Silicates, Ph.D. Thesis Oct 2000; Monash University, Australia.
16. Kornmann X, Lindberg H, Berglund LA. Polymer 2001; 42: 1303-1310.
17. Burnside SD, Wang HC, Giannelis EP. Chem Mater 1999; 11: 1055-1060.
18. Giannelis EP. Chem Mater 1990; 2: 627-629.
19. Lotz B, Graff S, Wittman JC. Jour Polym Sci Polym Phys Ed. 1986, 24 2017.
20. Kojima Y, Fukumori K, Usuki A, Okada A, Kurauchi TJ. Mater Sci Letters 1993; 12: 889-892.
21. Kojima Y, Usuki A, Kawasumi M, Okada A, Fukushima Y, Kurauchi T, Kamigaito O. Jour Mater Res 1993; 8: 1185-1189.

22. Kurokawa Y, Yasuda H, Kashiwagi M and Oyo A, J. Mater. Sci. Letters 16. 1997. 1670-1673.

23. Yano K, Usuki A, Okada A, Kurauchi T, Kamigaito O. Jour Polymer Sci 1993; 31: 2493.

24. Usuki A, Kojima Y, Kawasumi M, Okada A, Fukushima Y, Kurauchi T, Kamigaito O. Jour Mater Res 1993; 8: 1179-1184.

25. Usuki A, Kojima Y, Kawasumi M, Okada A, Fukushima Y, Kurauchi T, Kamigaito O. Jour Mater Res 1993; 8: 1174-1178.

26. Kojima Y, Usuki A, Kawasumi M, Okada A, Kurauchi T, Kamigaito O. Jour Polymer Sci 1993; 31: 983.

27. Kojima Y, Usuki A, Kawasumi M, Okada A, Kurauchi O, Kamigaito O Kaji K. Jour Polymer Sci 1994; 32: 625.

28. Kojima Y, Matsuoka T, Iakahashi H, Kurauchi TJ. Applied Polymer Sci 1994; 51: 683.

29. Tan KH. Principles of soil chemistry. New York. Marcel and Dekker 1998.

30. Pinnaaia TJ, Beall GW. Polymer-clay nanocomposites. New York. John Wiley and Sons 2001 (chapter 8)

31. Own CS, Seader D, D'Souza NA, Brostow W. Polymer Composites 1998; 19: 107-115

32. Liu X, Wu Q. Polymer 2001. 42: 10013-10019.

33. Nam PH, Maiti P, Okamoto M, Kotaka T, Hasegawa N, Usuki A. Polymer 2001; 42: 9633-9640.

34. Foresta T, Piccarolo S, Goldbeck-Wood G. Polymer 2001; 42: 1167-1176.

CHAPTER 4

QUASI-STATIC MECHANICAL PERFORMANCE OF POLYPROPYLENE NANOCOMPOSITES

4.1 Introduction

In chapter III a unique skin-core dispersion was determined in PP nanocomposites. A strong MLS concentration dependence on spherulite size was established. Here the tensile and fracture properties of the nanocomposites are investigated.

The combination of all the morphological effects observed in the previous chapter will result in a reinforced structure with optimal properties. The combined structure of PP added to the size distribution of the spherulites will provide a better performance. These two characteristics could not be as important in an intercalated structure since this will mean that the structures would be localized and not distributed in the system. An exfoliated structure will help to distribute these effects on the matrix.

The recent growth in interest in the use of MLS in different polymer systems leads to the need to evaluate their properties and determine the limits of their use. The reason for this interest has been the ability of the MLS to improve the mechanical properties as well as the rheological properties, when added at low percentages (below 10% weight percent) [1, 2]. Properties of interest include Young's modulus, maximum yield strength, ultimate tensile strength, fracture toughness and creep. From a materials deformation stand-point, a rare effect is introduced through comparison of tensile and creep measurements. The later is covered in chapter V. Within the context of low rate deformation, the influence of a crack is investigated here.

The deformation of materials as consequence of the strain rate applied are evaluated by two main approaches, the strength of materials approach and the fracture mechanics approach.

In the fracture behavior of materials, LEFM is the most common method for evaluation, but if non-linear deformation is present in the material it is not valid [3]. In polymeric composites, the presence of non-linear deformation makes it essential to consider the plastic contribution to failure. Among the techniques for measuring failure, CTOD and J-integral, are reliable methods applicable to different materials and techniques. [3-7]. CTOD and J-integral are techniques that relate both of the previous fracture analysis results. This is because in their calculation, the fracture toughness of the material is considered. The area under the force-displacement plot is considered in the calculation of the plastic component of the energy. However, the value of crack opening can be obtained from TWI images and is a measure of the plasticity of the system, the higher the value, the more plastic contribution is provided.

4.2 The strength of materials approach

Mechanical properties are almost always material dependent and it is not convenient to obtain them from a single test. Depending on the final application of a part, different properties need to be developed and measured. Two of the most common techniques to measure the properties mentioned above are: uniaxial and flexural testing. Uniaxial testing consists of the application of unidirectional stress on a standard specimen. The specimen is held by two grips and then stretched until the specimen

ruptures. This test can be used to determine important values such as Young's modulus and ultimate tensile strength and some other properties.

The flexural test, as it names indicates, has been created mainly to measure the flexural properties of materials, but this test can be used to analyze the fracture toughness too. The configuration consists of a specimen supported on a fixture with two points close to the edges of the specimen, and a single point of application of the load at the center of the specimen, normally right above a notch or precracked point.

4.3 Fracture mechanics approach

Fracture mechanics was recently developed as an experimental technique to evaluate the mechanical performance in the middle of the twenty century as a need to have a method for the analysis of the resistance of the material before and at failure [3].

In the case of fracture mechanics, not only the applied stresses and the nominal maximum stress of the material are considered. Fracture mechanics differentiates itself from the strength of materials approach since it accounts for flaws in the material and the ability of material to stop or dissipate the growth of these flaws due to the applied stress. In relating the three parameters of applied stress, flaw size and fracture toughness, two criteria can be considered, the energy criterion and the stress intensity approach. The energy criterion considers the point where there is enough energy for the crack to propagate while the stress intensity approach is founded on the concept of a stress intensity factor which explains how the stresses have a different effect related to the geometry of the part. Both of them, to some extent can be considered equivalent.

Due to the diversity of materials and the stages of failure they may cross, more analytical classifications are done to evaluate the mechanics of failure of a material. Among them I can mention two of the main theories that describe the mechanics of failure of a material, LEFM and EPFM.

The main differences between them are in the interpretation of the mechanical failure. LEFM considers only the proportionality region where the strain variation is linear in relation with the stress. This approach is valid as long as the relations in the specimen analyzed are kept linear, but if an additional factor, such as time dependent properties, would apply to the material under analysis, the study would be incomplete. For this latter case, a better understanding of the mechanics of failure will be given by the EPFM, where all the structural contributions are taken into account, either linear or non linear. Figure 4.1 describes this concept.

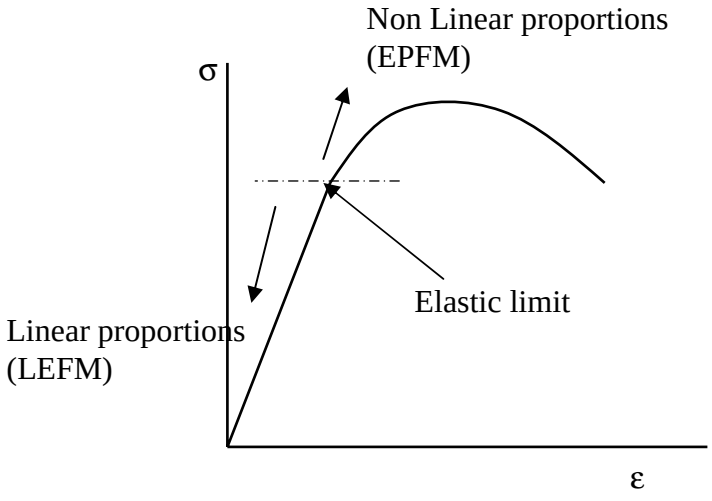

Figure 4.1 Interpretation of linear and non linear interactions

In the case of LEFM, where no plastic contribution is considered at all, a brittle failure of the material is assumed. This is not accurate for most materials. Further analyses in the EPFM theory have been focused on explaining how the plastic contribution defines the final performance in most cases. Depending on the mode of failure the material will show a different profile of stress or strain concentration around the crack propagation path as shown in figure 4.2 where different zones and contributions are sketched. In figure 4.2, the different stages that can be observed during failure of materials are identified. In the case of a ductile failure, only the first stage will be noticeable, since in such failure the crack will find resistance to propagate. As the plastic contribution increases, the different zones will be present in the region around the crack path [3].

There are several theories [3, 11-15] that explain the mechanics involved in failure and different reactions of the material. Fracture toughness is probably one of the

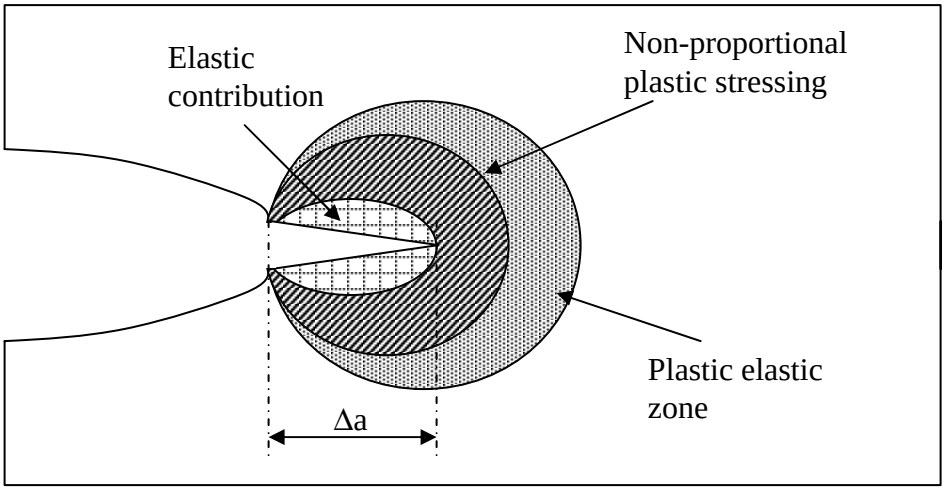

Figure 4.2 Different zones identified while a materials failure.

most important concepts. Even when it does not describe completely the fracture phenomena, it measures the resistance to the crack propagation, which is a significant parameter to consider. Some of the theories developed to understand this concept, are the CTOD theory and the J integral, both of them are derived from the fundaments of EPFM [3].

4.3.1. Crack tip opening displacement

The CTOD was first established by Wells. He discovered that the degree of crack blunting increased in proportion to the toughness of the material. He proposed the opening at the crack tip as a measure of the fracture toughness [3]. The CTOD is defined as

$$\delta = \frac{4}{\pi}\frac{K_I^2}{\sigma_{YS}E} \tag{4.1}$$

where δ is the CTOD, K_I is the stress intensity factor, σ_{YS} is the yield strength and E is the elastic modulus. The strip yield model proposes a similar approximation for the CTOD as:

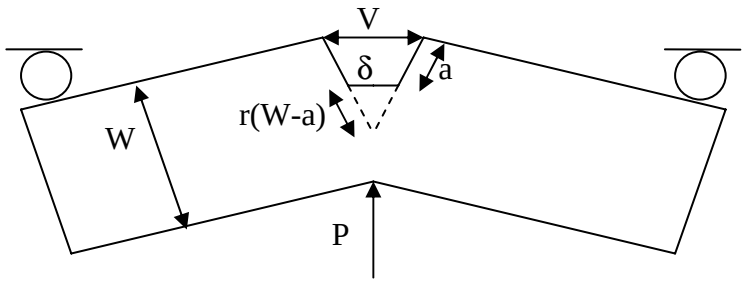

Figure 4.3. Schematic showing the parameters required for CTOD calculation [13].

$$\delta = \frac{K_I^2}{m\sigma_{YS}E} \tag{4.2}$$

where m, is a dimensionless constant that is approximately 1.0 for plane stress and 2.0 for plane strain. The displacement, V, at the crack mouth is measured and the CTOD is calculated by assuming the specimen halves are rigid and rotate about a hinge point. However, this procedure is inappropriate when displacements are primarily elastic. Consequently, modifications to the hinge method have been made to consider plastic and elastic contributions and the CTOD is defined by (4.3):

$$\delta = \delta_{el} + \delta_p = \frac{K_I^2}{m\sigma_{YS}E} + \frac{r_p(W-a)V_p}{r_p(W-a)+a} \tag{4.3}$$

where “el” and ”p” denote elastic and plastic components respectively. r_p is the plastic rotational factor and varies from 0 to 1. W and "a" are the width and the crack length on the sample and V_p is the crack opening at the moment of failure [3].

4.3.2. J –integral

The J-integral is a path-independent contour integral that describes the stresses, strains, and displacements of any path around a singular crack, if either linear or non-linear deformation proceeds crack growth. Physically, the J-integral can be considered as the difference of potential energy between two loaded identical specimens with slightly different crack lengths [4]:

$$J = -\frac{1}{B}\frac{dU}{da} \tag{4.4}$$

where U is the potential energy that can be obtained by measuring the area under the load displacement curve, a the crack length and B the thickness of the sample.

Elastic and plastic contributions have to be considered, and the J-integral is then defined by (3.4):

$$J = J_{el} + J_p = \frac{K_I^2}{E} + \frac{\eta_p U_p}{B(W-a)} \tag{4.5}$$

where η_p is a dimensionless constant. For a deeply cracked plate in pure bending, $\eta_p = 2$.

4.4. Experimental

4.4.1. Materials

PP, PP + mPP (polybond 3150) (mPP), and PP + polybond + MLS specimens were prepared.

Concentrations of 1, 2, 3, and 5 wt% (NC 1, NC 2, NC 3, and NC 5, respectively) of MLS were selected. mPP was used as a compatibilizer among the PP and the MLS. The MLS used was Cloisite® 15A. Table 4.1 shows the concentrations used in this research.

4.4.2. Tensile conditions

Tensile tests were done using MTS-810 Hydraulic system at room temperature, and with a displacement rate of 2 mm/ min.

Table 4.1 Compositions of samples used.

Material	**PP**	**PP + mPP**	**mPP + MLS**	**NC 1**	**NC 2**	**NC 3**	**NC 5**
HPP	100	98		97	96	95	93
Polybond 3150		2	99	2	2	2	2
Cloisite®			1	1	2	3	5

4.4.3. Fracture toughness test

The samples were obtained by injection molding and then cut to the final length. The original width and depth are used in the testing. Notching and precracking of the samples was done according to the ASTM standard 5045-99, using a diamond saw for the notch and a new razor blade for the precracking. The three point bending technique was used to test the samples using a MTS-810 Hydraulic system with a rate of 10 mm/min. The tests were monitored with an Infrared Thermal wave camera from FLIR systems, model Prism-DS. All of the tests where the thermal camera was used were done at room temperature. Additional test at -30 ° C were done to verify the degree of reinforcement at temperatures below the glass transition temperature.

4.5. Results

4.5.1. Tensile test

Figure 4.4 shows tensile stress-strain relationships for the materials investigated with the concentrations defined in table 4.1. As can be seen the yield strength for almost all nanocomposites are similar to that of PP, with a maximum value observed in the NC 5 nanocomposite. These values are tabulated in table 4.2.

Important differences can be observed from this analysis. Taking as a reference the behavior of PP, the matrix, I observe that the mPP + MLS specimen has a marked inferior behavior in the elongation properties, and is more brittle. The rest of the samples show plastic behavior to a varying degree. NC 1, NC 2, and NC 3 do not reach a level of elongation comparable to PP, and only NC 5 reaches a value close to it. However, two

samples did not fail following the same cycle, the specimen of PP + mPP and NC 5. A strain hardened necking of the gauge length was observed. Considering the first case, PP + mPP one can determine that this system is a very ductile material, showing a larger plastic deformation before failure .In the case of the sample with NC 5 of MLS the situation is different. The values of yield strength, elastic modulus, and elongation to failure increased considerably. Actually it can be observed that as the MLS content increases the elongation to failure is also increasing. In the rest of the immediate properties, the values are very similar, but small differences can be also noted as the MLS content increases.

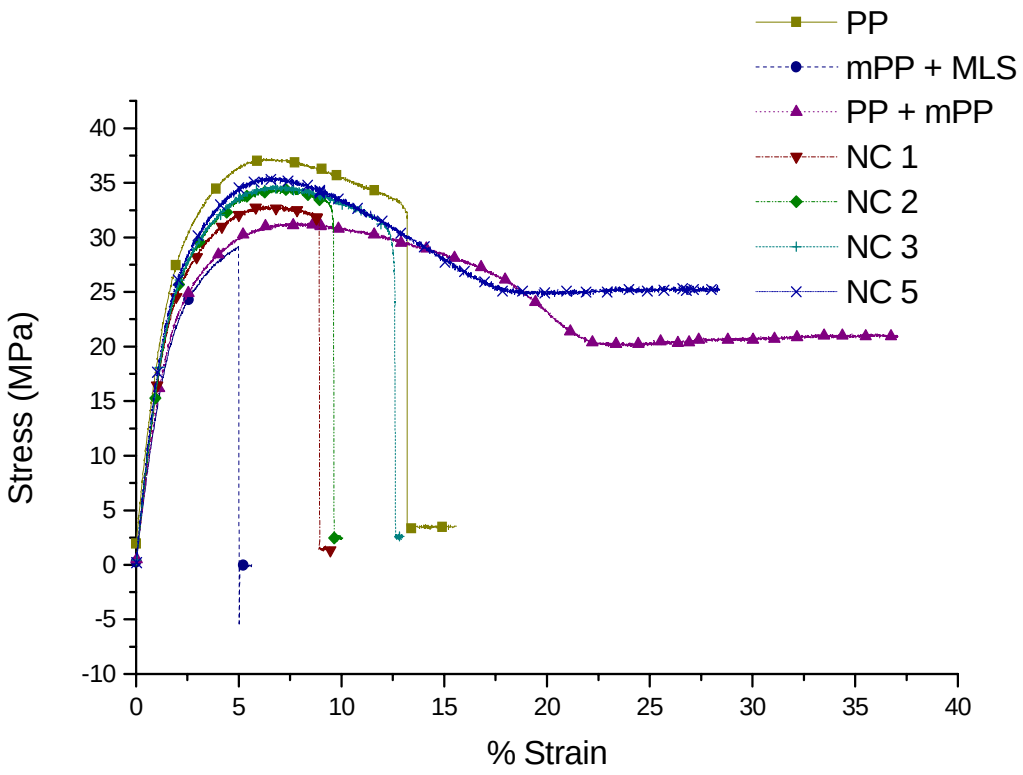

Tensile results

Table 4.2. Summary of the mechanical properties

Sample	E (GPa)	UTS (MPa)	Yield (MPa)
PP	1.90 ± .0266	37.24	19.93
mPP + MLS	1.49 ± .0313	29.16	16.20
PP + mPP	1.61 ± .0306	31.41	18.49
NC 1	1.62 ± .0194	32.89	18.31
NC 2	1.82 ± 0.0200	34.55	18.43
NC 3	1.70 ± .0306	34.78	18.73
NC 5	1.84 ± .0166	35.63	19.91

The simultaneous increase in both elastic properties and ductility implies a change in base PP properties being influenced by the MLS and the mPP. This was resolved through polarized microscopy showed earlier in figure 3.8.

PP by itself has large spherulites along the entire surface, above 60 microns in average. When the mPP is added, this size slightly decreases and spherulites of different sizes can be observed at 40 microns. When MLS is added, the nucleation of spherulites increases, leading to smaller sizes, spherulites <20 microns can be observed. For NC 5 the nucleation of spherulites generates a distribution in the spherulitic size; both spherulites sizes as big as those found in PP and small as in NC 1 are observed. Intermediate concentrations, as in NC 2 and NC 3 show a similar effect but the spherulites sizes are not as large as in the PP specimen. The results in NC 5 seem to be the result of two effects:

- the presence of the PP + mPP crystalline structure, where the small crystallites facilitate plastic deformation

- The presence of another distribution of larger crystallites similar in dimension to

NC 3 nanocomposites providing increased stiffness.

4.5.2. Fracture results

Figure 4.5 show characteristic plots for each one of the systems obtained from three point bending testing. The results are summarized in table 4.3. First, from the load-deformation curves it can be seen that for pure PP the fracture mechanism is the most brittle of all the samples, and that the plastic zone is increasing as the concentration of MLS increases.

All the MLS containing specimens showed higher fracture toughness than PP, with a maximum obtained at NC 5 content, where it is possible to observe that the K_q

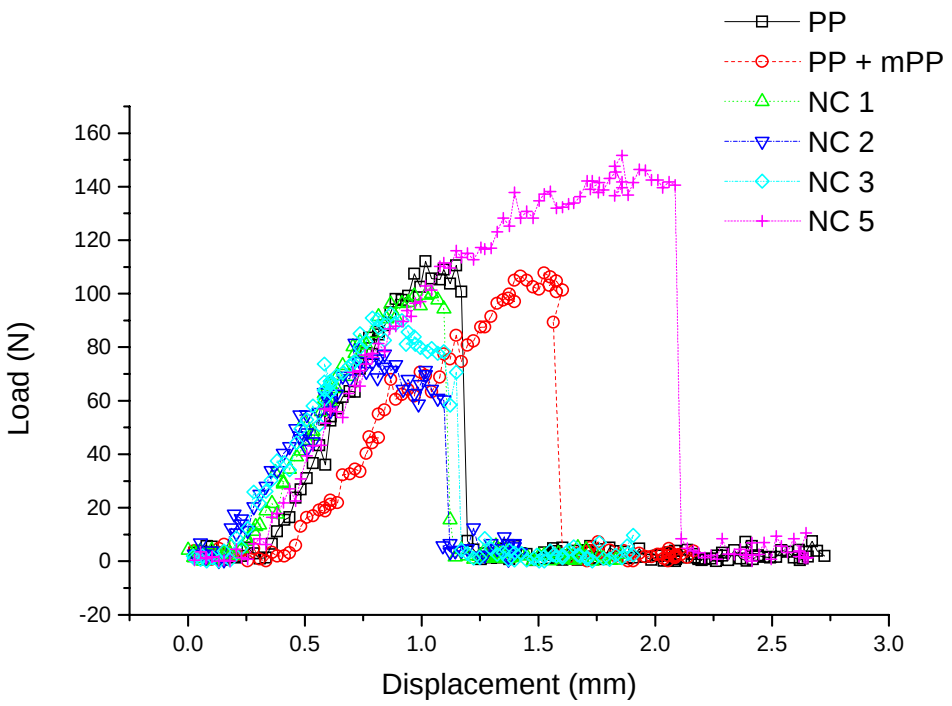

Figure 4.5. Characteristic three point bending plots

value is about 1.6 K_q of PP. This has a great impact since no similar results have been obtained before in the literature.(See table 2.1).

The last column in table 4.3 shows results obtained at -30°C. From these results, it is observed a similar trend to the one at room temperature. The larger values of K_q arise due to the higher load values to cause similar deflection as obtained at room temperature. This is significant from an application standpoint since automotive materials are specified to sustain stresses at temperatures as low as –30 °C.

Table 4.3. Fracture toughness at different temperatures.

MECHANICAL PROPERTIES SUMMARY				
Sample	**Kq (Mpa.√m)**	**S.D.**	**Kq (Mpa.√m) (T= -30°C)**	**S.D.**
PP	2.34	0.20	3.09	0.25
mPP + MLS	--		--	--
PP + mPP	2.3	0.11	3.31	0.16
NC 1 %	2.64	0.11	3.20	0.17
NC 2 %	2.53	0.18	3.22	0.29
NC 3 %	2.81	0.17	3.26	0.27
NC 5 %	3.76	0.08	3.87	0.04

4.5.2.1. CTOD

The value of δ was calculated using Eq. 4.3, and using a plastic rotational value of 0.44 [3]. In table 4.4 these values of δ are summarized. The PP materials had almost no opening during the test.

The crack opening is directly related to the ability of the crack to propagate through the material and fail. When MLS is added, the crack opening is inhibited for

similar values of load, requiring a higher energy to propagate. Even when the energy to propagate is finally reached, the material still withstands the crack propagation, which causes a higher crack tip opening at the end. This is the reason for the increasing values in table 4.4 for increasing MLS concentration. NC 5 shows an important increment in relation to the rest of the samples, in both the plastic and the elastic contribution. In general, for all the samples, the plastic contribution is almost one order of magnitude higher than the elastic contribution.

Table 4.4. Plastic and elastic contributions in CTOD

	CTOD				
	δ_{el}(m)	S.D. (%)	δ_{pl}(m)	S.D. (%)	δ (mm)
PP	3.92E-05	7	1.89E-04	12	0.23
PP + mPP	5.36E-05	11	3.87E-04	9	0.44
NC 1 %	6.13E-05	13	2.72E-04	6	0.33
NC 2%	4.88E-05	6	6.11E-04	12	0.66
NC 3%	6.47E-05	7	7.83E-04	4	0.85
NC 5%	1.08E-04	7	1.88E-03	8	1.99

4.5.2.2. J-integral

The second analysis applied to the data is the J- integral. This technique, widely used for fracture analysis, actually relates more clearly than CTOD to the fracture toughness of materials. From the J-integral values, summarized in table 4.5, it is possible to observe that the trend is the same as in the case of CTOD. The elastic zone contribution can be neglected since the plastic parameter is defining the value of our system. As observed before, the higher content of MLS provides the largest improvement.

Table 4.5. Results from the J-integral

	J-integral				
	Up Mpa*m	**S.D. (%)**	**Jel (J/m²)**	**Jpl (J/m²)**	**J (KJ/m²)**
PP	27.20743	14	0.002916	2186.572	2.186575
PP + mPP	26.12445	12	0.00337	2212.055	2.212059
NC 1%	35.10854	10	0.004031	3162.669	3.162673
NC 2%	47.31082	11	0.003375	5231.168	5.231171
NC 3%	70.03576	8	0.004498	7056.299	7.056304
NC 5%	306.2771	5	0.007691	30669.74	30.66975

Once the techniques have been evaluated, the ideas summarized above for each test by the different techniques, can be summarized in a single and general trend. The

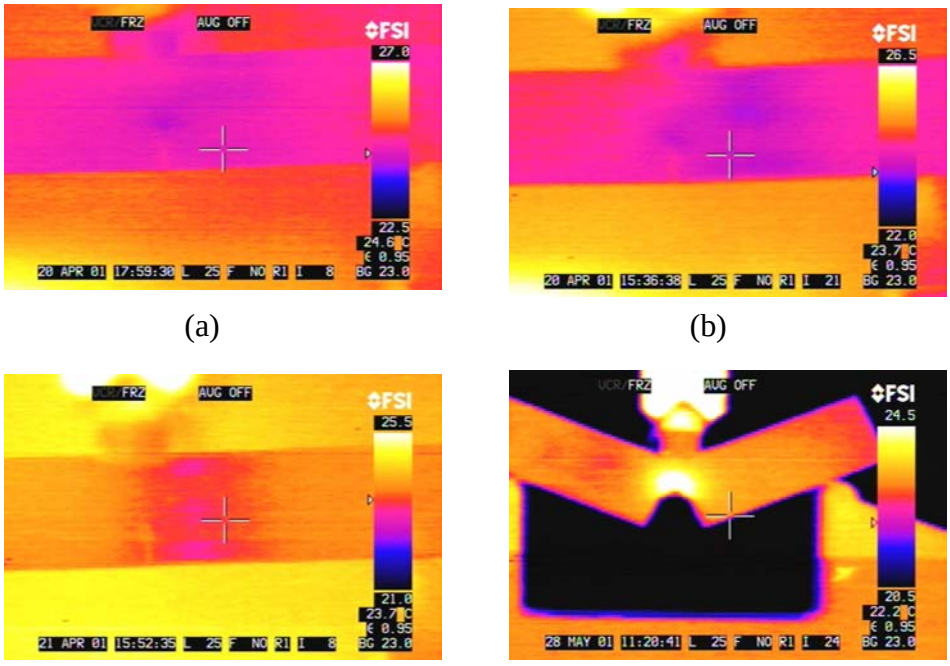

(a) (b)

(c) (d)

Figure 4.6. IR thermalwave image in real time just before failure for samples of (a)PP, (b) PP + mPP, (c) NC 1, (d)NC 5.

fracture toughness of a material is mainly defined by the plastic zone contribution. It has been found that all the methods agree with this trend. In summary the higher concentration of MLS will delay the crack propagation in the sample, generating plastic zones with high-energy concentrations that will result in a higher temperature at the ligament region and will be dissipated only by the separation (failure) of the material.

4.6. Discussion

TWI helped to confirm that increments in plasticity are the result of the increments in MLS content. As illustrated in figure 4.6, right before the failure of the specimens, it is possible to observe how the temperature profiles are different from one another. In the unfailed ligament region, an increment in the temperature is observed a consequence of the plastic deformation of the material. Here the shape and size of the plastic zone could be used to identify the fracture differences from one sample to another. I explore the deformation of materials with TWI in detail in chapter VI.

In PP, for instance, the plastic zone is small, and the fracture of PP specimens can be identified as “brittle” in comparison with the rest of the samples. As the MLS content is increased in PP, the size of the plastic zone increases, which confirms that the presence of the MLS leads to a larger plastic area. At this point, and by summarizing the data obtained before, it is possible to confirm that the plastic zone size determined the fracture toughness of the material.

Furthermore, it can be observed that the TWI imaging can be used as a method to classify materials according to plastic deformation. Figure 4.7 shows the cracking displacement for NC 5. In this series of images it is possible to see the evolution of the

bundle and the plastic zone. At the beginning, a small increase in temperature is noticeable, as in the rest of the samples. However as the test advances, the energy accumulated at the crack front produces an increment in the surface temperature which is detected by the IR camera. At this point I conclude that the plastic contribution represents the defining parameter for the final values of fracture.

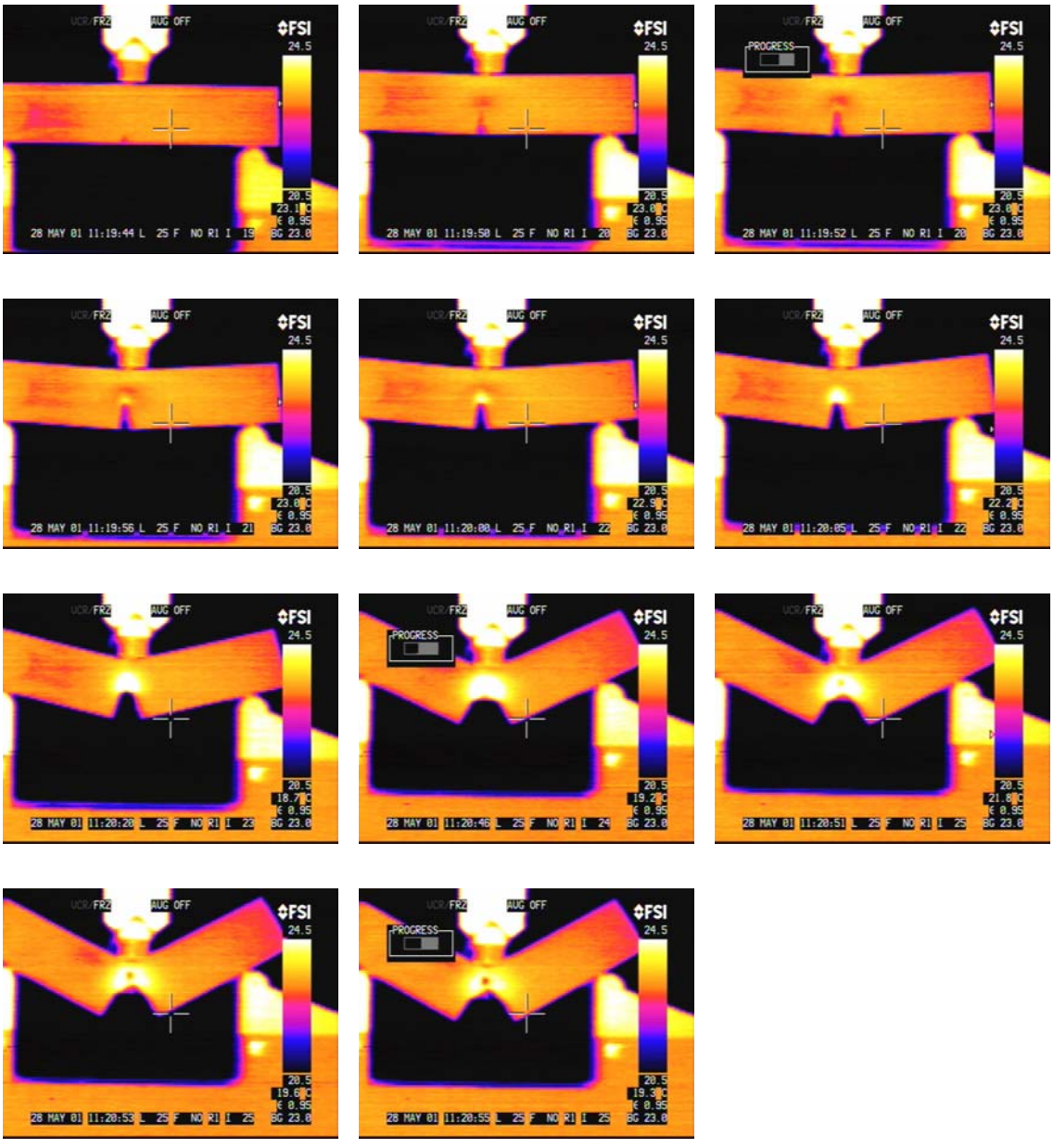

Figure 4.7. TWI sequence of NC 5 nanocomposite

The IR TW camera has system that converts the measured values of the surface in temperature values. From a microstructural point of view it, the reason for the properties of the nanocomposites are explained due to the presence of introduced heterogeneity. During the tensile test, PP chains are pulled in one direction, and the PP specimen will resist until the force applied is large enough to break the inter-chain bonding among the different polymeric units. When a foreign particle is added to the PP structure, packing of chains is altered so there will be an alteration in the bonding forces along the sample. These bonds will lead to similar values obtained for pure PP, but due to the difference in bonding forces one would experience more deformation than the other.

4.6.1. Materials effects

As was seen in figure 3.8, the addition of MLS into the PP structure will result in a reduced spherulite size, influencing the nucleation of the spherulites. However, for NC 5, there is a distribution of several spherulite sizes, and it looks as if the MLS is acting as a barrier around the spherulites, inhibiting growth. From this figure, another conclusion on the behavior of these materials can be obtained. Having similar spherulite size, PP may require a higher force in order to start the slip deformation. In the case of a size distribution this could represent both advantages and disadvantages at the same time. When a distribution of the particle sizes are present, the smaller particles, can act as reinforcement sites, stopping the larger particles from slipping. This provides a higher resistance to the crack propagation, since the crack then requires a higher energy to keep propagating. One consequence is a higher stress concentration on the crack tip (ligament area). A higher stress concentration will lead to higher values in energy and can be

understood as an increment in the temperature at the crack tip, or more properly, by the ligament region. This is observed in the TWI images.

4.7. Conclusion

The addition of MLS and mPP to the structure of PP decreased slightly the values of Young's modulus and the ultimate tensile stress, and increased the plasticity of the system. However, it significantly increased the resistance to crack propagation in the material, reaching the maximum degree of reinforcement for NC 5, where the fracture toughness reached the highest values. CTOD and J–integral techniques confirmed that this concentration, 5 %, provided the highest resistance to crack propagation. The use of TWI imaging by itself could be used to characterize the degree of plasticity in each material and define ranges of fracture toughness by analyzing the regions at the crack tip, where accumulated energy will be determined by increments in temperature in the plastic zone. Thus, the link between MLS dispersion, modified crystallinity by MLS and mPP, tensile deformation and fracture toughness lead us to conceptualize the following. In semicrystalline matrices, it is vital that the end goal be kept in mind as opposed to limiting thinking to developing the most exfoliated structure. Following the logic that more maleation would mean more penetration of MLS platelets by PP would result in using a higher than appropriate level of mPP. Here I show that lower levels of maleation ease problems of PP phase separation in the nanocomposites.

In the appendix, additional thermal images are included as well as plots with profile of temperatures indicating the progress of the failure. It is not included in the context of the chapter for practical and illustration purposes.

References

1. Walter P, Mader D, Reichert P, Mulhaupt RJ. Macromol. Sci. Pure Appl. Chem. 1999: A36: 1613-1639.
2. Nam PH, Maiti P, Okamoto M, Kotaka T, Hasewaga N, Usuki A. Polymer 2001; 42: 9633-9640.
3. Anderson TL. Fracture Mechanics, 2nd ed. New York. CRC press 1995 (chapter 1, 2 and 3).
4. Hashemi S, Arkhireyeva A. Polymer 2002; 43: 289-300.
5. Pardoen T, Marchal Y, Delannay F. Engin Fract Mechan 2002; 69: 617-631.
6. Karger-Kocsis J, Czigany T, Moskala EJ. Polymer 1997; 38: 4587-4593.
7. Chan C, Wu J, Li J, Cheung Y. Polymer 2002; 43: 2981-2992.
8. Karger-Kocsis J, Czigany T. Polymer 1996; 37: 2433-2438.
9. Karger-Kocsis J, Czigany T, Moskala E J. Polymer 1998; 39: 3939-3944.
10. Poon WKY, Ching ECY, Cheng CT, Li RKY. Polymer testing 2001; 20: 395-401.
11. Seymour BR, Carraher CE. Structure property relationships in polymers, New York. Plenum Press 1984 chapter(3, 5 and 12)
12. Bikales NM. Mechanical properties of polymers. New York. John Wiley and Sons 1971 chapter(1 and 3).
13. Rosen SL. Fundamental principles of polymeric materials. New York. Barns and Noble 1971 (chapter 17 and 18).
14. Billmeyer FW. Textbook of polymer science, 2nd ed. New York. John Wiley and Sons 1970 (chapter 6 and 7).
15. ASTM standard D 5045-99.

CHAPTER 5

TIME DEPENDENT RESPONSE OF POLYPROPYLENE NANOCOMPOSITES

5.1 Introduction

Understanding the mechanical response of PP under values of constant stress is important from a fundamental and applications point of view. The finite creep rate of polymers has been the primary reason limiting their use in structural applications. For instance, in the automotive industry finite time-dependant deformation often is a primary consideration in specific structure application of plastics. From a fundamental stand point, the influence of the MLS particulates on creep deformation has not been investigated before [1-8].

PP has a glass transition temperature below room temperature, which introduces the likelihood of a non-linear response. I have analyzed and established the existence of a non-linear response in PP at stresses below the yielding point. The characterization of the long-term behavior of polymers that exhibit nonlinear viscoelastic behavior can be obtained by the use of creep and stress relaxation analysis. Creep deformation delineates the strain increase when a specimen is subjected to a stress that is kept constant over a defined period of time. Creep compliance is then calculated by dividing measured strain by the constant stress level [9].

In a creep-recovery test measurement, strain is continued after stress is removed. In an elastic material, ideally, the material will recover its original dimensions. However, some materials will show signs of deformation or non-elastic behavior at this level. This response is known as viscoelasticity and is characteristic of thermoplastic polymers.

Several algorithms have been developed for the determination of the nonlinear or viscoelastic behavior of polymeric materials to establish time dependent performance.

Among the different classifications of composites, polymer matrix composites deserve special attention due to the specific characteristic of viscoelasticity. On application of stress, two responses result: an immediate response known as hookean or elastic contribution, and a delayed, or viscous contribution. Among the models used to explain this combined behavior are the Burger's, Maxwell, Voigt, Maxwell-Wiechert, and Voigt-Kelvin models [10-12]. All of them use analogies with spring and dashpot elements in different configurations either in parallel, series, or both. Schematic representation of these models is shown in figure 5.1.

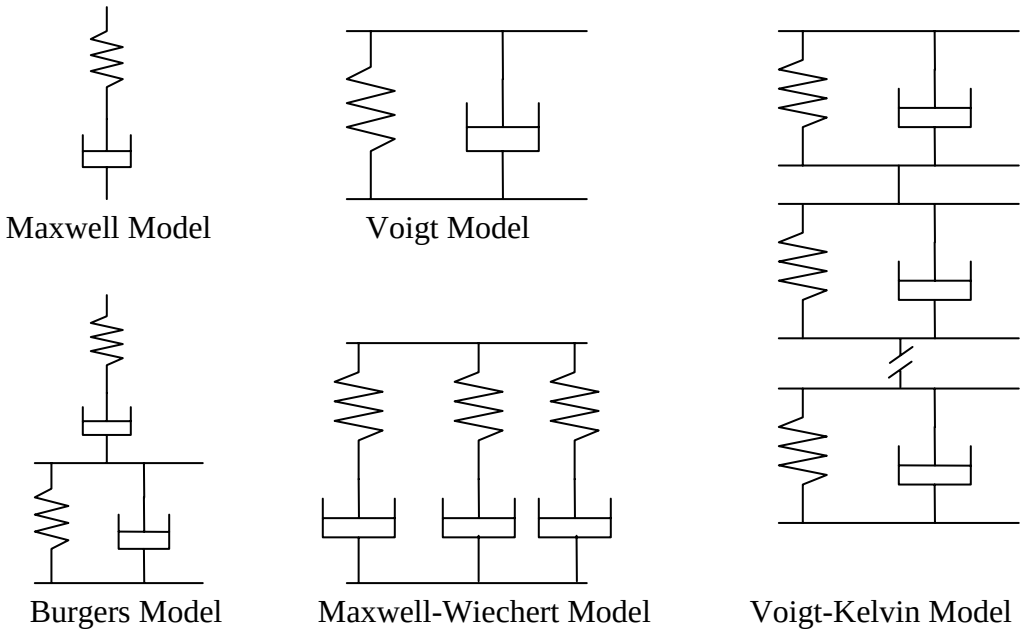

Figure 5.1 Viscoelastic models. Used with permission Dover Editors [13].

The behavior of each of the elements, dashpot and spring, is shown in figure 5.2. The mechanical behavior of the spring is represented by [13]:

$$\sigma = R\varepsilon \tag{5.1}$$

where R is the linear spring constant (or elastic modulus in the case of a material, E), σ the stress applied and ε the resultant strain. As observed in figure 5.2 the spring undergoes immediate deformation and recovery after the application of stress. The dashpot is represented by equation 5.2 [13]:

$$\sigma = \eta \frac{d\varepsilon}{dt} = \eta \dot{\varepsilon} \tag{5.2}$$

where η is the coefficient of viscosity. This equation describes how the stress is directly proportional to the strain rate. In figure 5.2 we observe the schematic representation of

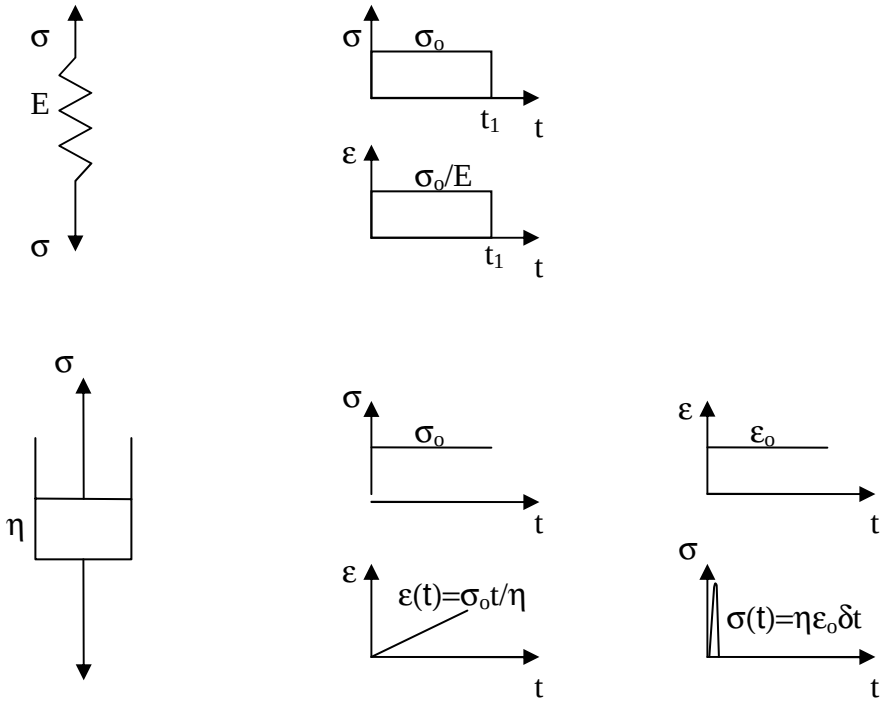

Figure 5.2 Behavior of linear spring and linear dashpot. Used with permission Dover Editors [13]

this and also how the stress increases immediately as a strain is applied and how it decreases instantaneously. From all the models sketched on figure 5.2 The Burgers model is the only one that describes polymer creep-recovery properly. A basic analysis is done in figure 5.3. The general equation that describes the Burgers model is [13]:

$$\sigma + \left(\frac{\eta_1}{E_1} + \frac{\eta_1}{E_2} + \frac{\eta_2}{E_2} \right) \dot{\sigma} + \frac{\eta_1 \eta_2}{E_1 E_2} \ddot{\sigma} = \eta_1 \dot{\varepsilon} + \frac{\eta_1 \eta_2}{E_2} \ddot{\varepsilon} \qquad (5.3)$$

Burgers model describes the four stages in the creep-recovery processes, stressing, strain at constant load, unloading and recovery. Other models may describe only some of these stages which limits the accuracy of the results and its interpretation.

5.1.1. Viscoelastic response

Several algorithms have been developed for the determination of the nonlinear or viscoelastic behavior of polymeric materials [9, 10, 11]. Among them, Lai and Baker

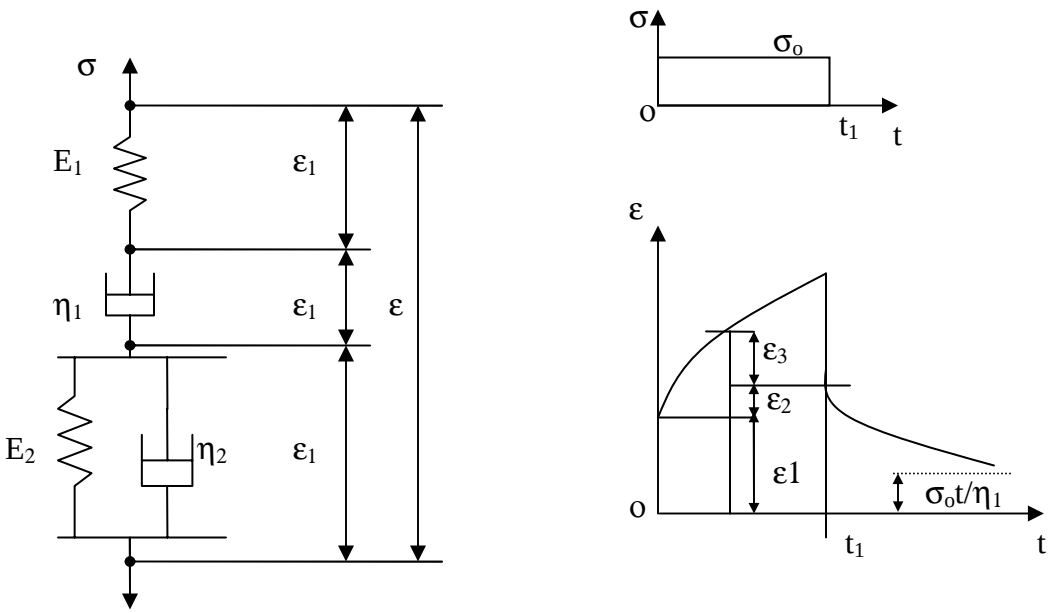

Burgers Model Creep and recovery

Figure 5.3 Burgers model. Used with permission of Dover Editors[13].

[12] have developed an equation for nonlinear viscoelastic behavior for high density polyethylene (HDPE), where only creep and recovery data are needed to determine the material properties. They investigated non-linear behavior using values of stress below the elastic limit on HDPE and predicted a master curve with this behavior over time. A master curve is a prediction in time built from individual contributions at different stress or temperature values.

In analogy with the well known WLF equation for the time temperature superposition, Lai and Baker developed an equation based on the time-strain superposition of materials to determine the effect of time on a material based on variation in stress, suggesting the relation between creep compliance at two different stress levels as:

$$D(t_1, \sigma_1) = gD(\frac{t}{a_\sigma, \sigma_2}) \tag{5.4}$$

where *log* a_σ and *log g* are the horizontal and vertical shift factors, respectively. The shift factor is related to the WLF equation:

$$\log a_\sigma = \frac{C_1(\sigma - \sigma_s)}{C_2(\sigma - \sigma_{s)}} \tag{5.5}$$

where C_1 and C_2 are constants, and σ_s is a reference stress, and then the unified expression for creep strain ε_c as function of time can be formulated as follows:

$$\varepsilon_c(t) = \sigma g\overline{D}(\frac{t}{a_\sigma}) \tag{5.6}$$

Here, the presence of time effect is defined by a_σ and g, which are the horizontal and vertical shift factors respectively. $\overline{D}(t)$ is the reference creep compliance [12].

Many procedures have been developed to explain the behavior of polymers in the non-linear region. However, creep is one of the simplest and more reliable. In fact, Lai and Baker's model is based on a prior work reported by Schapery [13]. In the Schapery method, creep and recovery curves are simultaneously shifted vertically and horizontally to create a single master curve.

The Lai and Baker model is utilized here for the construction of the master curves of compliance from the material as a function of time. However, to explain the viscoelastic response properly, materials deformation description is also important. Schapery's model to determine these structural parameters is shown in equation 5.7 [16, 17].

$$\varepsilon_c(t) = g_0 D_0 \sigma_0 + g_1 g_2 \Delta D\left(\frac{t}{a_\sigma}\right)\sigma_0 \tag{5.7}$$

where g_0, g_1, g_2, a_σ, are time-dependent, but stress dependent non linear parameters. For a reference state $g_0 = g_1 = g_2 = a_\sigma = 1$, then the system has linear response. D_0 represents the instant compliance or time-independent (elastic) compliance, ΔD the transient or time-dependent compliance. σ_0 is the constant stress and t the time. Zaoutsos et al. [17] proposed a viscoplastic term ε_{vp} to consider the plastic response, but this concept is not applied in our work. Master curves can be built following a combination of methods among the Lai and Baker method to obtain the compliance at every stress value, and using graphic fitting from Schapery theory obtaining the vertical and horizontal shift factors. The structural parameters can be calculated from the data obtained during the test. In order to obtain the non linear structural parameters mentioned above, the

following methodology can be used. For the shifting, a reference compliance D_0 is chosen to start the plotting of the master curves, at this stage $g_0 = g_1 = g_2 = a_\sigma = 1$. The predicted shifted factors are proportional to logarithmic relationships among these factors, $\log[g_1(D_0)g_2(D_0)]$ for the vertical and $\log[a_\sigma(D_0)]$, and by these means, the values for each structural parameter can be obtained.

5.2. Experimental procedure

5.2.1 Materials

The materials employed were pure semi-crystalline PP (PP), a blend of the same PP with mPP (polybond 3150) and MLS (Cloisite®15A) to form nanocomposites (NC) with concentrations of 1, 2, 3, and 5 weight %content.

5.3. Results

Tensile tests were performed on all the specimens to determine the magnitudes of the constant stresses, and then determine the elastic region and determine the stress level to use for the creep-recovery cycle for the analysis. Figure 4.4 in chapter 4 sketches the stress-strain behavior plots that were obtained.

The stresses, or loads, applied were selected related to the tensile test, since the application of stress above the elastic limit will lead to plastic deformation. A series of values below the elastic limit have been applied to the samples in order to evaluate the visco-elastic behavior of each specimen. Stresses of 2.5, 5, 7.5, 10, 12.5, 15, and 17.5 MPa were applied. Since the reference material is the PP (the material to reinforce), this was selected as a basis for comparison. Figure 5.4 shows the non-linear behavior of PP as

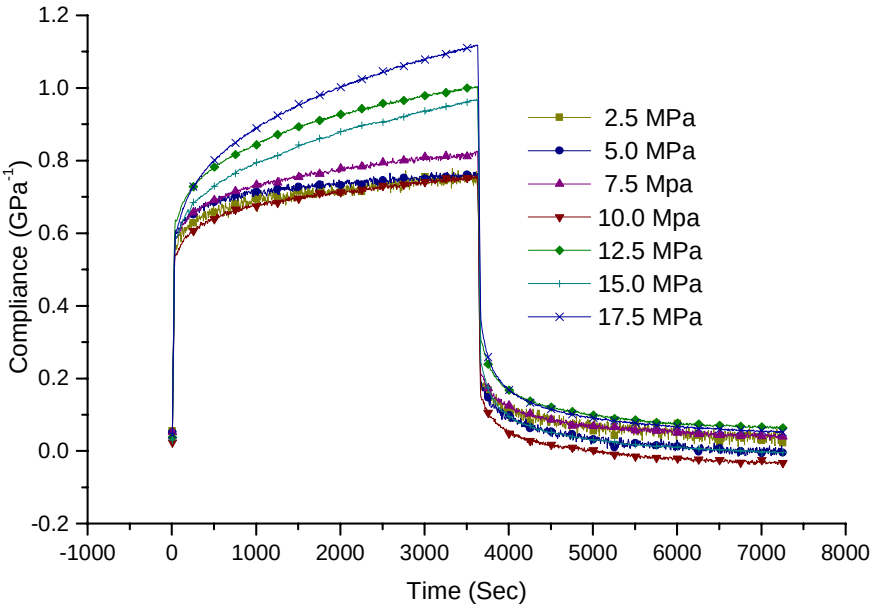

Figure 5.4. Creep – recovery cycle for PP

stressed, and how the recovery is not complete. The unrecovered strain increases with the stress as the stress value approaches the yield point. Even when all the stresses are under the values of the elastic limit, it is possible to observe that the sample has a non-linear response. Once the stress is removed, a total recovery of the sample is expected and compliance should go to zero. However, in some of the cases as the stress increases, the sample shows a difference between the changes during stress and during recovery. This unrecovered deformation indicates not only a non-linear response but also a permanent deformation in the materials. The final deformation in each sample could be used to distinguish the performance of each sample. Figure 5.5 shows the differences, considering the ratio of final deformation to elastic modulus. Plots showing the characteristic creep-relaxation behavior for several specimens tested are included in the appendix.

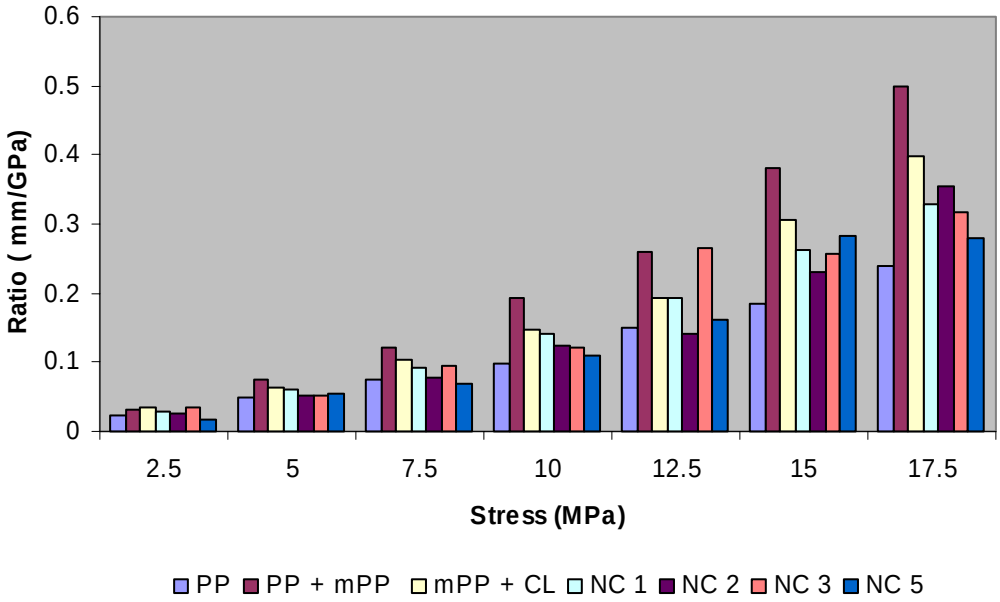

Figure 5.5. Differences in the final deformation of samples

Analyzing the individual performance of each sample at different stress values, we can see that PP has a better performance for the entire range of stresses since the elastic modulus is higher, and at the end the deformation is the minimum. NC 5 has the next best performance in terms of plastic deformation to initial compliance of PP. At 2.5 MPa the value is much lower than that of PP and it has a similar value up to 12.5 MPa which has to be considered in the overall performance, since I am reporting lower deformation due to its slightly lower elastic modulus. At the end of the test it has a high deformation related to the PP but much lower in comparison with the rest of the samples. On the other hand, the specimen PP + mPP has the highest deformation of all, which is expected.

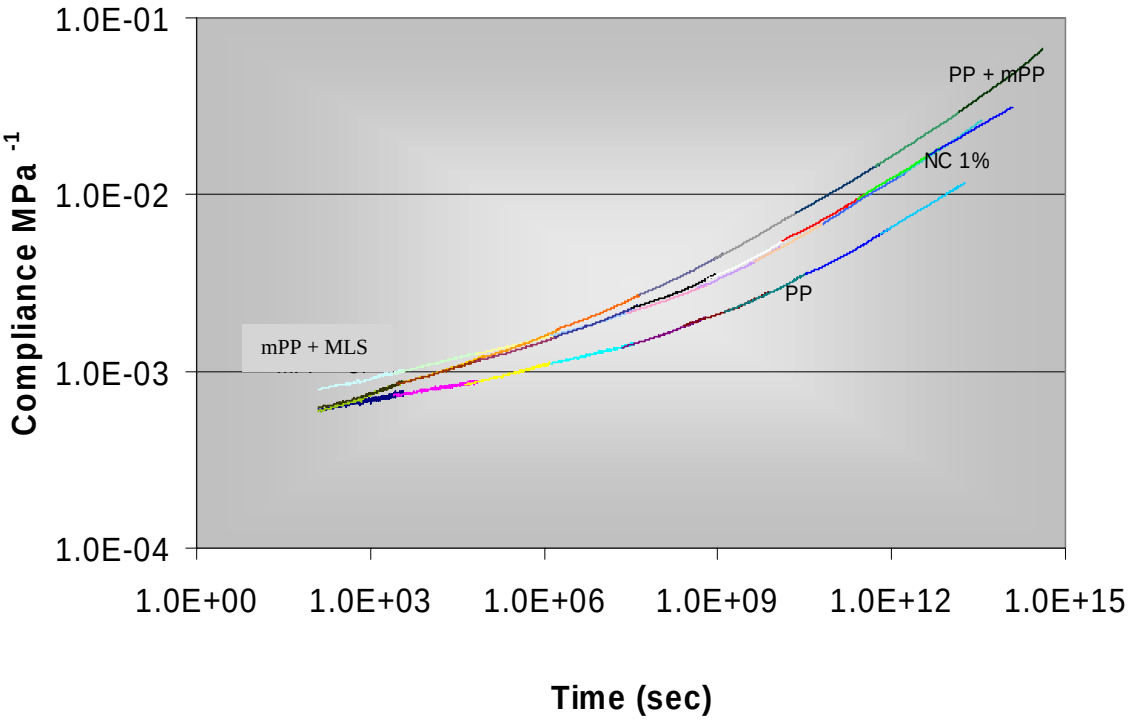

Figure 5.6 master curves for PP and PP with some additives

Viscoelastic behaviors are characteristic of polymer matrices and materials that have been subjected to constant stress for a long period of time. Creep–compliance curves will be similar for any kind of material, with differences primarily related to the magnitude of their compliance. The real differences are noticed when the behavior in time is considered. To do this, master curves are projected using the values of compliance. Characteristic master curves for PP and PP + mPP and NC1 are shown in figure 5.6. The lower compliance of PP is observed compared to the rest of the materials. The addition of mPP to the matrix resulted in a higher ductility in creep similar to that shown in the tensile test. The addition of MLS also influenced the compliance. The

addition of MLS decreased the compliance of the blend with only PP and mPP. However, the concentration added is not enough to equal the behavior of PP itself. Figure 5.6 also shows the behavior of mPP + MLS only. It can be seen that this specimen has a different behavior than the rest. It has a lower increment in the compliance, but the values are not greater than the PP specimen. In addition, the tensile test did not show a good performance in the immediate response as showed in the previous chapter.

In figure 5.7 the effect on the compliance as the MLS content increases in the matrix is examined. The addition of 2 % MLS to the matrix, NC 2, did not represent a

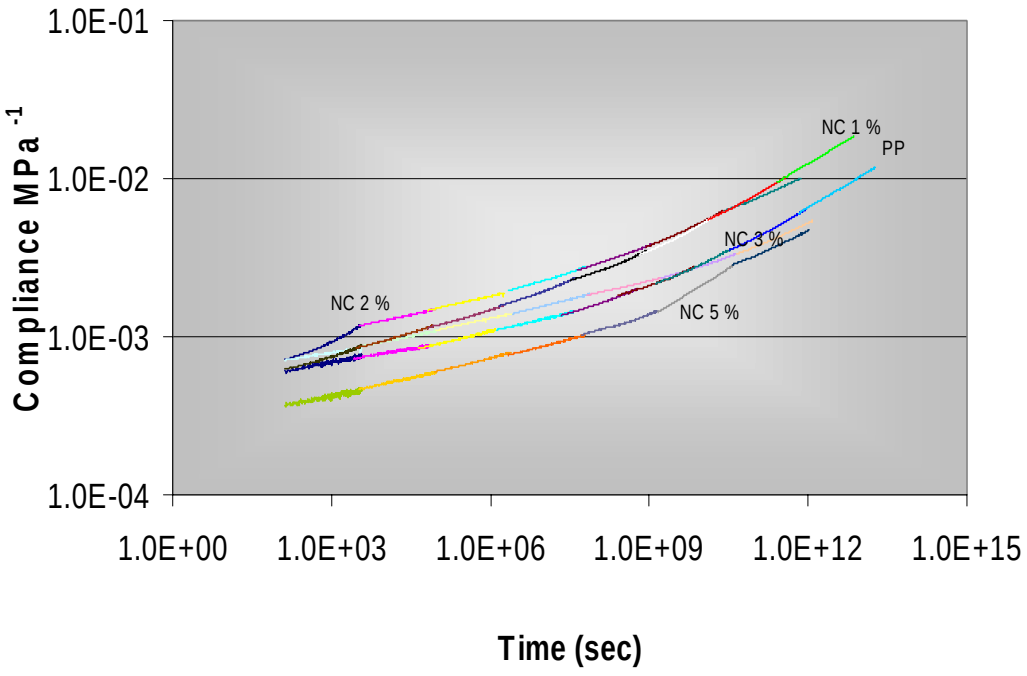

Figure 5.7. Master curves for PP and PP nanocomposites

noticeable difference in the compliance properties, and its behavior is similar to NC 1 but with a higher compliance in the initial stage. NC 3 shows a similar behavior in the early stages of creep, however, the compliance does not increase as observed at the lower concentrations of the MLS. The lower final deformation is that of PP. At this point, I can say that any increase the MLS concentration reduces the compliance.

Master curves using 2.5 MPa as the reference stress in equation 5.6 were analyzed. Equation 5.6 uses two parameters known as vertical and horizontal shift factors. These factors are structure dependent and are obtained from analyzing experimental results. Since they are material dependent, they will change from one sample to another. Also, due to their correspondence with the structure of the material, they can indicate the degree of linearity and non-linearity of the system. In figure 5.8 and

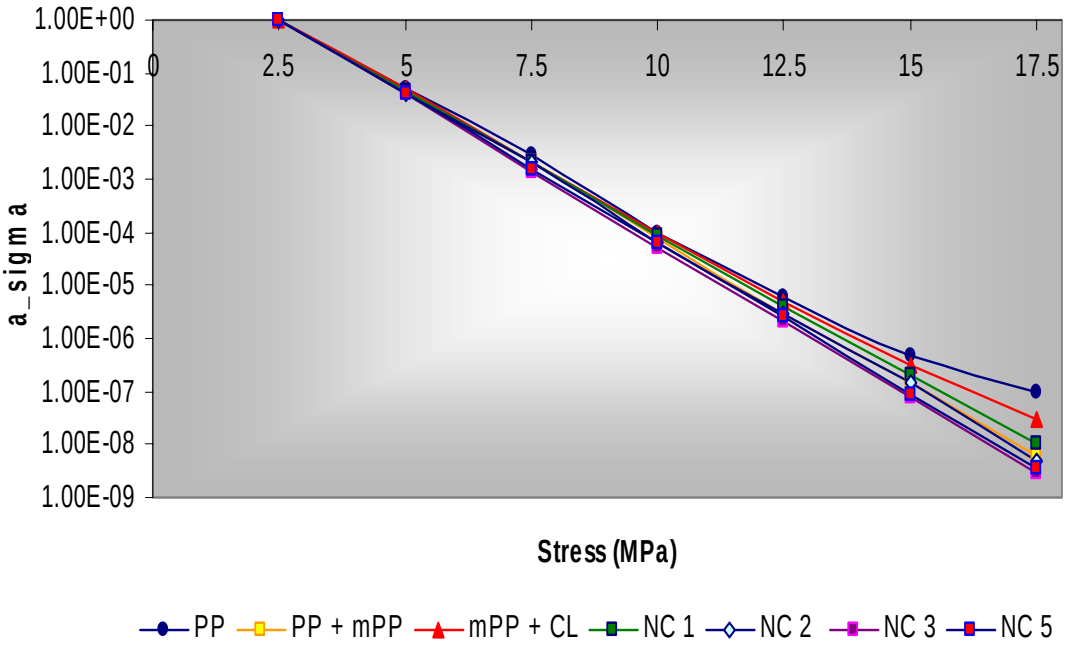

Figure 5.8. Horizontal shift factors in creep

5.9 the vertical and horizontal shift factors are shown. From the creep curves, as explained, $g_{1*}g_2$ are obtained but for stress equal to zero in recovery g_2 is obtained. This separates out the stress effect from the materials effects.

The shift factors basically indicate the non-linearity of our system. The horizontal shift factors are related to the time dependence. Figure 5.8 shows that these were largely material independent. In figure 5.8, the plots have variations only at higher stresses, when values close to the elastic limit are reached.

Figure 5.9 shows the vertical shift factors in creep. These factors are directly related to the structure of each sample and it can be seen that their values are quite different from each other. If we observe the plots, the most ductile system, PP + mPP, is the most regular, while the NC 5 oscillates in a periodic fashion. As mentioned, these

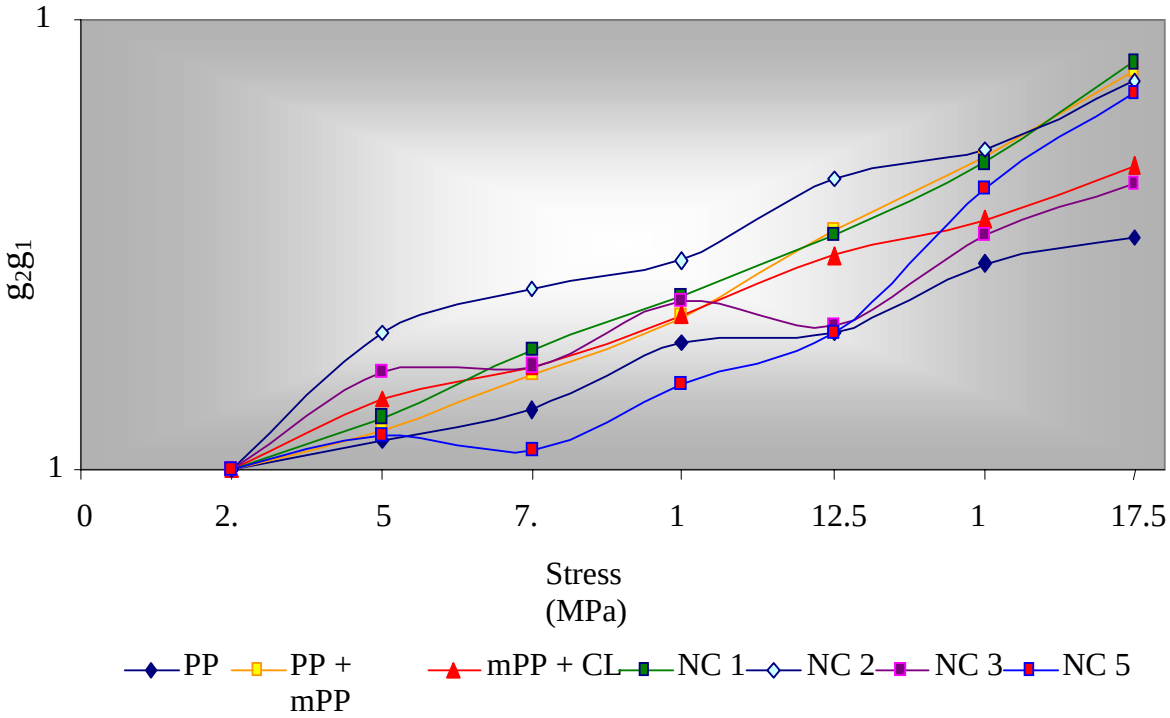

Figure 5.9. Vertical shift factors

vertical shift factors are structure dependent, the addition of compatibilizer to the PP will decrease its viscosity making the distribution of the stress easier. In other words, the system is more susceptible to the application of the stress. When a more complex system is evaluated, the interactions among each component, at some regions will stop or will yield depending of the concentration either of MLS or PP.

The deformation of the nanocomposites will be mainly through the bonds between PP molecules, rather than in the union with the MLS. It is logical that at some point the stress applied leads to a higher deformation, that is then stopped by the chemical interaction with the MLS leading to the wavy behavior observed.

The separation of the materials contribution and stress contribution can be observed in figures 5.10 and 5.11 respectively. In figure 5.10 it is observed how two

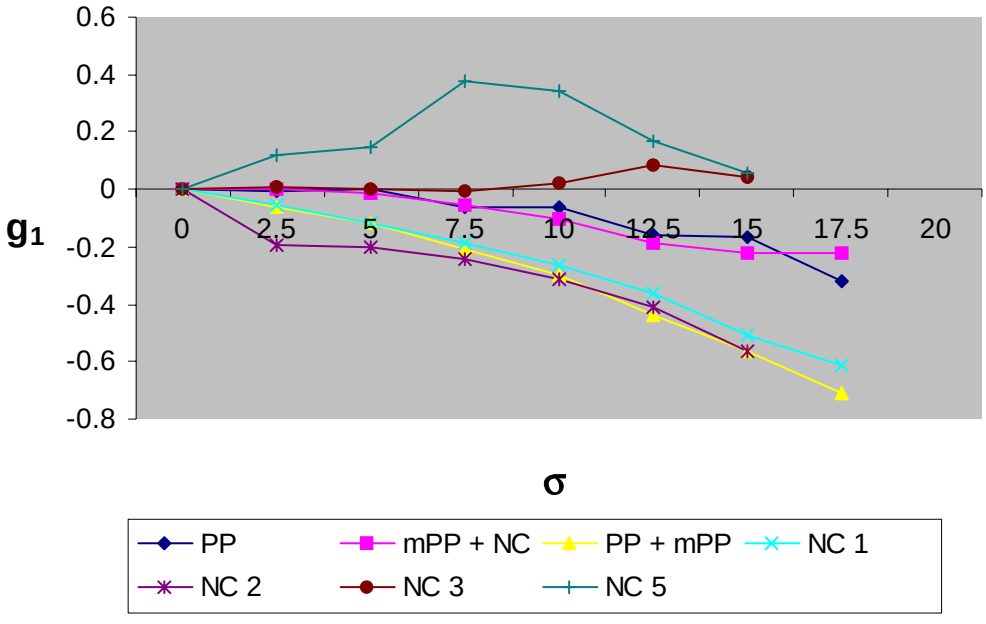

Figure 5.10. Materials contribution to creep

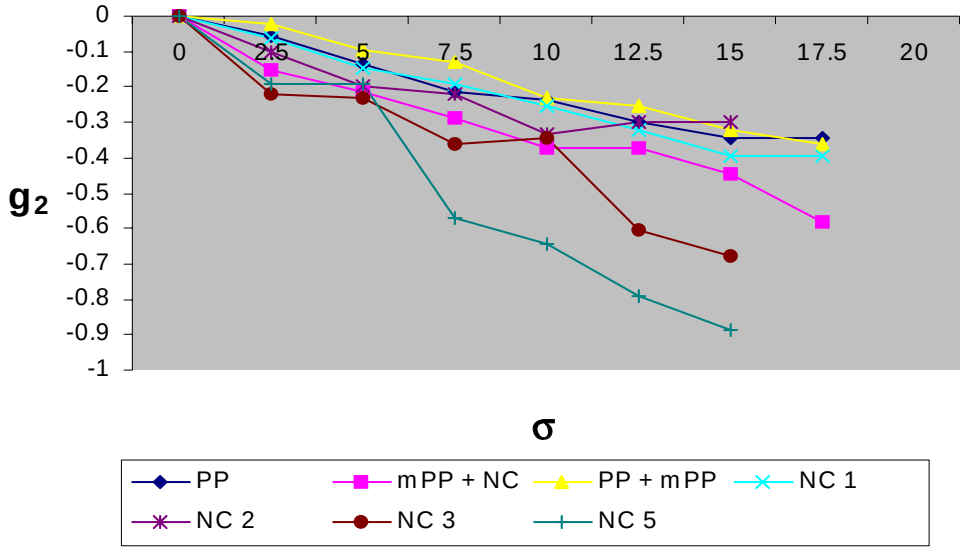

Figure 5.11. Stress contribution to creep.

specimens NC3 and NC 5 have a different trend than the rest. If we look back to figure 5.7 we will see that these are also the two concentrations that provide a lower compliance than the original PP. Then we can see again that the behavior the specimens is material dependent, since the structural contribution in figure 5.11 shows a uniform trend for all the specimens.

Figure 5.12 shows the elastic compliance in the creep and recovery stages. As can be seen, any change in the structure of PP is translated to higher values of compliance, or deformation in a given system. A different effect is observed when different MLS concentrations are added to the PP matrix.

As we can see in figure 5.12 the absolute values of compliance are lower, but what is noticeable is the oscillation of the compliance curves, especially in NC 3 and NC 5. This effect is similar to the one that the vertical shift factors showed. If we

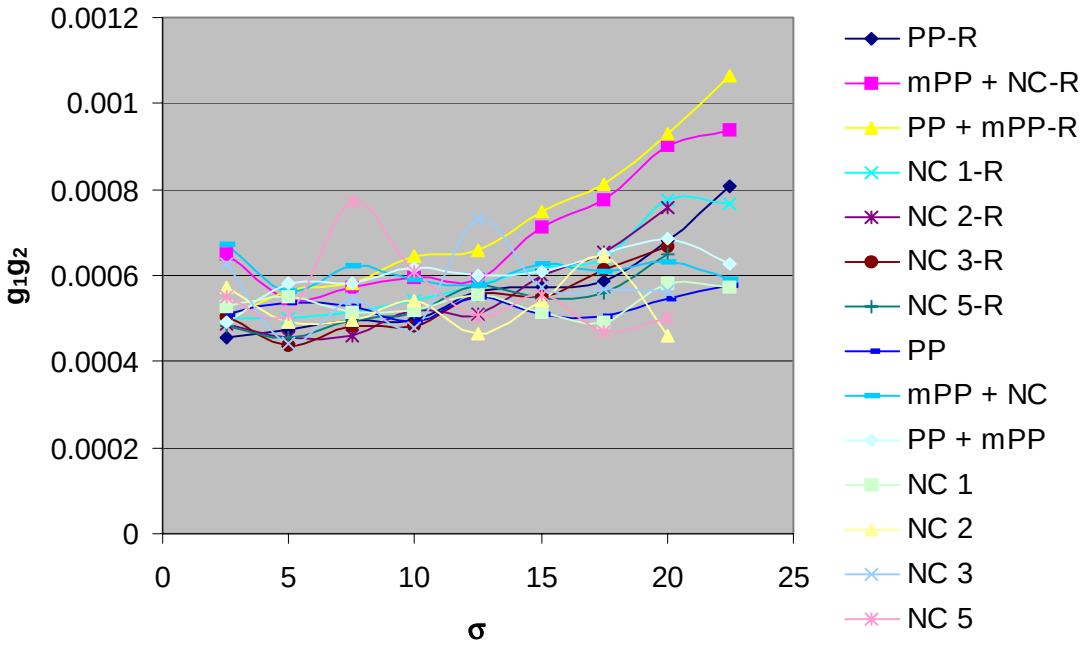

Figure 5.12. Variation on response in the specimens.

go back in the analysis an recall the behavior during creep tested showed, these are the two values that have lower final (and overall) compliance than the PP.

This is explained again by the structural differences between these, and reinforces the initial theory about addition of MLS and mPP. The addition of mPP increases the toughness of the system, leading to a more ductile material that will undergo a higher degree of deformation. This has been noted at all the stages of the mechanical testing. The addition of low concentrations of MLS increases the stiffness of the matrix and shows higher compliance in comparison with the PP and PP + mPP samples. Another observation from figure 5.12 is that the recovery plots are always above the creep plots which implies that there is different behavior at each stage, and that this leads to a different structure in recovering.

From the structural point of view, there are methods that can be used to analyze the degree of deformation in the specimens. Figure 5.13 shows X-ray diffraction spectra for the NC 1 sample. It can be observed how the displacement of the peaks is indicative of the deformation in the sample. Similar to the respective creep plots, the deformation is not completely linear. The range selected was chosen to highlight the peak with higher intensity, but the trend is similar along the entire range. Figure 5.13 shows how all the samples loaded have a displacement of the peaks from the original PP.

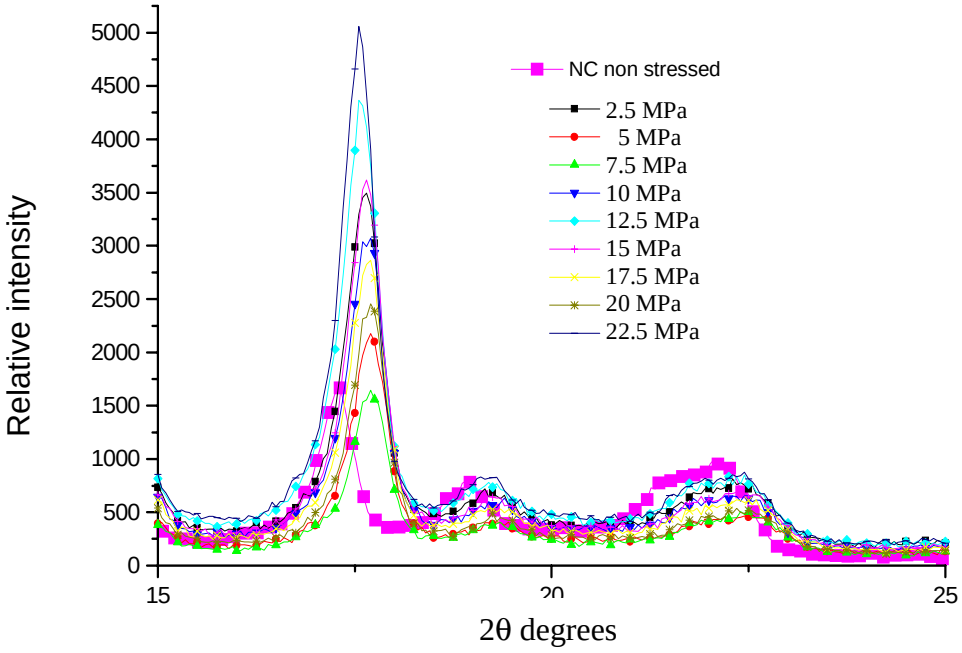

Figure 5.13. X-ray diffraction spectra for NC 1.

Table 5.1 Ratio of intensities for surface, inner and strained samples.

	$I_{16°}/I_{14°}$		
	Surface	**Inner**	**Strained**
PP	3.8	2.26	2.68
mPP	0.67	-	-
PP + mPP	1.08	0.95	1.39
mPP+Clay	0.96	0.99	1.19
NC 1	2.28	1.47	5.46
NC 2	4.79	2.72	6.99
NC 3	3.31	1.21	8.55
NC5	7.64	1.72	10.53

In table 5.1, it is possible to see the behavior of the strained sample in comparison with the inner and surface specimens analyzed in chapter III. Following a similar discussion as in chapter III, we observe that the strained sample retains the same structure as the surface. The retention of this monoclinic structure indicates a strong presence of MLS in the area analyzed, which could be considered as normal since the deformation of the specimen will retain the MLS, while the main deformation and any other deformation effects are observed in the polymer component.

5.4. Conclusion

The creep compliance trends differ from the one obtained in the tensile tests indicating that the nanocomposite creep deformation is highly dependant on the strain rate of the experiment.

It was found that the creep response of the material is mainly material dependent, and that NC 3 and NC 5 differ from the rest of the specimens, resulting in the two concentrations that show lower compliance that the base material, PP.

References

1. Kornmann X, Berglund LA, Sterte. Jour Polym Eng Sci 1998: 38: 1351-1358
2. Alexandre M, Dubois P. Mater Sci Eng 2000; 28: 1-63
3. Walter P, Mader D, Reichert P, Mulhaupt R. Jour Macromol Sci Pure Appl Chem 1999; A36: 1613-1639.
4. Okada A, Kawasumi M, Usuki A, Kojima Y, Marauchi T, Kamigaito O. Mater Res Soc Proc 1990; 171 :45-50
5. T. J. Pinnavaia. Science 1983; 220(4595): 365-371.
6. P.B. Messersmith and E.P. Giannelis. Chem Mater 1998; 5: 1064-1066.
7. Own CS, Seader D, D'Souza NA, Brostow W. Polymer Compos 1998; 19:107-115.
8. Hernandez-Luna A, D'Souza N.A. SPE ANTEC 1999.
9. Brueller OS, Steiner H. Polymer Eng Sci 1993; 33:1400-1403.
10. Rosen SL. Fundamental principles of polymeric materials. New York. Barns and Noble 1971 (chapter 17 and 18).
11. Seymour BR, Carraher CE. Structure property relationships in polymers, New York. Plenum Press 1984 chapter(3, 5 and 12)
12. Bikales NM. Mechanical properties of polymers. New York. John Wiley and Sons 1971 chapter (1 and 3).
13. Findlay WM, Lai JS, Onaran K. Creep and relaxation on nonlinear viscoelastic materials. New York. Dover publications1976 (chapter 1).
14. Lai J, Bakker A. Computational Mechanics 1996; 18: 182-191.
15. Lai J, Bakker A. Scripta metallurgica et materiala 1993; 28: 1447-1452

16. Augul JM, Land DJ. Jour App Polymer Sci 1985; 30: 4203-4233.
17. Zaoutsos SP, Papanicolaou GC, Cardon AH. Composites Sci Tech 1998; 58: 883-889.
18. Zhu D, He D, Zheng M, Gu Y. Heat transfer-Asian research 1999; 28(2) 89-94.
19. Merchant J. The infrared temperature handbook.
20. Godovsky YK. Thermophysical prop of Polymers. New York. Spanger-Verlag 1992 (chapter 1, 4, 6, 7 and 8).

CHAPTER 6

THERMAL WAVE ANALYSIS OF THE MECHANICAL DEFORMATION OF POLYPROPYLENE NANOCOMPOSITES

6.1 Introduction

The quest for new characterization techniques is always a priority in order to understand and study the behavior of materials For instance, the use of nondestructive techniques enables examination of actual pieces employed and provides reliable information about their performance. Thermal imaging is one of the techniques that has been used to provide valuable materials information. In the past, pyrometers and other temperature measuring instruments were used [1-9]. Thermal wave infrared imaging (TWI) has experienced fast development and has provided useful information in different fields.

The plasticity of materials studied in chapter IV has been used to correlate the increased ductility of nanocomposites to the presence of mPP. Interpretation of the strength of materials and fracture mechanics approaches at room temperature were both based on the analysis of force deflection data, while considering the crack effects. The differences in ductility were correlated to spherulitic size. Here TWI is used as a tool to follow the deformation experienced for polymeric nanocomposites under conditions of constant and variable stress. I show it as a useful technique for the non-destructive analysis of deformation. A unique understanding of deformation mechanics is obtained through visualization of this deformation and understanding stress induced crystallization and plasticity development during the test. This is facilitated by thermal imaging.

A thermal wave camera followed all the mechanical testing presented in order to analyze the deformation in specimens as the test advances.

6.2. Thermodynamics of mechanical deformation and rupture

6.2.1. Plastic and Elastic Deformation

Deformation in solids is normally treated as a subset of stress-strain data interpretation. Godovsky [10] has elegantly explained the relationships among deformation and temperature changes for polymers, using thermodynamics. For some purposes, this mechanical approach is enough to explain the deformation of the material. However, when it is necessary to relate the response of the material to thermodynamic potential as internal or free energy rather than in terms of potential energy, additional relationships need to be considered. The first law of thermodynamics states that energy is conserved in all deformation processes. Therefore, the mechanical response of any material reflects the amount of energy which accompanies the deformation process as enthalpy, or internal energy changes. In other words, thermal variations brought about by adiabatic or isothermal processes have to be measured simultaneously with stresses and strains. A schematic diagram of thermo-mechanical behavior of an ordinary polymer is sketched in figure 6.1.

After a small amount of initial cooling, resulting from stress induced crystallization, an evolution of heat accompanying the beginning of the plastic deformation occurs. The appearance of plastic deformation is accompanied by heat evolution, independent of whether it is localized (necking) or distributed along the

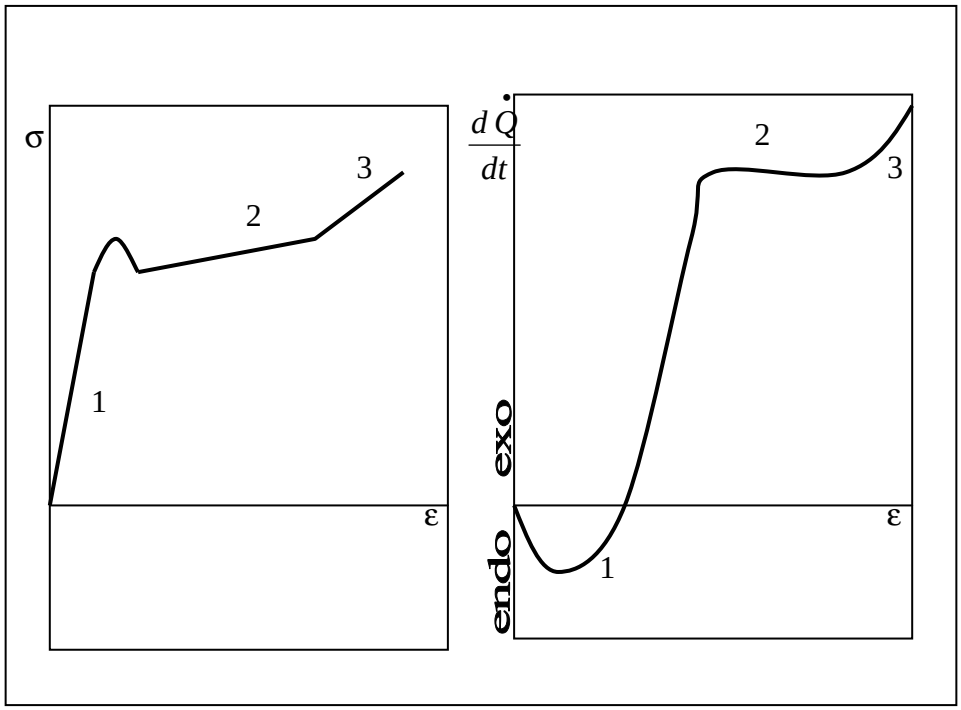

Figure 6.1. Thermo-mechanical behavior of polymers at simple extension. (1) Elastic deformation. (2) Cold drawing of plastics. (3) Plastic deformation . Used with permission of Springer-Verlag GmbH & Co.KG [10].

sample uniformly. If the plastic deformation is accompanied by neck formation, then, the heat generated locally may lead to considerable local temperature rise.

The starting point of thermodynamic analysis of plastic deformation of solids is the energy balance of deformation. Because the first law of thermodynamics is valid for all deformations, its application to the plastic deformation allows the calculation of internal energy changes during plastic deformation. The possible mechanisms for energy storage during uniaxial tension that can be found in a polymer include the following [10]:

1. In crystalline polymers, the most significant energy change is related to changes in the degree of crystallinity during deformation. This source of internal energy change may be both positive and negative.

2. The second source of internal energy changes is the intramolecular conformational transitions. The heat dissipated during the reversible deformation of glassy polymers consists of two parts: the heat resulting from conformational changes and the heat resulting from intermolecular friction. This can be applied to the changes of conformational entropy and conformational energy of the amorphous regions of crystalline polymers.

3. An important source of energy storage may be related to the appearance of internal stresses. Normally such stresses can relax very slowly and their relaxation will be accompanied by the emission of the corresponding energy, and with a transition of the deformed polymer to a more stable state.

4. In deformed solid polymers, the internal energy change may be the result of intramolecular changes, in particular due to the breaking of the hydrogen bonds.

5. Plastic deformation of glassy and crystalline polymers is accompanied with the formation of new surfaces (crazing and fibrillation), where work is spent.

6.2.2. Thermodynamics of elasticity

The first law of thermodynamics defines the internal energy as

$$U = dq + dw \tag{6.1}$$

From the second law of thermodynamics we can define the change in entropy in a reversible process as:

$$TdS = dq_{rev} \quad (6.2)$$

In our case I refer basically to the elastic region, where the material that has been strained can return to its original conditions once the stress is released. Combining equations 6.1 and 6.2:

$$dU = TdS + dw \quad (6.3)$$

Helmholtz energy is defined as A= U – TS; considering this concept at constant temperature:

$$dA = dU - TdS \quad (6.4)$$

combining equations 6.3 and 6.4 then we got:

$$dA = dw \quad (6.5)$$

In a mechanical system the work refers to that done by the applied stress. If the tensile force is f and l is the initial length of the elasticity specimen, the work done in creating an elongation dl is:

$$dw = fdl \quad (6.6)$$

From equation 6.4, for any change:

$$dA = dU - TdS - SdT \quad (6.7)$$

but in a reversible process:

$$dU = fdl + TdS \quad (6.8)$$

From this equation 6.8, it is possible to conclude that the change in the internal energy of a material is a consequence of two contributions. The first is related to the energy changes due to applied force or mechanical contributions. The thermodynamic contribution basically consists of the change of entropy at constant temperature. This last

contribution could be positive or negative, depending upon a negative or positive change in entropy. [11]

Another theory that is commonly used in temperature deformation relationships is derived from the work of Lord Kelvin. This theory relates directly the stresses in the materials to the changes in temperature by what is known as the material thermoelastic constant K_m:

$$\Delta T=-K_m T\Delta\sigma \tag{6.16}$$

K_m is defined by:

$$K_m = \frac{\alpha}{\rho C_p} \tag{6.17}$$

where α is the coefficient of thermal expansion, ρ the density and C_p the heat capacity and $\Delta\sigma$ is the change in principal stresses.

This approach requires further analysis to the one above, since particular values of density, coefficient of thermal expansion and heat capacity will change accordingly with the MLS content.

6.3. Imaging techniques

6.3.1. History

Non-destructive analysis of the structure of bodies has its beginning in the development of photo acoustic analysis, where a spatial distribution of matter is perturbed by a time varying interaction with an electromagnetic field. This concept is then applied to the development of thermal analysis, by measuring the change of temperature in time instead of deformation distributions. Both nondestructive testing and

analysis of temperature changes can be related to determine the deformation of the material based on the changes in temperature.

Early techniques used for photothermal analysis used probe beams to monitor the variation of reflective index. Among these are thermal lensing, interferometry, laser beam deflection, transient gratings, and reflectometry. Important developments were reached when infrared radiometry and pyroelectric sensors were introduced in the detection of the surface temperature variation of solids. Many other techniques have been suggested and used, and have led to the development of the thermal wave analysis technique [1]. Two methods are generally followed, dependent on the detector. In pulse-echo techniques a flash lamp is used and images are acquired synchronously. Alternatively, images can be obtained in real time.

Thus, it is important also to note that despite the fact that all techniques provide useful information about changes in the temperature or structure of the specimens under analysis, not all of them provide a real time measurement. This is because in pulse-echo techniques a signal is sent but it is the echo signal that will provide information. The gap between these signals will not be separable.

Thermal wave imaging can be considered more as a development from photoacoustics than from thermography. Thermal wave techniques are based on the modulated thermal response of a medium. The mirage effect, piezoelectric detection, thermal dependence of reflectivity and infrared detection are techniques that use the principle of thermal wave imaging. The last method is the closest related to thermography. A thermal wave is the response of a medium to a periodic heat source. It

takes the form of a temperature oscillation which propagates away from the source, usually into a solid. [7,8]

6.3.2. Principle

The thermal wave imaging technique is a based on the principle that the sample under investigation is illuminated with light whose intensity depends on time. The dependence can be periodic, pulse shaped, or modulated in a statistical way. A certain part of the radiation is absorbed by the sample and results in a temperature increase as a function of both time and position. From the temperature dependence of the sample one can derive in various ways photothermal signals providing information on optical, thermal, or structure properties. When using photothermal signals, finding or generating the signals is not a problem, the way in which the thermal wave is generated (optical absorption, heat diffusion), how it is observed, and the interpretation of the signal itself represent the major difficulty in the technique.

Different principles apply depending on the interaction or signal to be evaluated. When the signal is derived from the surface; temperature is explained by the principle of photothermal radiometry. Thermoreflectance, on the other hand, describes surface deformation, depending on surface reflectivity, temperature and optically generated charge carriers. This last application is mainly used in thin film semiconductors [2].

In photothermal radiometry the quantity under investigation is the change of thermal radiation emitted from the sample of a surface element Δf. If the reflectivity R_{IR} does not change much with the wavelength the signal S is proportional to:

$$S(t) \propto \iint_{\Delta f} (1 - R_{IR}) 4\sigma_B \beta_{IR} T^3 \left[\int_0^{\infty} \Delta T(x, y, z, t) e^{(-\beta_{IR} z)} dz \right] dxdy \qquad (6.9)$$

with $\Delta T = T(x, y, z, t) - T_{environment}$, β_{IR} is the infrared absorption coefficient and σ_b the Stefan-Boltzman constant. The essential advantage of this technique is the fact that the signal is obtained through non-contact means. The shape of the objects can be arbitrary, however, one has to make sure that the quality for imaging a sample spot on the detector is good. Signal evaluation may be complicated if the sample is transparent or reflective in the infrared spectral range.

Thermal properties of materials affect thermal waves in two different ways: amplitude is determined by the effusivity $e = (kC)^{\frac{1}{2}}$ and spectral decay by the diffusivity a = k/C. Diffusivity and effusivity are related. Therefore thermal insulators give a high amplitude whose decay times are very short, so that the depth range is small. On the other hand thermal conductors give small amplitudes and a depth range, which is typically larger by an order of magnitude [2].

Any object emits radiation in a continuous way, depending only on the object and its spectral emissivity. A black body, an object for which absorption is maximum, makes a perfect radiator. The energy emitted by a black body is the maximum theoretically possible for a given temperature. The radioactive power (or number of photons emitted) and its wavelength distribution are given by the plank radiation law

$$W(\lambda, T) = \frac{2\pi hc^2}{\lambda^5} e^{(\frac{hc}{\lambda kT})^{-1}} Wcm^{-2}\mu m^{-1} \qquad (6.10)$$

$$P(\lambda, T) = \frac{2\pi c}{\lambda^4} e^{(\frac{hc}{\lambda kT})^{-1}} photons \cdot s^{-1} cm^{-2} \mu m^{-1} \qquad (6.11)$$

where λ is the wavelength, T the temperature, h is Planck's constant, c is the velocity of light and k is Boltzmann's constant. As temperature increases, the amount of energy emitted at any wavelength increases, and the wavelength of peal transmission decreases. The latter is given by the Wein's displacement law

$$\lambda_{mw} T = 2898 \mu m K \qquad \text{For maximum watts}$$

or

$$\lambda_{mp} T = 3670 \mu m K \qquad \text{For maximum photons.}$$

For an object at room temperature of 290°K, λ_{mw} and λ_{mp} occur at 10.0 and 12.7 μm respectively. [3,4]

6.3.3. Detection

Thermoelastic measurements using TWI are based on the determination of the change of radiance from an observed surface area that is due to an adiabatic change in applied load or stress. Planck's Law describes the spectral distribution of the radiation from a black body as:

$$M_\lambda = \frac{c_1}{\lambda^5} \frac{1}{\exp(c_2 / \lambda T)^{-1}} \qquad (6.12)$$

where M_λ is the spectral radiant emittance or exitance, λ is the wavelength, T is the absolute temperature of the black body, c_1 is the first radiation constant and c_2 is the second radiation constant. The emissivity ε of a surface is given by the ratio of the radiant exitance of the source to the radiant exitance of the black body at the same temperature. The value may lie between zero, perfect reflector and 1 (black body), and is a function of materials and surface finishing. [5,6]

6.3.4. Infrared camera

There are several methods for the detection of thermal waves, gas-cell detection, photothermal deflection, photothermal deformation, photothermal reflection, acoustic transducers, pyroelectric detectors, direct infrared detection and infrared cameras. Most of the methods, with the exception of the use of cameras, are classified as point scan methods, because they involve scanning a focused heating beam over the surface of the sample. After scanning the stored data is used to construct an image. The main disadvantage in following this procedure is that it is very slow. However, if the entire surface is heated at once and an infrared camera is used, surface temperatures can be mapped. In this way a continuous set of images can be obtained regarding the changes of temperature on the surface of any solid.

In pulsed thermography the mechanism of image formation is as follows: when a light pulse is absorbed at the surface of the sample plane a thermal wave pulse is launched into the sample, the surface temperature then starts to decay as a reciprocal of the square root of time. Meanwhile, under the surface, the pulse is propagating deeper, and simultaneously spreading and decaying.

Whenever the pulse reaches any kind of thermal inhomogeneity it is scattered or reflected. A reflected pulse is propagated back towards the surface. This pulse can be considered as an “echo” of the original pulse and once it reaches the surface it alters the rate of decay of the surface temperature so that the temperature cools more slowly. [8, 9]

The previous explanation is applicable in the case when defects such as voids are present in structural bodies and the echoes are the only means to find them. In the

research being reported, a similar principle can be used. In this case, the camera uses the emissivity of the material. The camera detects the emission of energy and creates an image, mapping the temperatures of the sample and surroundings. Then, the material is stressed. These stresses produce structural changes in the materials affecting the entropy of the system. Changes in entropy lead to changes in the internal energy of the body and consequently to temperature changes. The energy will tend to be dissipated reaching at some point the surface of the sample. This is then detected by the infrared camera.

Higher or lower temperatures are dependent on the nature of the structural changes. If the stresses originate in stress induced crystallization, energy is required for the transformation. The internal energy decreases and since this will imply a more ordered structure, the entropy of the system will be lower leading to a lower temperature. On the contrary, plastic deformation will lead to a release of energy, and increased entropy and consequently an increase in the temperature of the system. The main objective is then, to relate these structural changes to the changes in the surface temperature of the sample.

6.4. Measurement of temperature changes

The IR images from the samples were recorded using a Prism DS IR camera from FLIR Systems Inc., with a Platinum Silicide (PtSi) IR detector with an accuracy variation of 2% of the range used. The IR camera measures the emissivity of the sample by counting the photons coming from the surface, but being pyrometrics provides direct values of temperature.

6.5. Results and discussion

As an external action (force) is applied to any material it will undergo certain degree of strain which is indicative of changes in the equilibrium of the material, which will lead to energetic gradients, as the surface temperature varies. The changes can be analyzed from different perspective, according to the kind of test in effect.

6.5.1. Tensile test

By dynamic effects we will define changes that occur when the applied stress changes too. Mechanically, this would reproduce a stress-strain diagram characteristic of Hooke's law. As the strain is increased so will the stress until a maximum point is reached and the material is broken. In figure 6.2 we can observe the temperature profile that occurs at different stages of a tensile test. Following the evolution of the images in time, it is possible to observe two main stages, a cooling down effect followed by an increase in the surface temperature. The temperature scale for each image is kept constant to appreciate the changes. The temperature drops until the sample "vanishes" with the background until at some point it starts increasing again. The increase in temperature is steady for a certain time, until a major and localized change in temperature occurs in the sample. The identification of heating zones is only important if we can relate them to the structural changes that are happening in the specimen tested. Of course, even when every material undergoes the same stages of transformation and deformation, the times and strength required for a given deformation will vary among them.

From a mechanical point of view, there are also different stages. In this case, for a PP matrix, the specimen is semicrystalline and is formed of several chains with varying

degree of order. When a stress is applied, first the polymer chains will re-order, resulting in a more ordered structure, and increased degree of crystallization. The reorientation

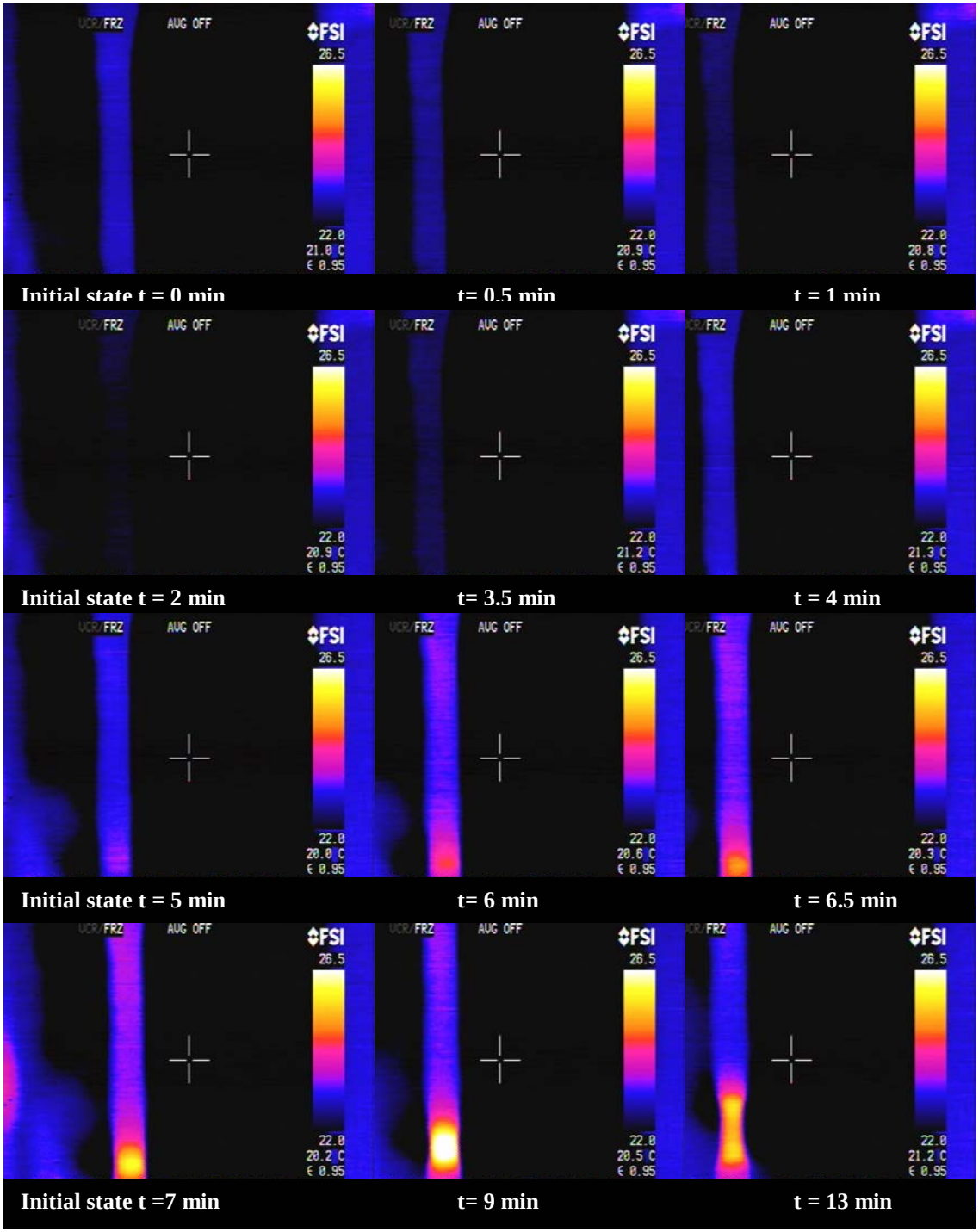

Figure 6.2. Infra red sequence of a nanocomposite sample under axial strain.

will be in the direction of the applied stress.

Table 6.1 Peaks intensity ratios showing the retention of α phase in PP.

Materials	$I_{16°}/I_{14°}$	
	Surface	**Strained**
PP	3.8	2.68
mPP	0.67	-
PP + mPP	1.08	1.39
mPP+MLS	0.96	1.19
NC 1	2.28	5.46
NC 2	4.79	6.99
NC 3	3.31	8.55
NC5	7.64	10.53

I rule out the possibility of phase transformation through the XRD of the post failure systems as observed in the table 6.1. As explained in chapter III different crystalline structures can be present in the PP. Here I can see the retention of the same

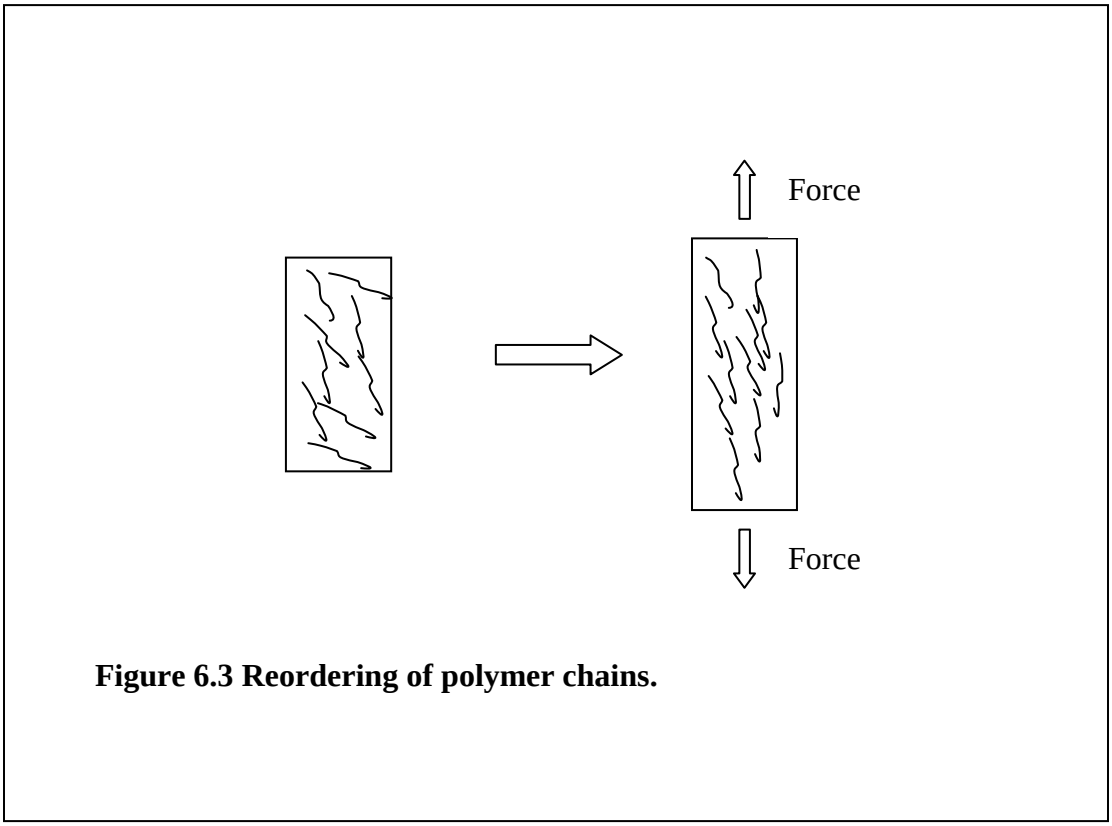

Figure 6.3 Reordering of polymer chains.

structure before and after the stressing, an α phase.

The change in the structure of the samples will lead to energetic changes since a crystallization process consumes energy, this will lead to a decrease in the energy of the sample, leading to the undercooling stage observed in the first stage of the thermal images observed. However, at some point the force applied will be above the bonding energy between molecules and deformation will occur.

Breaking these bonds will release relatively large amounts of energy, which will increase the surface temperature of the sample. This effect was also observed in the specimens tested. After identifying the different thermal stages that occur in the sample during a uniaxial test, additional analysis was done. In a conventional stress-strain curve for a semicrystalline polymer, some important points can be obtained, which define the elastic modulus, maximum strength, and yield strength of the material.

The use of thermal imaging will allow us to relate these mechanical parameters to the thermal stages identified. Table 6.2 shows some characteristic points from a set of samples including PP nanocomposites with different concentrations and the PP + mPP blend.

Table 6.2. Temperatures at different mechanical regions

mPP + MLS			**PP + mPP**			**NC 1**		
	T °C			**T °C**	**Time**		**T °C**	
Initial T	23.1	at 0 sec	Initial T	23.25	at 0 sec	Initial T	23.09	at 0 sec
Lower T	22.33	at 30 sec	Lower T	22.34	at 2.5 min	Lower T	22.86	at 42 sec
Yield T	22.35	at 12 sec	Yield T	22.46	at 42 sec	Yield T	22.88	at 34 sec
Max S T	24.3	at 1 minute	Max St T	22.45	at 3.93 min	Max S T	22.75	at 3.67min
NC2			**NC 3**			**NC5**		
Initial T	22.64	at 0 sec	Initial T	22.34	at 0 sec	Initial T	22.67	at 0sec
Lower T	22.25	at 2 min	Lower T	22.21	at 1.67 min	Lower T	22.32	at 2.26min
Yield T	22.46	at 30 sec	Yield T	22.3	at 30 sec	Yield T	22.57	at 30 sec
Max S T	22.27	at 3.93 min	Max S T	22.23	at 3.5min	Max S T	22.41	at 3.3min

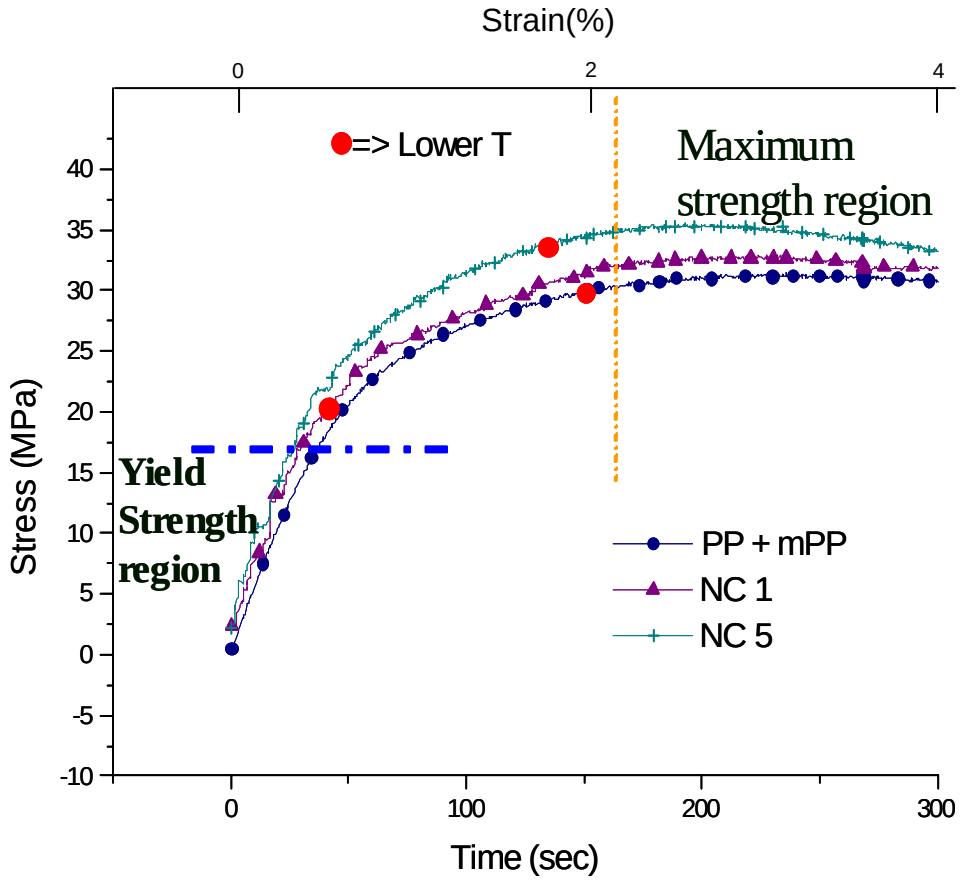

Figure 6.4 Maximum crystallization regions.

The system used to perform the uniaxial tests, allows simultaneous recording of stress, stroke and time; this last parameter allows one to relate the values of temperature with the values of stress and deformation and detect the temperature at yield and at maximum strength values.

With the exception of the blend designated as mPP + MLS all of the samples showed a certain degree of ductile behavior (even though NC 1 and NC 2 nanocomposites have brittle failure in comparison to NC 3 and NC 5, they are not as brittle as PP) and the maximum strength occurs at similar times. However, the time at which each sample reaches the lowest temperature is quite different.

I analyzed the parameters of time to maximum recrystallization, maximum sample stress and strain in figure 6.4. As can be seen, for brittle failure obtained in NC1, the end of stress induced crystallization terminated at very short terms. Samples with ductile failure recrystalized almost at the point of the ultimate tensile stress, irrespective of nanocomposite formation or not. I hypothesize that in the nanocomposites the layered silicates do not constrain chain orientation because exfoliation resulted in an average interlayer distance of 300 nm, which is well above the lateral dimension of the PP chain. This orientation proceeds without impedance in the highly exfoliated and ductile NC 5.

Figure 6.4 shows the lower temperature points for a few samples. Due to the similar behavior in all the specimens, not all of them are indicated.

As can be observed the maximum crystallization (lower temperature) in the samples is in the region between the yield strength and the maximum strength. It is

important to remember that the plot represents the stress in time, and not the stress strain behavior only.

One would think that the maximum cooling could be in the elastic region, below the yielding point, however, TWI has shown that the cooling down goes further. Another concept that can be observed from table 6.2 is the gradient of temperature from one point to another. If quantified, it could be a more defined way to distinguish among samples with the same components but small differences in concentrations.

6.5.2 Transient loading

The static loading effect is related to creep-relaxation testing. Here, the mechanisms of temperature change and the deformation stages in each specimen are expected to be the same as in the section above. However, differences in the zones will be

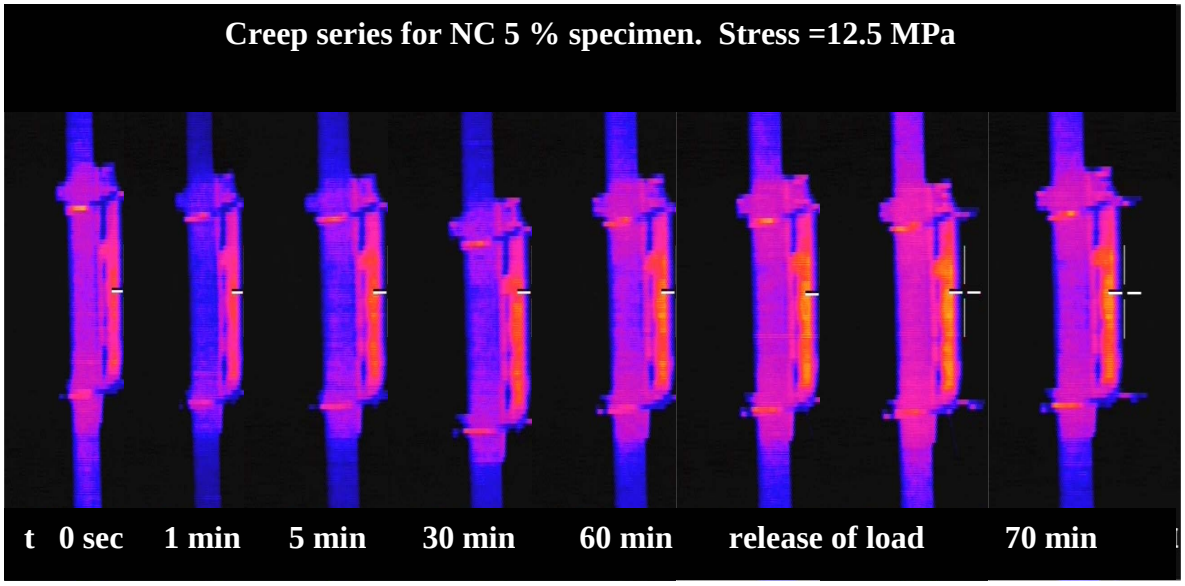

Figure 6.5. Thermal sequence for NC 5 specimen under creep at 12.5 MPa

analyzed while a constant stress is applied to the sample.

Figure 6.5 shows a reduced sequence of a creep test, where the main transitions are observed. A cooling stage can be observed right after the beginning of the test, and warming occurs as the time progress. It is important to note that the tests are done at room temperature and that small changes in temperature will balance in time. Then, only the changes that happen at critical moments should be considered. By critical times, I refer to the stressing and the unstressing of the sample. Short times as 1 minute should be considered too, but larger periods were not controlled environmentally and can not be correctly interpreted.

In figure 6.5 it can be seen that stress application produces a cooling in the surface of the sample. Since the stress is kept constant, at some point any possible deformation that could be induced will stop, and the sample will equilibrate with the environment; this is the effect observed after 5 minutes of application of the stress. Once the stress is released, another increase of temperature is observed. This is explained as follows, the constant stress induced a gradual crystallization of the specimen, which is in a metastable condition, while the stress is kept; this crystallization yields a decrease in the surface temperature of the sample.

As the stress is released, the metastable state of the specimen finishes, returning to its original structure, or at least to a less ordered structure. All the energy stored for the specimen in its metastable state is released, which is translated as an increase in the surface temperature of the sample. In the relaxation period, once the stress was released, it can be observed that the surface temperature decreases. Again, this is explained by the balance of temperatures on the surface and the room temperature. We observe that at 30

minutes after the stress is applied and also when it is removed, the surface temperature completely recovers. Figure 6.6 shows the points in the creep-relaxation plot where the

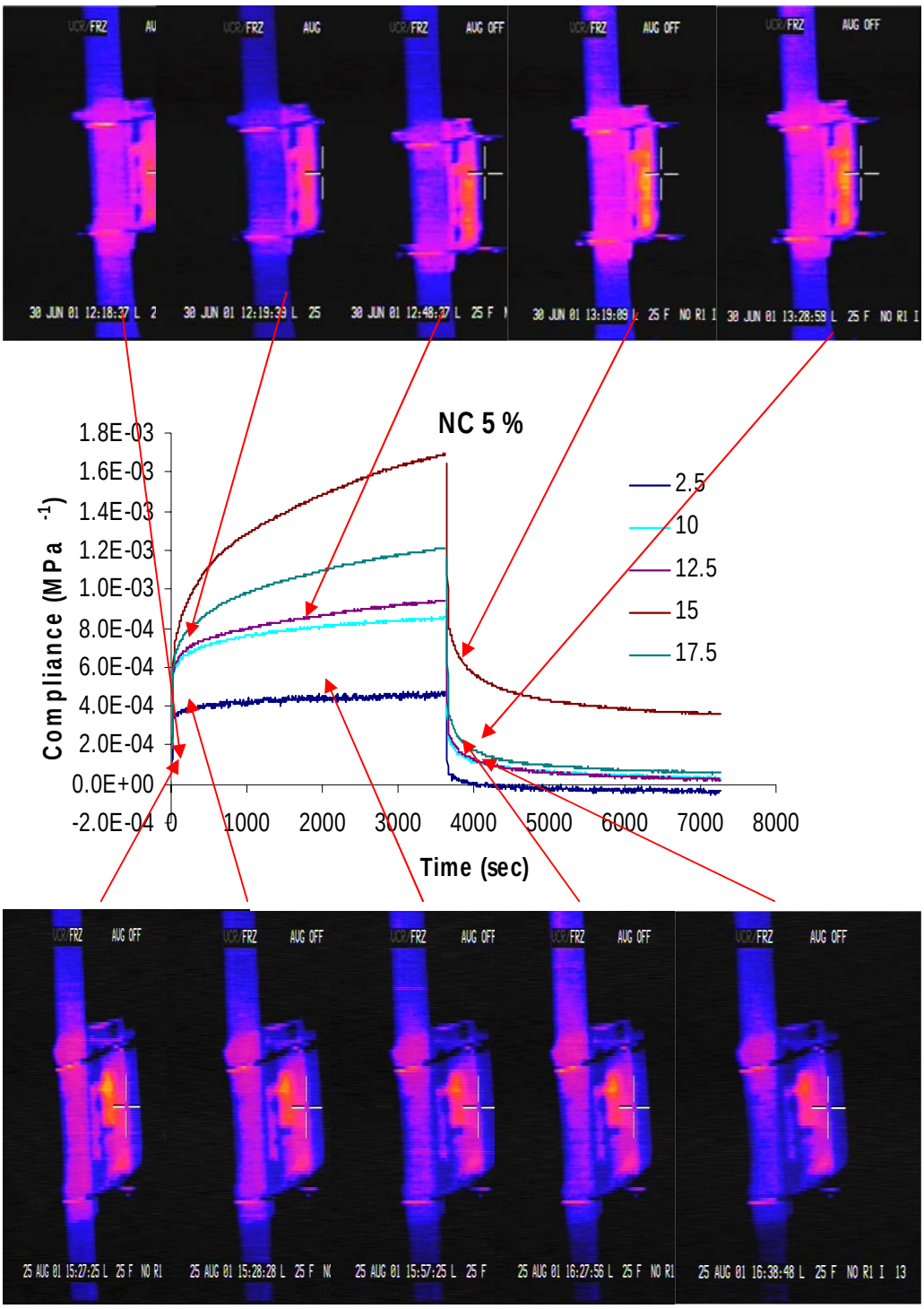

Figure 6.6. Thermal sequence at creep test.

images were taken, and its location in relation with the critical points defined. Different levels of stress show that the variations in temperature are different.

The time values allow us to relate the stress level and the temperature changes. In the figure we observe that the level of stress produces a different change in temperature, since the energy that is stored and released will be different too, making it possible to differentiate between the levels of stresses. Values of temperature for different systems are shown in table 6.3.

So far, we have observed the changes in temperature of specimens while an external action acts on it. It was also said that all changes are energetic changes that can differentiate the mechanical points of interest that separate stages of material deformation. Linking now the results to the concept of entropy, I define the changes and thus, deformation.

Entropy can be understood as the degree of randomness in a system. If we consider our polymer to be oriented by a certain degree, this will be the degree of randomness, its chain orientation. When a stress is applied the chains will be oriented in the direction of the stress, decreasing the disorder in the system, thus decreasing the entropy. On the other hand, when the stress is released, and the changes are not permanent, the original order will be reestablished, increasing the entropy and then the energy of the system. When the force is enough to break the bonds in the polymer system then, the disorder is even higher, and so a large change in the energy and temperature of the specimens is noted

Table 6.3. Changes in temperature during creep

mPP+Cl			**PP + mPP**			**NC 1 %**		
DTL	DTU	DTS	DTL	DTU	DTS	DTL	DTU	DTS
-0.02	*0.31*	*-0.65*	*-0.01*	*0.47*	*0.04*	*0.00*	*0.20*	*0.10*
-0.25	*0.13*	*0.33*	*-0.21*	*0.13*	*0.32*	*-0.20*	*0.23*	*0.29*
-0.98	*0.05*	*-0.47*	*-0.73*	*0.27*	*-0.12*	*-0.97*	*0.31*	*-0.27*
-0.40	*0.45*	*-0.53*	*-0.23*	*0.39*	*-0.51*	*-0.33*	*0.32*	*0.58*
-0.44	*0.21*	*0.04*	*-0.47*	*0.58*	*-0.44*	*-0.47*	*0.44*	*-1.23*
-1.19	*0.72*	*-0.64*	*-0.40*	*0.62*	*-0.34*	*-0.60*	*0.56*	*-0.62*

NC 3 %			**NC 5 %**		
DTL	DTU	DTS	DTL	DTU	DTS
-0.86	*0.00*	*0.77*	*-0.09*	*0.08*	*-0.71*
-0.23	*0.43*	*-0.04*	*-0.21*	*0.12*	*-0.78*
-0.28	*0.17*	*-0.40*	*-0.24*	*0.20*	*0.36*
-0.10	*0.30*	*0.02*	*-0.51*	*0.37*	*-0.84*
-0.40	*0.41*	*-0.47*	*-0.37*	*0.34*	*-0.11*
0.00	*0.00*	*0.00*	*-0.50*	*0.39*	*0.53*

DTL = Change of temperature at stressing.

DTU = Change of temperature at unstressing

DTS = Change in temperature while stressed

6.5.3 Detection of stresses

Among the multiple applications of thermal imaging, fracture analysis has been one with the most benefits. The study of fracture as a mechanical concept initiated recently, in the last century. In very short time, multiple theories and mechanisms of failure have been proposed, and profiles of stress concentration have been developed to explain the difference in failure mechanisms for different materials. TWI can follow all these stress profiles during the test. Even more, it makes the classification of the failure mechanism for a given specimen, clearer than purely checking the load-deflection data.

Samples of PP and PP nanocomposites have been tested to follow the thermal profiles originating in the samples as consequence of the fracture process. Figure 6.7 shows a sequence of fractures for a nanocomposite specimen.

In the figure, the different stages that a ductile material will follow are shown. These stages can be defined as a) zero stress, b) elastic deformation, c) elastic-plastic deformation, d) plastic deformation, and e) failure by crazing.

The zero stress stage is basically the beginning of the test. The grip does not touch the sample for a period of 1 second and the initial conditions of the sample, temperature and shape can be observed. Also the notch is identifiable at the bottom of the sample.

Once the stress starts, a slight cooling is observed in the specimen, right above the notch during the first 10 seconds of test. From the mechanisms that I have discussed so far in uniaxial testing we know that the region where the temperature decreases, corresponds mainly to an elastic deformation. First signs of plastic deformation are

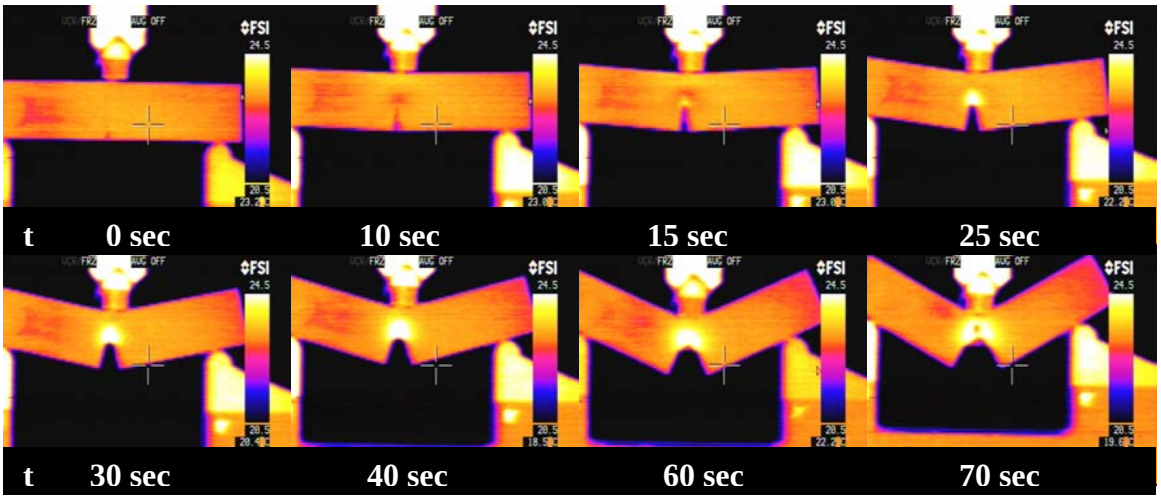

Figure 6.7. Thermal wave images of a nanocomposite specimen during fracture toughness test

observed in the elastic-plastic stage. In this stage, an increase of temperature in the region above the notch, in the path of crack propagation, is observable. The increase of temperature is a result of the crazing generated in the region. At this stage the "thermal area" above the crack opening is small but defined and resembles an elliptical shape. Above the elliptical region, it is possible to observe a region where elastic deformation is taking place.

Plastic deformation can be identified because the elliptical area defined by the

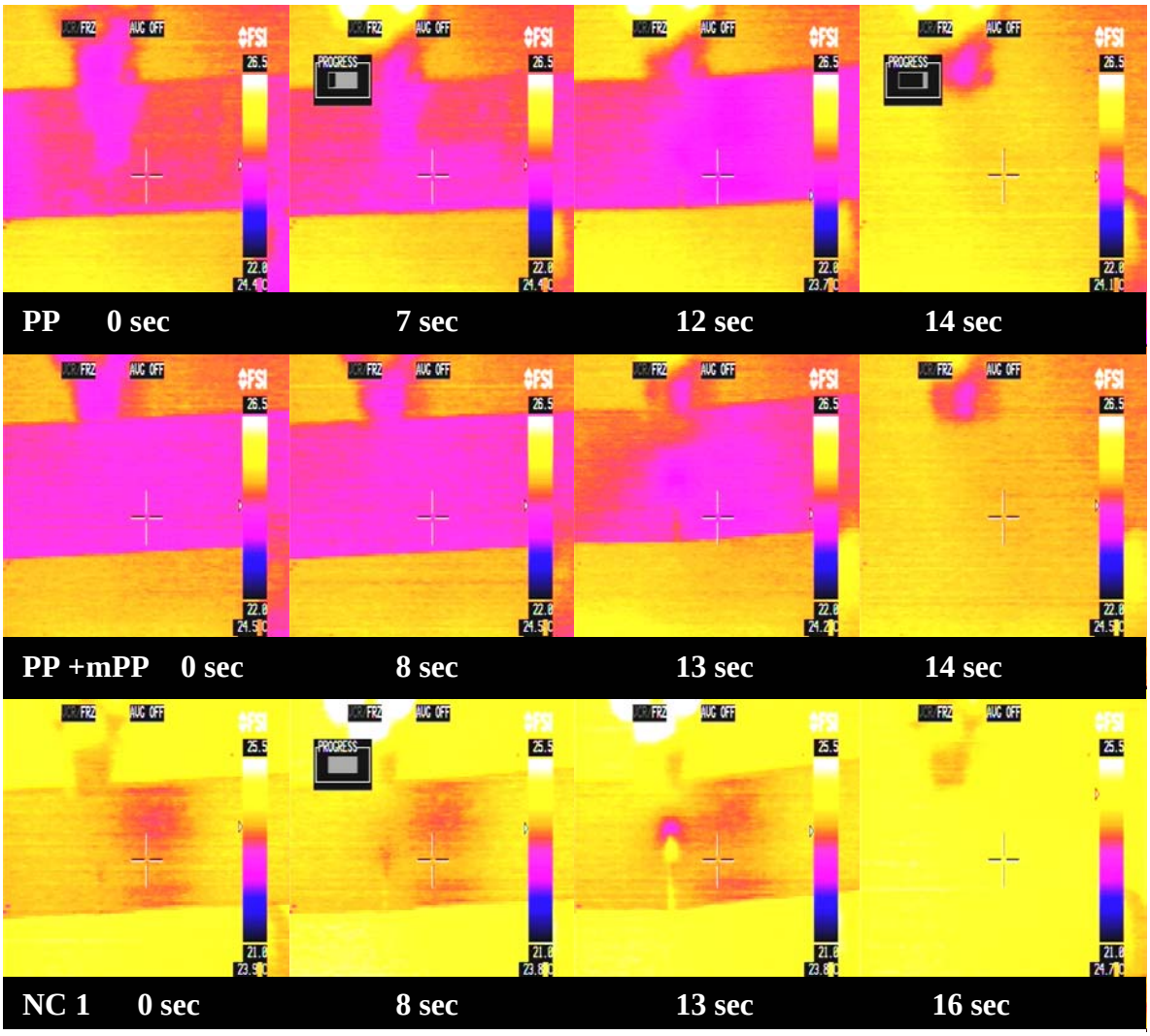

Figure 6.8 Fracture sequence for different specimens

increment in the surface temperature grows until it covers the entire width of the specimen. At some point a small region indicating a lower value of temperature is observed in the center of this area. This is a void, which indicates that the sample is close to fracture.

It is important to clarify that not all the specimens showed all the stages clearly. PP, a thermoplastic, has a brittle failure in the fracture toughness test. But the addition of certain fillers, or more precisely, the addition of MLS and mPP increased the degree of ductility in the sample. Figure 6.8 shows differences in the failure profiles for different materials and concentrations. At the top it can be observed that the PP failed just as described, while it was cooling down, or in other words, right after the elastic deformation region. With 2 % of the mPP, the specimen shows a smaller plastic zone than PP, and among other properties, a lower elastic modulus and flexibility. However, the addition of 1 % MLS develops a plastic zone, or in other words, improves the ductility of the specimen. In figure 6.7, the sequence of failure is for a concentration of 5 % of MLS. Comparing these two sets of images, we can observe what the addition of MLS induces in the PP matrix. This concept brings up another point. While PP and PP + mPP showed ductile behavior in the tensile test, this was not observed in the fracture toughness measurements. In other words, the characteristic of anisotropy showed for these specimens and low concentration of MLS, differed when a crack was present.

From the point of view of TWI analysis, the identification of the zones is the most important concept. Fracture mechanics theory has divided the crack propagation phenomena into two main contributions, elastic and plastic. The plastic contribution is the one that defines the degree of fracture toughness of a specimen. If we combine this

concept with the thermal regions that have been defined, we can identify a tough material by the thermal regions observed. From a mechanical point of view, a larger plastic region will be indicative of crazing, where the crack propagation is slow in comparison with a specimen where elastic contributions dominate.

6.6. Fracture and surface energy

In polymer fracture the thermal events are the result of deformational processes and rupture of macromolecules. Normally, the appearance of the initial sources of fracture (cracks) results in local plastic deformation. The plastic work developed during the deformation is transformed into heat which leads to an increase in the local temperature during the crack propagation of solids. For a plate-like deformation state the following equation could be used to determine the surface energy produced:

$$\sigma_0 = \left[\frac{2E\Gamma}{\pi l(1-\mu^2)} \right]^{\frac{1}{2}} \tag{6.13}$$

where σ_0 is the critical stress, E is the elastic modulus of the material, Γ is the surface energy, 2l is the length of the elliptical crack and m is the poison ratio. However equation 6.13 is based on the energy balance of the deformation, and is based on brittle fracture, neglecting the plastic contribution. By using Γ_{eff}, which represents the brittle and plastic contributions ($\Gamma_{eff} = \Gamma_{brittle} + \Gamma_{plastic}$) and equation 6.13 in equation 6.14

$$\sigma_0 = \left[\frac{2E\Gamma_{eff}}{\pi l(1-\mu^2)} \right]^{\frac{1}{2}} \tag{6.14}$$

Actually, the value of Γ_{eff} is dominated by the plastic contribution. Whether the fracture of solids is brittle or quasi brittle (brittle-plastic) depends on the stress state on the tip of the crack.

6.6.1. Surface energy

The fracture mechanism in the material can be related to the energy of the system. In addition to the temperature reading by the thermal wave camera, the image also provides useful information about the elliptical cracking area.

This feature, will aid in the determination of the surface energy before failure, which can also be used as a parameter of characterization of each specimen. This surface energy can be calculated from equation 6.14, by using ,

$$\Gamma_{eff} = \frac{\sigma_0^2 \pi l (1-\mu^2)}{2E} \tag{6.15}$$

The relative surface energies calculated are shown in table 6.4. The value of PP was taken as reference.

Table 6.4. Relative surface energies for the different samples

	Γ_{eff}
PP	1
PP + mPP	2.37026257
NC 1	3.326196
NC 2	2.59104601
NC 3	5.24986792
NC5	10.7612865

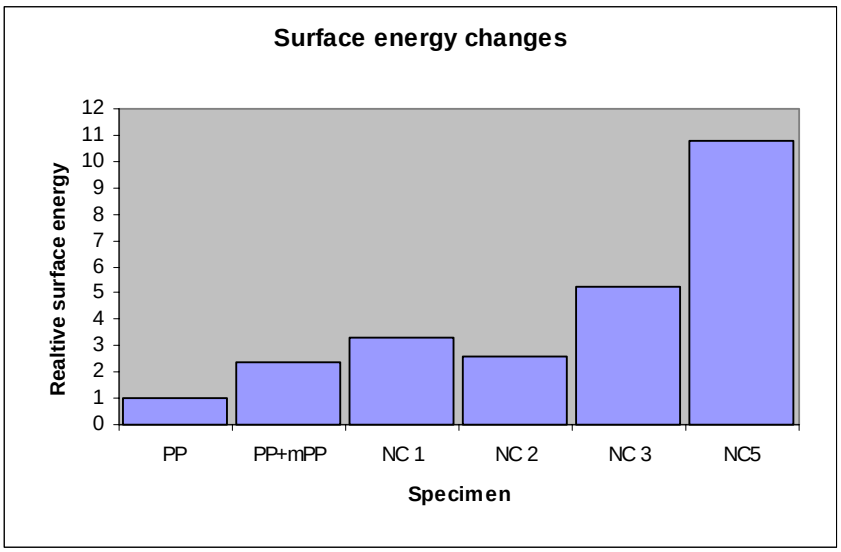

Figure 6.9. Changes in surface energy (Normalized to PP)

As can be seen in table 6.4, the difference in the surface energies is clear when any additive is added to the PP matrix, showing more than twice the original value. This trend remains almost the same for the two first concentrations of MLS in NC1 and NC 2. However, for NC3 and NC 5 this trend increases in an exponential way, and the energies reported are up 5 and 10 times respectively. Figure 6.9 shows graphically the change in surface energy.

In the equation (6.15), the term Γ_{eff} includes the plastic and the elastic contribution, again the plastic contribution being the one with a much higher value.

This point could also corroborate the result obtained previously. If a given specimen has a higher surface energy and this energy is mainly determined by the plastic contribution, then the higher plasticity is obtained in NC 5.

6.7. Conclusion

The use of thermal wave imaging to follow the structural changes while a mechanical stress is acting on a specimen has proven to be an additional tool to understand the transitions occurring in the material. It has been found that these structural changes produce first a rearrangement or reorientation of the polymer chains, which leads to a less random system. The entropy and the internal energy in the system will decrease. The decrease in these thermodynamic properties will result in a cooling down on the surface of the sample. Once the sample has reached the maximum order possible, the deformation of the structure, rupture of the entanglements among chain, voiding and finally failure events will be observed in the material. All these stages have a common response, increase in the randomness of the system. As opposed to the first stage, this will lead to an increase in internal energy and then in surface temperature of the system.

A second contribution of thermal wave imaging is during the creep stage, when it was possible to observe how after the applied stress is released, depending upon the level of stress, there is complete recovery or permanent deformation in the specimens. The energies in these first two tests are not quantified. Due to the conditions of testing, there is not a defined area where the failure will occur and any calculation will contain a big error.

In the three point bending technique used to obtain the fracture toughness of the material, the location of the failure is easy to anticipate and real time following of the crack propagation can be done, the crack progress through the material as well as the thermal events that will happen in the surroundings. Here it was possible to identify

different stages in the fracture, but the most important probably is the differences in the elastic and plastic contributions from one sample to the other. It was known from the literature that the plastic contribution has to be higher, and also from the calculation, but now it has been proven in a visual way.

The initial objective planned for the use of the technique has been determined and identified in a qualitative manner. A quantitative analysis of the changes can be done only at certain stages where the specimens are already deformed irrecoverably, but this is also applicable.

References

1. Boccara AC, Fournier D. Progress in Photothermal and Photoacoustic Sciences and Technology 1. New York. Elsevier ed. by Mandelis A 1992, 3-39
2. Busse G, Walther HG. Photothermal nondestructive evaluation of materials with thermal waves. New York. Elsevier ed. by Mandelis A 1992, 205 – 298
3. Davis AP, Lettington AH. In Applications of Thermal imaging. Philadelphia. Ed by Burnay SG, Williams TL, Jones CH. Adam Hilger 1988. 1-34
4. Barron WR. In Omega's Temperature handbook. 2001.
5. Webber JMB. In Applications of Thermal imaging Philadelphia. Ed. by Burnay SG, Williams TL, Jones CH. Adam Hilger 1988. 191-225
6. Merchant J. In: Omega's Temperature handbook. 2001
7. Almond DP, Patel PM. In Applications of Thermal imaging Philadelphia. Ed. by Burnay SG, Williams TL, Jones CH. Adam Hilger 1988. 226-241

8. Favro LD, Han X. In Sensing for materials characterization, processing and manufacturing, Vol. I. Birnbaum G, Auld BA. Ohio. Ed . American. Soc. For Nondestructive testing Inc. 1998. 399- 416.
9. Han X, Favro LD, Thomas RL. 2nd Joint NASA/FAA/DoD Conf. On aging aircraft. Virginia. 1998
10. Godovsky YK. Thermophysical prop of Polymers. New York. Spanger-Verlag 1992 (chapter 1, 4, 6, 7 and 8).
11. Rudin A. The elements of polymer science and engineering, 2nd ed. New York. Academic Press 1992 (chapter 7 and 8)
12. Anderson TL. Fracture Mechanics, 2nd ed. New York. CRC press 1995 (chapter 1, 2 and 3).
13. Hashemi S, Arkhireyeva A. Polymer 2002; 43: 289-300.
14. Pardoen T, Marchal Y, Delannay F. Engin Fract Mechan 2002; 69: 617-631.
15. Karger-Kocsis J, Czigany T, Moskala EJ. Polymer 1997; 38: 4587-4593.

CHAPTER 7

SUMMARY

1. The addition of MLS leads to a thickness dependent dispersion of MLS in PP. The core tends to retain the monoclinic structure characteristic of PP while the surface shows a marked change to a triclinic phase. This has been attributed to the effect of the mPP used as a compatibilizer.
2. The MLS also has an effect on the nucleation and particle size of the PP spherulites. Nucleation increases with the presence of both mPP and MLS in the matrix, but particle size distribution and retention of the spherulitic size is only noticed when the MLS content is high.
3. The quasi-static response of nanocomposites differs from the transient creep response. The elastic modulus, yield strength, and ultimate tensile strength were retained for the MLS concentrations investigated, while an important increment in the elongation to failure was induced at higher MLS concentrations.
4. Compliance in the system also improved with the MLS concentration. Once more, low concentration of MLS stopped and locked the softening effect of the mPP, but at higher concentrations considerable reduction in the compliance was observed.
5. Probably the most valuable result obtained in the practical utilization of PP nanocomposites was the fracture toughness. One of the concentrations suggested at the beginning (5%) resulted in a tough nanocomposite. The

relevance of this result is that no tough nanocomposite has been reported using a PP matrix.

6. The thermal wave imaging analysis provided helpful information to follow the structural changes that the material experienced while being tested but the most important contribution can be found in the fracture analysis. Thermal wave imaging analysis allows to differentiate the distribution of the energy to failure and helps to explain the differences among different concentration of MLS and why the 5 % content provided the higher mechanical performance.

The work presented is expected to contribute to the study of nanocomposite systems and to serve as a guideline for future research in similar systems to obtain similar effects, especially in fracture toughness. In addition, it is intented to introduce thermal wave imaging as a technique and tool in mechanical analysis.

7.1. Future work

The following themes are suggested, based in the presented work:

- Energy quantification of the structural deformations
- Analysis in a different semycristalline matrix
- Analysis in amorphous matrices
- Analysis using different compatibilizers
- Compile all the results obtained and create a model that would be able to predict properties of nanocomposite systems.

APENDIX A
CREEP - RECOVERY PLOTS OF PP AND PP NANOCOMPOSITES

Creep recovery plots describing the behavior of each specimen are illustrated in this section. Their addition to this work is considered since a better understanding of the behavior of each specimen will result from the analysis of these plots. The differences in deformation are shown and comparisons can be done.

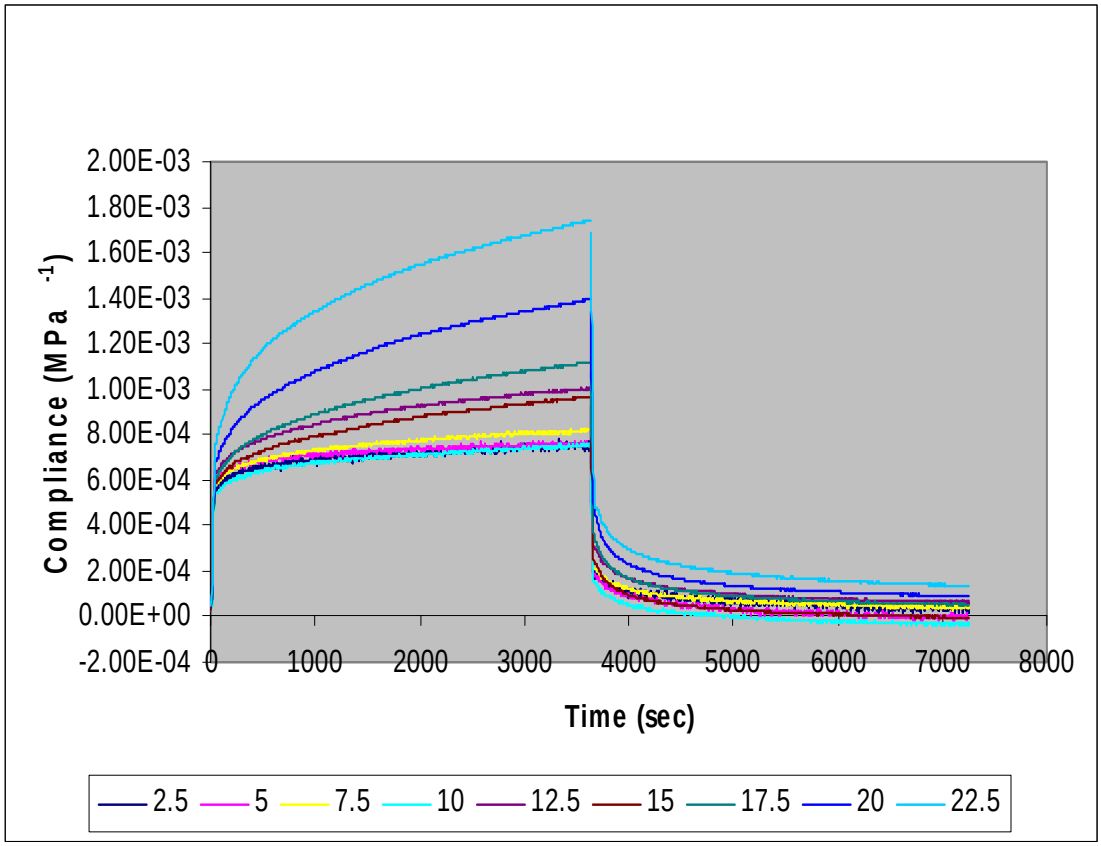

Figure A1. PP creep – recovery plots

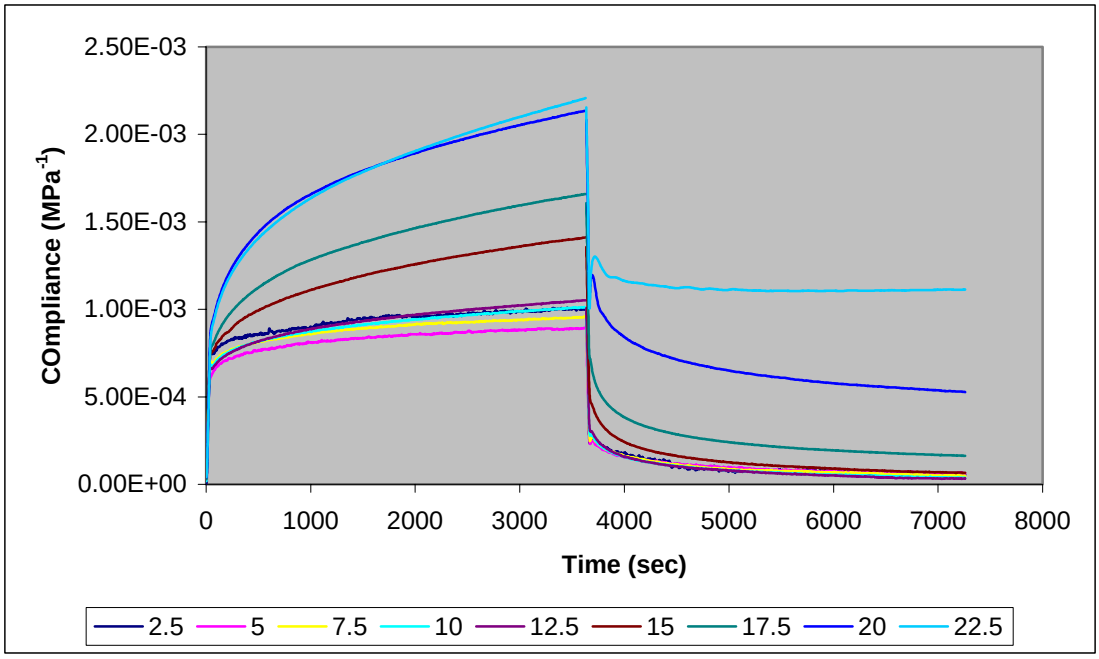

Figure A2. mPP + MLS creep recovery plots

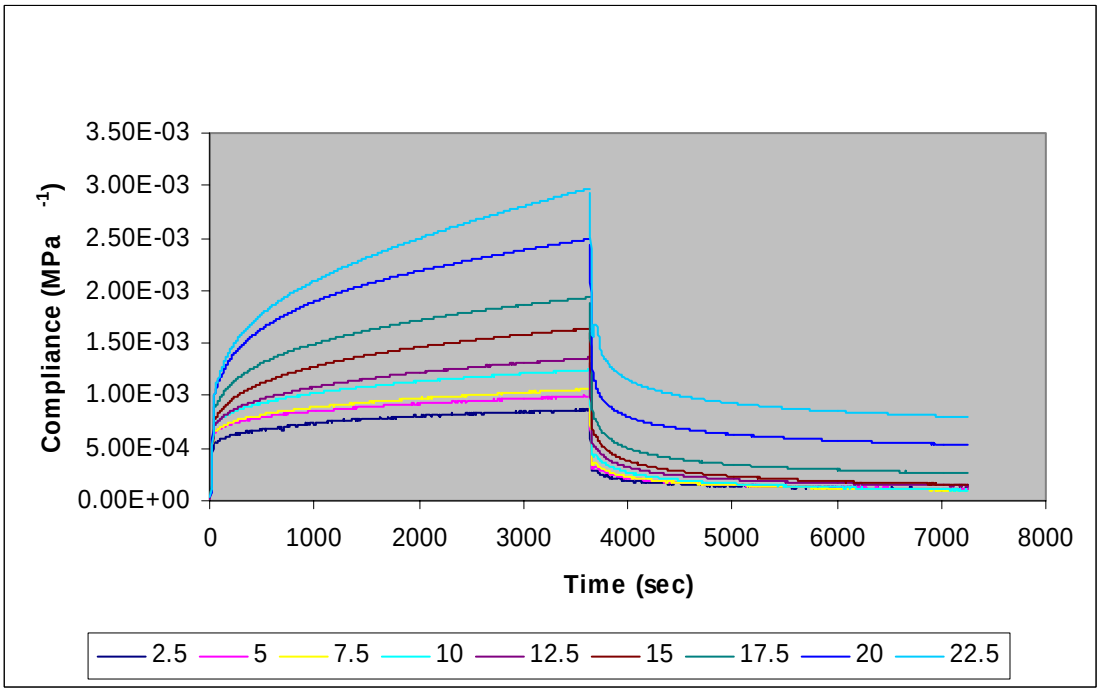

Figure A3. PP + mPP creep-recovery plots

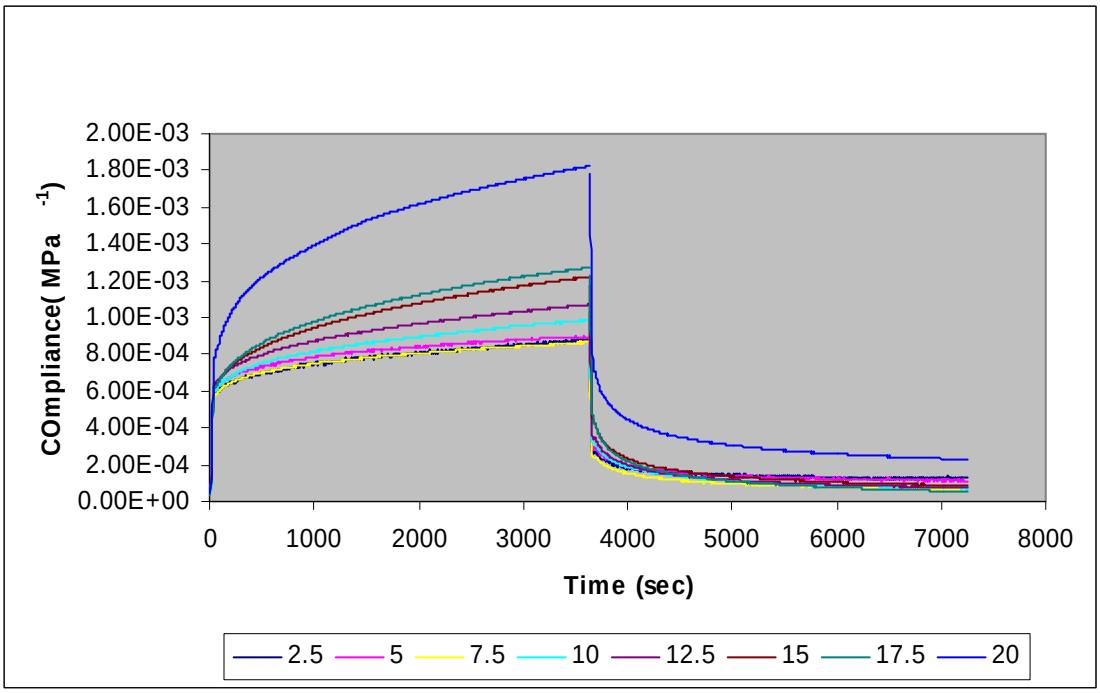

Figure A4. NC 1 creep – recovery plots.

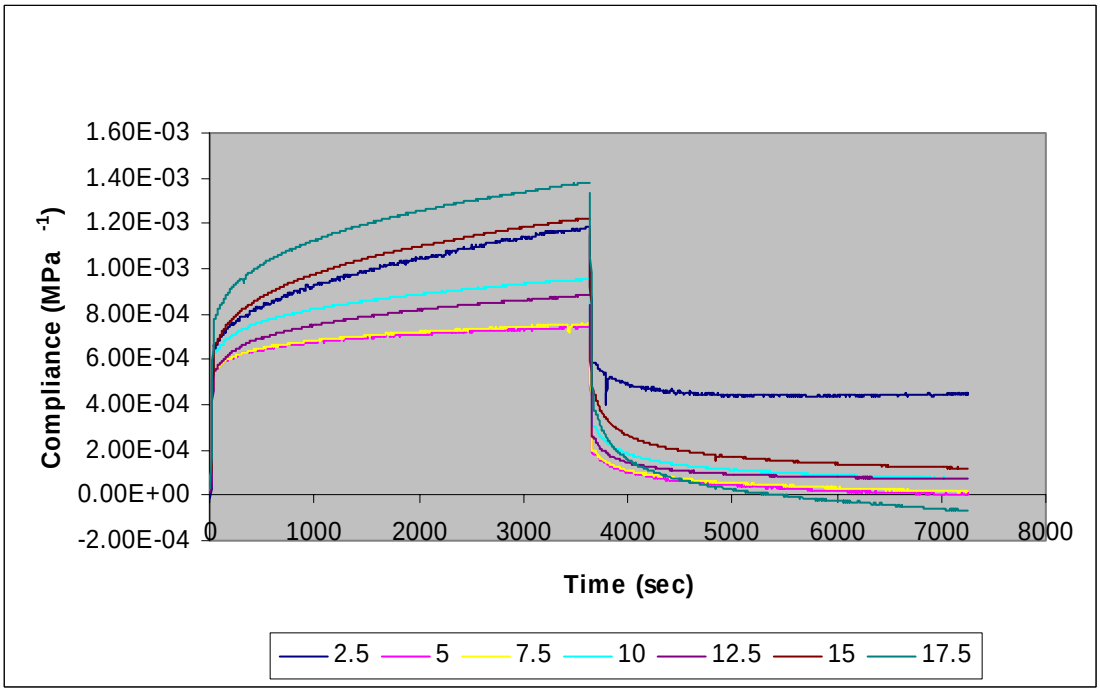

Figure A5. NC 2 creep – recovery plots.

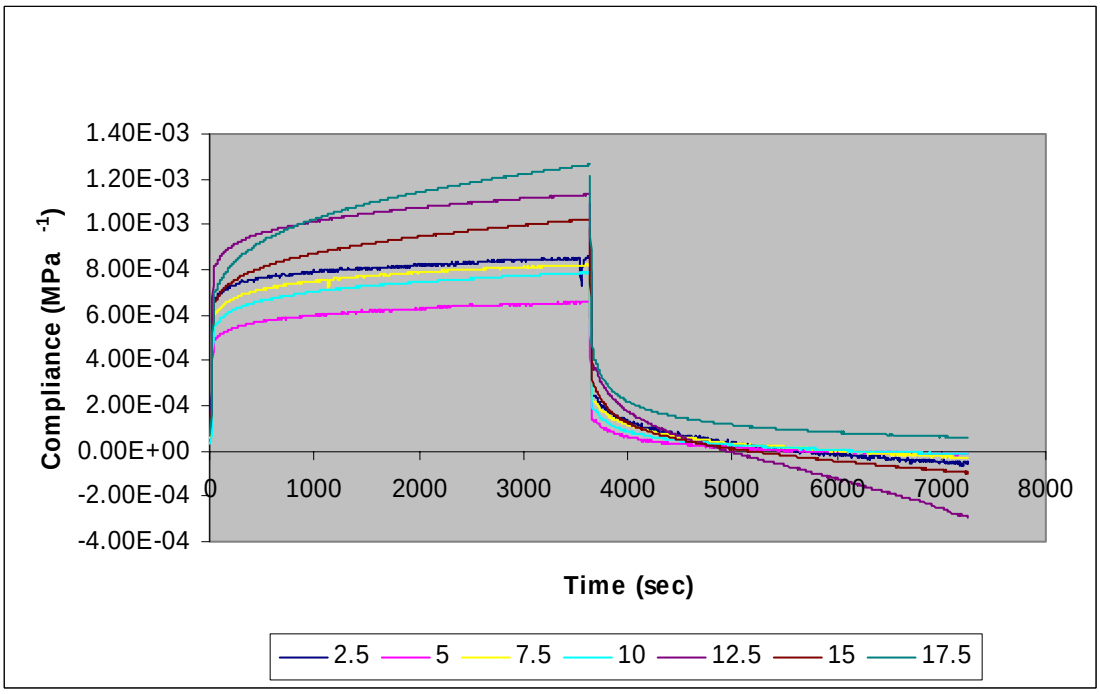

Figure A6. NC 3 creep – recovery plots.

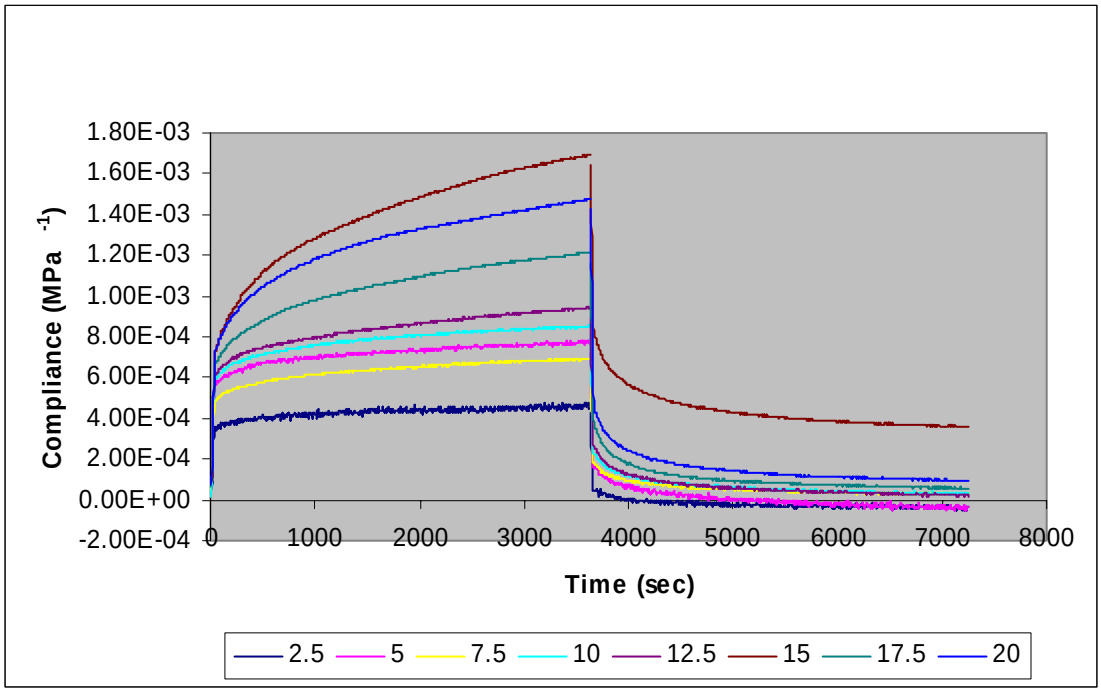

Figure A7. NC 5 creep – recovery plots.

APENDIX B
THERMAL WAVE IMAGES

In this work the use of the TWI technique as a way to characterize the morphological changes of the materials was introduced. As explained, it can be used to distinguish from one material to another by visualizing structural changes. The images below show the initial and final stages of some of the samples. The images are self explanatory; differences can be noted.

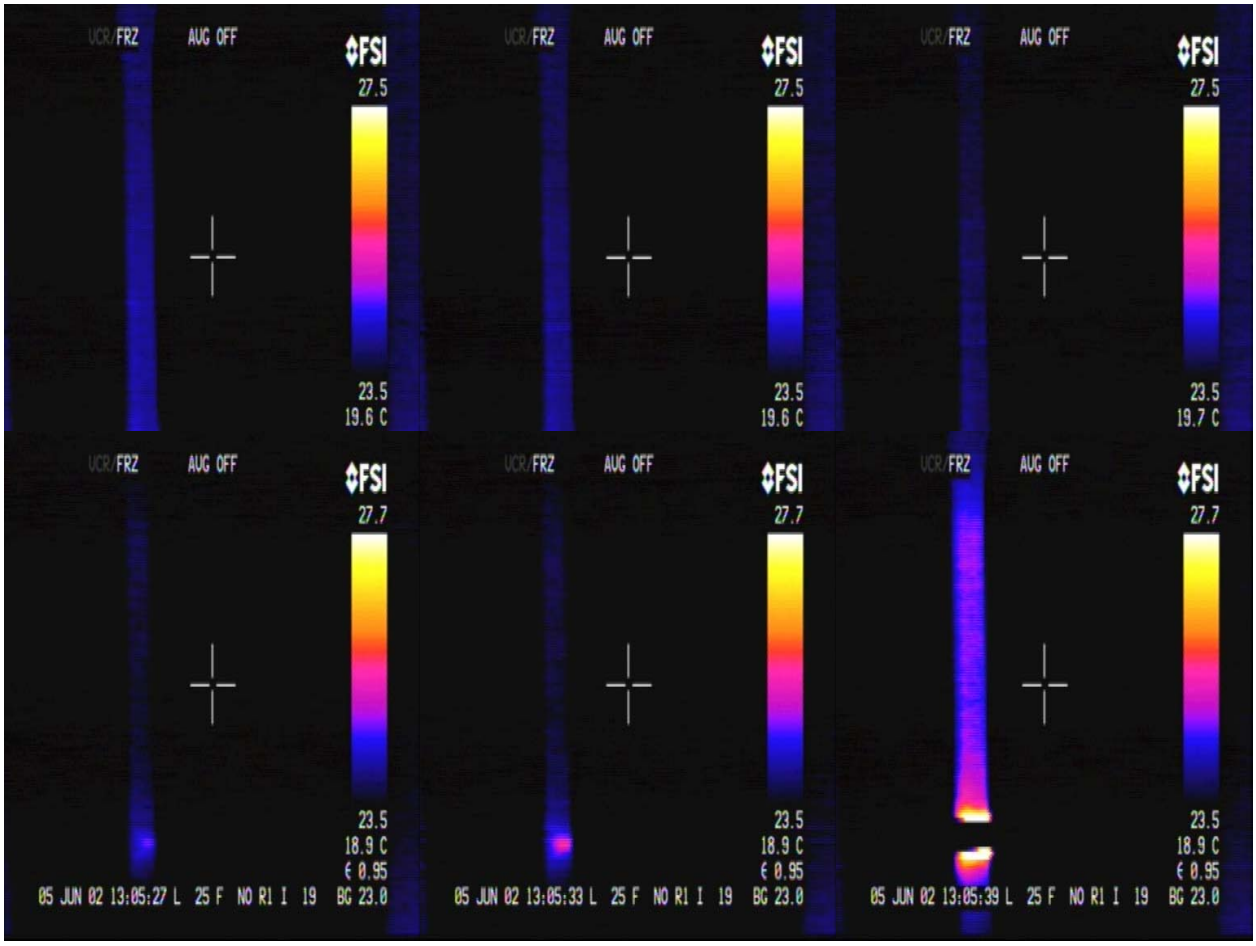

Figure B1. Tensile fracture of PP.

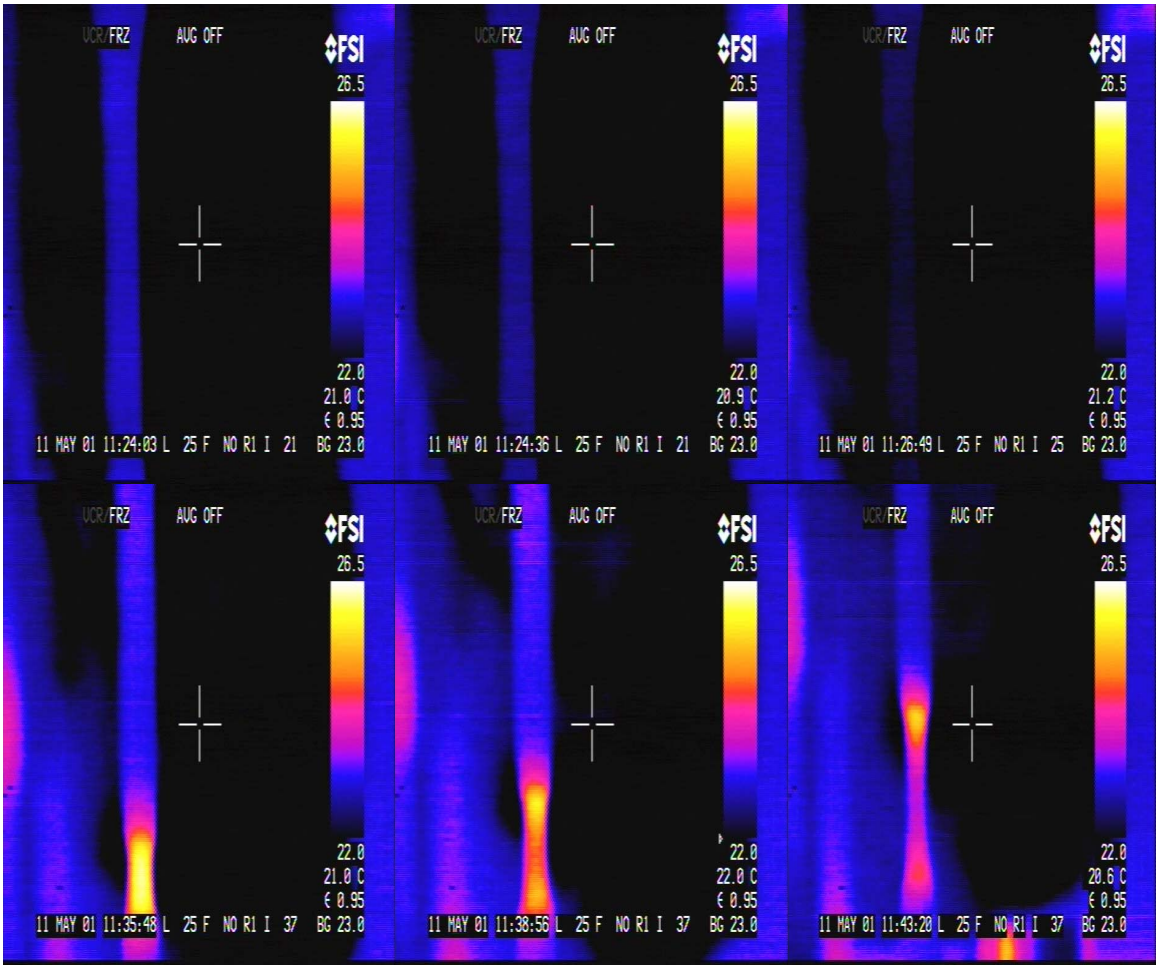

Figure B2. Tensile failure of NC 5

Note how the neck formation generates increments in temperature identifying the areas of stress concentration.

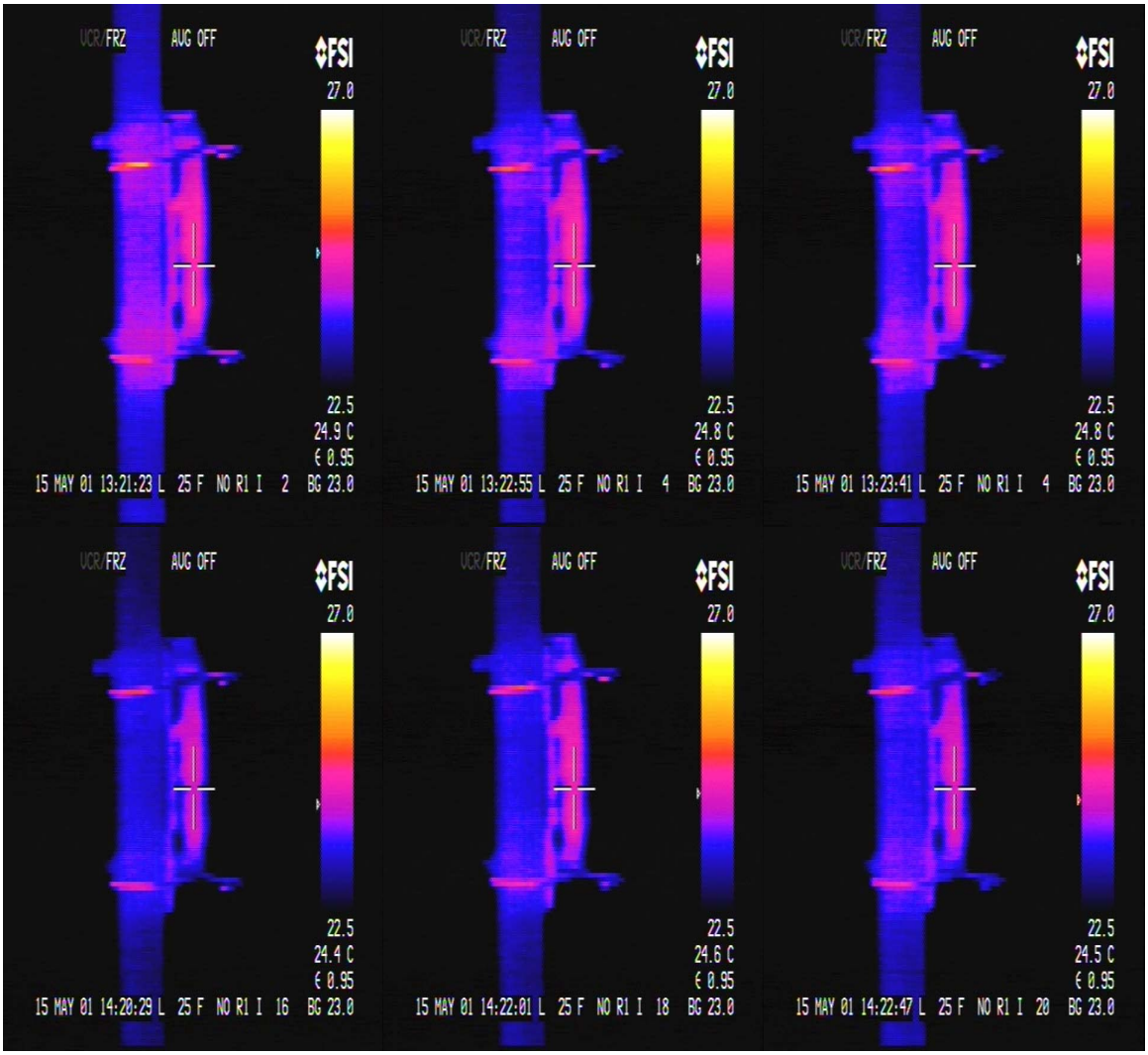

Figure B3. TWI of initial and ending creep for NC 3 at 7.5 MPa.

It can be distinguished the cooling down at the beginning of the test as the load is applied to the sample and the slight warming at the end, when the load is just released. Since it is at low stress, the changes will be not as clear as when a high stress is used.

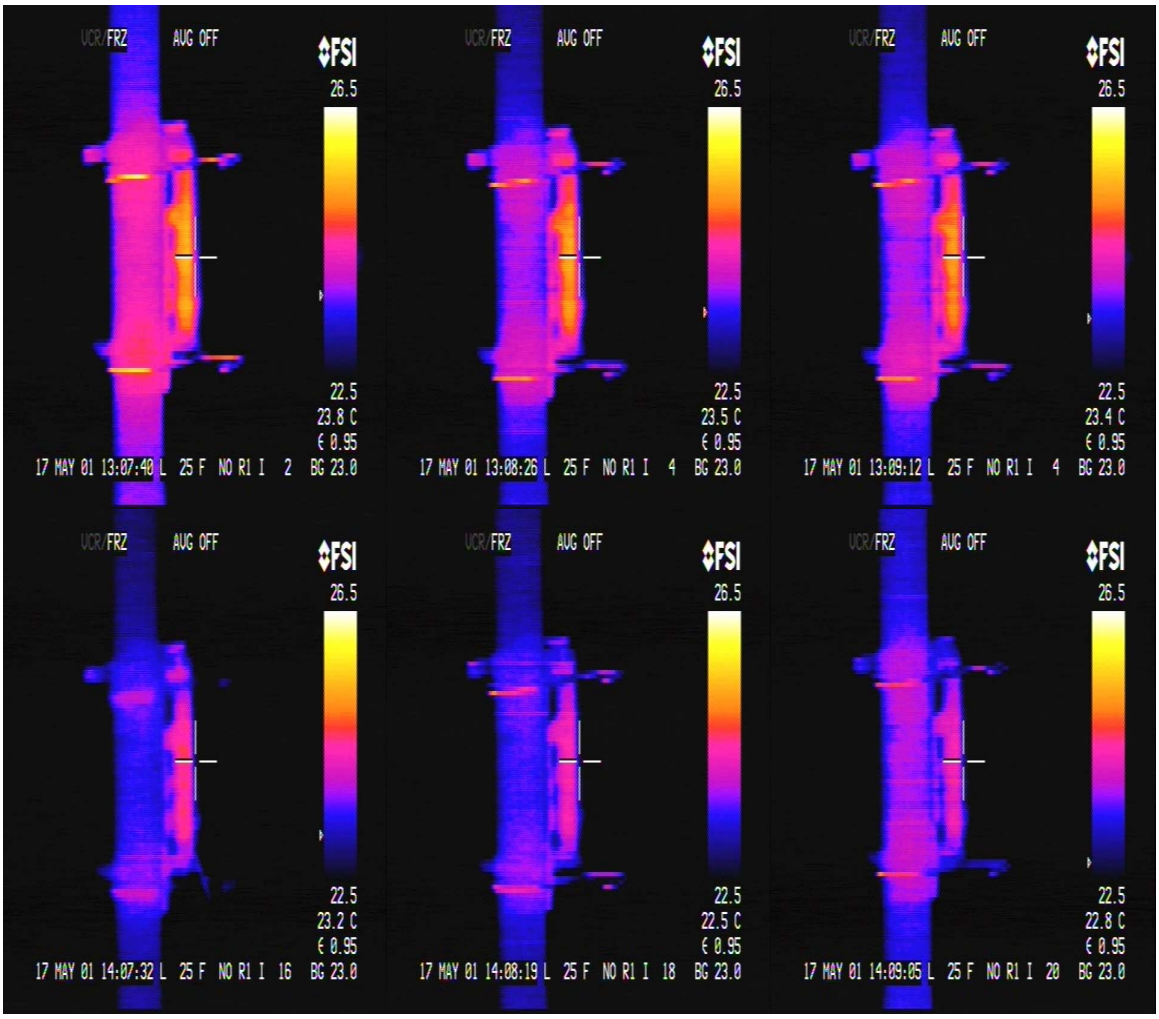

Figure B4. TWI of initial and ending creep for NC 3 at 20 MPa.

In this last figure the effect of loading and unloading is more clearly observed. A small decrease in the surface temperature is observed at the beginning, while the warming up of the specimen is observed at the time the stress is released.

As these examples and the ones explained during the work, images exists for every sample, and depending on the test, samples are available for short and long time intervals. There are available more than 10 Giga Bytes images that correspond to more than 10,000 images concerning the test I ran. A separate document with sequences (movies) generated from these images is available.